8-11-2015

Quantification of Nonlinear And Dynamic Charge Transport Through Nanoscale Confinements

Dengchao Wang

QUANTIFICATION OF NONLINEAR AND DYNAMIC CHARGE TRANSPORT THROUGH NANOSCALE CONFINEMENTS

by

DENGCHAO WANG

Under the Direction of Gangli Wang, PhD

ABSTRACT

Structurally defined nanopores have received great attentions in the past decade for both novel mass transport phenomena at nanoscale solid-liquid interfaces and practical applications exploiting such processes. New capabilities and/or better efficiency are envisioned in molecular sensing, energy storage and conversion, nanofluidics, and membrane transport. However, the dynamics of the mass transport (MT) processes in nanopores remain poorly understood, albeit steady-state MT processes have been extensively studied. In this dissertation, multiple time and frequency- domain electrochemical techniques have been used in combination with simulation to investigate the dynamic transport of aqueous electrolytes through single conical nanopore

embedded in glass membrane or capillary. Electrical ionic current results from the transport of ions or other charged species. The current signal is limited by and thus reflects the transport at the most resistive/smallest nanopore region. Stimulated by an external triangular potential waveform, an intriguing non-zero cross point and pinched hysteresis current-potential curves have been discovered. Those emerging transport behaviors are quantified and correlated to the surface and geometry properties of the nanopores as well as the frequency of the external stimuli. Accordingly, multiple processes with different transport dynamics are deconvoluted and quantified respectively. At different frequency ranges, the dynamics of concentration polarization and ionic current rectification are decoupled from the charging/discharging of the glass membrane. Furthermore, physical models and empirical equations are proposed to describe the nonlinear current-potential responses. The last chapter of this dissertation describes the electronic structures and corresponding physicochemical properties of gold-thiolate clusters as novel functional nanomolecules.

INDEX WORDS: Dynamic mass transport, single conical nanopores, memory effects, ionic concentration polarization, ionic current rectification, finite element simulation.

QUANTIFICATION OF NONLINEAR AND DYNAMIC CHARGE TRANSPORT THROUGH NANOSCALE CONFINEMENTS

by

DENGCHAO WANG

A Dissertation Submitted in Partial Fulfillment of the Requirements for the Degree of

Doctor of Philosophy

in the College of Arts and Sciences

Georgia State University

2015

QUANTIFICATION OF NONLINEAR AND DYNAMIC CHARGE TRANSPORT THROUGH NANOSCALE CONFINEMENTS

by

DENGCHAO WANG

Committee Chair: Gangli Wang

Committee: Stuart Anthony Allison

Markus W. Germann

Electronic Version Approved:

Office of Graduate Studies

College of Arts and Sciences

Georgia State University

August 2015

DEDICATION

This dissertation is dedicated to my parents and sisters.

ACKNOWLEDGEMENTS

I would like to sincerely thank my advisor Dr. Gangli Wang for his excellent guidance, patience, caring and proving me with an excellent research atmosphere throughout the five years during my PhD studies. He not only teach me how to do the research efficiently, but also help me improve my presentation skills and give me lots of opportunities to present my work in the national meetings. It's my great honor to be Dr. Wang's student, and I am really enjoy working in his lab.

I would also like to thank Dr. Stuart Anthony Allison and Dr. Markus W German for serving on my dissertation committee. Thanks very much for their questions and helpful suggestions for my research in every annual meeting.

I thank all my dear labmates in Dr. Wang' group: Yan Li, Juan Liu, Tanyu Wang, Zhenghua Tang, Maksim Kvetny, Warren Brown, Jonathan Padelford, Loubna Pagnotti, Tarushee Ahuja, Jie Jiang, and Cecil Conroy. I really enjoy working with them in the lab and having fun together in the spare time.

I acknowledge the fellowship from Brains & Behaviors (2013-2015), Georgia State University. The financial supports from GWang startup at GSU, NSF CHE-1059022 and ORNL FIRST EFRC of DOE (ERKCC61) are also acknowledged.

TABLE OF CONTENTS

LIST OF FIGURES

1 INTRODUCTION

The nanopores or nanochannels, referring to nanometer-sized holes across an insulating membrane, have received great attentions recently due to their fundamental interests in novel nanoscale mass transport features[1-3], and broad applications in molecular sensing[4-5], nanofluidics[6], energy storage and conversion[7-8], and membrane transport[9]. In a typical nanopore device, two large solution reservoirs are connected by single nanopore or an ensemble of nanopores, which allow the molecules and fluid to transport through under external driving forces. Due to the unique nanoscale geometry and strong interfacial interaction, the mass transport processes through nanopore are quite different from their bulk counterpart and display novel nonlinear and dynamic features.[10] An overall investigation of the mass transport processes through nanopores, at both transient and steady states, is therefore needed for both fundamental research and practical applications exploiting such processes. For example, most nanopores-based sensing is based on the quantification of the resulting transport current patterns.[11] The ion transport dynamics through nanoscale confinements are also important for those nanostructured electrodes in energy storage and conversion, since it directly determines the electrolyte resistance and power density. The rectified ionic currents have also been directly utilized to develop ionic diodes and transistors[12], and in nanofluidics devices for sample enrichment and desalination.[13-14]

With the advances in nanotechnology and nanofabrication, various biological and synthetic nanopores with desired geometry and surface properties have been successfully developed for different purposes.[15-16] The electrostatics and electrokinetic properties in the nanopores are generally described by classic electric double layer (EDL) structure at the substrate/solution in-

terface, in which many limitations and failures have been dicussed.[17] The mass transport processes through nanoscale confinements have been investigated by extensive computational simulation and experiments, and the nonlinear rectification currents are believed to origin from asymmetric symmetry in geometry and/or surface charge distribution in the nanopores.[18-19] Many factors including potential[20], surface charges[17], geometry[21-22], ionic strength[23], external pressure[24] and concentration gradient[25-26], affect the rectification behavior of the nanopores. However, most of these studies focus on the steady state conditions. The dynamics of the transport processes are of great challenge and remains rarely investigated.

In this dissertation, I am aiming at the fundamental understanding in the origins of the ionic current through nanopores, especially at the transient state. The dynamic mass transport processes through single nanopores are investigated with multiple experimental electroanalytical techniques and numerical simulations. The physical origin of different dynamic processes are proposed, and quantitatively correlated to the surface and geometry properties of the nanopore. The analysis provides new physical insights in the mass transport processes at nanoscale interfaces.

1.1 Biological and solid state nanopores

The development the nanopores are briefly introduced in this section first, including the fabrication techniques, nanopore geometry, and surface properties. The great advances in nanofabrication nowadays have offered many different nanopore platforms with desired geometry and surface functions. Biological channel proteins and synthetic solid-state ones fabricated from silicon, polymer and semiconductor materials can be integrated into devices that allow stable and reproducible measurements.

1.1.1 Biological nanopores

Various ion channel proteins and pore-forming peptides and toxins have been reconstituted into lipid membrane to form the biological nanopores for single channel recording.[16] One of the most widely used biological nanopores is the α-hemolysin, which has a 1.4 nm diameter limiting pore at the narrowest opening and ca. 10 nm height, serving as a perfect platform for the sequencing of single-strand DNA (~1 nm). The performance of the α-hemolysin can be improved through chemical modification or genetic mutation, i.e. mutation of interior amino acids[27] and incorporation of molecular adaptors with proper sizes. Other biological nanopores including MspA[28] (1.2 nm diameter), aerolysin[29] (1.0 nm diameter), ClyA[30] (3.3 nm diameter) have also been developed for sensing molecules with different sizes. However, the biological nanopores and lipid layer are generally too fragile to bear harsh environmental conditions, and the resulting transport noises are generally very high.

Therefore, the synthetic nanopores have been recognized as promising alternatives due to the easy fabrication and characterization techniques, good thermal and mechanical stability, adjustable geometry and surface properties, and capability to be integrated into large arrays.[15] Based on the substrate materials, a variety of techniques have been applied to fabricate nanopores and nanochannels with stable and well-defined nanoscale geometry.

1.1.2 Silicon-based materials

The silicon materials (including Si, Si_3N_4, and SiO_2) are the most commonly used materials to fabricate the nanopores. Well-developed lithography techniques in microelectronic fabrication have been employed including wet and dry etching, electron beam[31], ion beam[32], and photolithography sculpting[33]. Single nanopores in the range of 2-20 nm radius were fabricated through

the silicon nitride membranes with electron beam from a field-emission TEM.[34] The geometry of the nanopore are found to be affected by two processes and a low-impedance hydrocarbon layer was found to be formed on the pore surface. The electron beam etching is suitable for thin membranes (< 50 um) since the energy is relatively low and the drilling rate is slow. The ion beam technique, on the other hand, shows better selectivity, reproducibility and thus is suitable for any membrane thickness,[32] but the drilled nanopores generally have large radius (> 5 nm) due to the high energy employed. For the silicon substrate, the etching source would always be plasma and the resulting nanopores display inverted-pyramid geometry.[35] Conical nanopores have also been fabricated through silicon substrate with a metal nanoparticle assisted plasma etching.[36]

The glass capillaries, mainly borosilicate and quartz materials, have also been widely used to make single nanopores due to the easy fabrication procedures.[37] The etching and pulling methods are the two popular fabrication methods. White's group develop the bench-top method[38] to fabricate single nanopores in glass membrane: an electrochemically etched gold or platinum nanotip can be encapsulated into a glass capillary via thermal heating/melting of glass; the following polishing, etching and removing of the tip would leave a conical nanopore through the glass membrane. The geometry of the nanopore replicate the geometry of gold and platinum nanotip, which can be controlled by the electrochemical etching processes.[39] The resulting radius of the conical nanopores is generally in the range from 20 to 100 nm, and the thickness of the membrane is around 50 μm. Needle-like quartz glass nanopipettes can also be easily and quickly fabricated with a laser-heated mechanic puller.[40] The opening of the fabricated nanopipettes can be as small as 20 nm. The geometry and size of the pulled pipettes can be

controlled by various pulling parameters, i.e. force, heating time, and pulling time, though not with a high precision.

The surface active group of the silicon/silica materials are generally Si-OH. At least two surface pKa are observed on the planar surface: 4.9 for the isolated Si-OH, and 8.5 for the Si-OH group that could form hydrogen bond with a neighboring one, either directly or via water molecule.[41] The density of surface active groups is around 5 per nm^2. The percentage and distribution of those silanol groups vary in the materials and devices from different fabrication methods and parameters. In general, the surface charge densities of the silicon-materials based nanopores at ambient aqueous solution (pH = 6-7) would be below 1 e/ nm^2, or 0.16 C/m^2.[42] The surface of these silicon based nanopores can also be easily controlled and modified by chemical modification.[43] Through saline chemistry, different groups can be modified on the surface to improve their performance, or make the surface sensitive to the pH, light[44] and temperature.

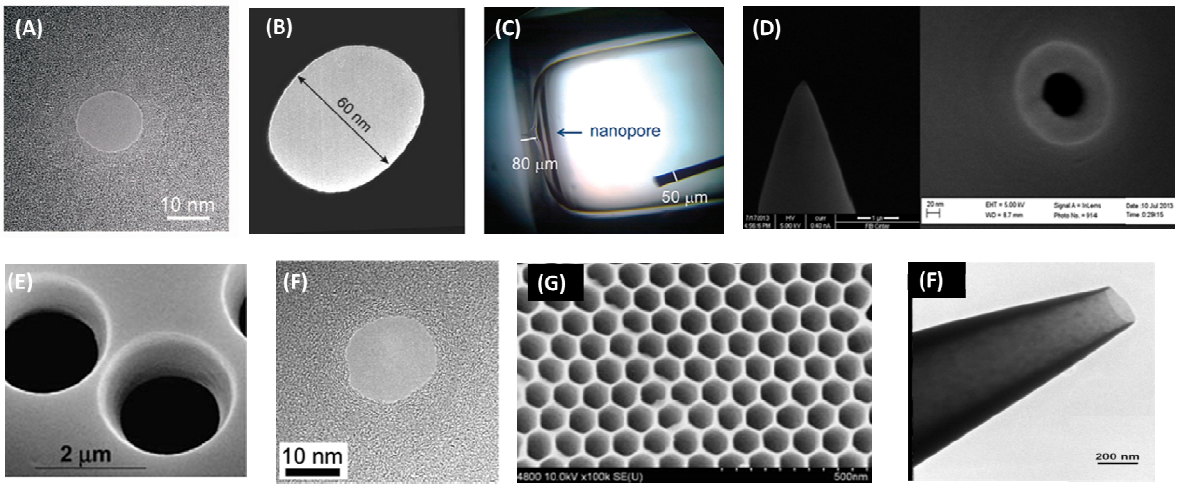

Figure 1.1 Synthetic solid state nanopores. Dependent on the fabrication techniques and substrate materials, various size and shape of the nanopores can be fabricated. (A) SiN substrate with electron beaming sculpting, (B) SiN substrate with ion beam sculpting, (C) single conical glass nanopore fabricated from bench top method, (D)quartz glass nanopore fabricated from laser pulling, (E) PET polymer nanopore fabricated from ion-track etching methods, (F)

graphene nanopore from electron beam sculpting, (G) Al2O3 nanopore arrays, (H) carbon deposited nanopipettes. Panel A was reprinted with permission from ref 34. Copyright 2006, American Chemical Society. Panel B was reprinted with permission from ref 32. Copyright 2001, Nature Publishing Group. Panel C was reprinted with permission from ref 39. Copyright 2012, American Chemical Society. Panel D was reprinted with permission from ref 45. Copyright 2015, Royal Society of Chemistry. Panel E was reprinted with permission from ref 46. Copyright 2003, Elsevier. Panel F was reprinted with permission from ref 34. Copyright 2010, American Chemical Society. Panel G was reprinted with permission from ref 47. Copyright 2009, Springer. Panel H was reprinted with permission from ref 48. Copyright 2014, American Chemical Society.

1.1.3 Polymer nanopores

Polymer nanopores, such as poly(ethylene terephthalate) (PET)[49], and polycarbonate (PC) are also good insulating substrates for nanopore fabrication. Ion tracking etching methods are widely used to etch through the membrane.[50] Briefly, one side of the polymer membranes were first irradiated with heavy ions, and chemical etching was followed on the other side to expose the nanopore.[46] The resulting geometry of the nanopore would always be conical, and the opening could be controlled to be 2 nm or larger. The resulting surface active group is –COOH, and its surface active site density would also be around 1 e /nm^2 with a surface pKa of ca. 3.8.[51] Similar to the silicon based materials, the interior surface of the polymer materials can also be easily modified through amide chemistry.[52]

1.1.4 Other nanopores and nanopore arrays

The nanopore arrays will maintain the unique function of individual nanopore and improve the transport efficiency. Several techniques have been developed to fabricate the arrays. The anodic alumina oxides (AAOs) is one of the most used nanopore arrays.[48] Well-defined self-ordered AAO nanoporous membrane can be fabricated through aluminum anodizing in acidic or alkaline solutions. The geometry of each individual nanopore is cylindrical with a radius ranging from 2 to 100 nm. The AAOs can also serve as template to synthesize nanotube arrays of other

materials.[53] The surface active group in Al_2O_3 is generally Al-OH and the surface pKa is around 7-10, so that positive charged surface is expected for Al_2O_3 at ambient solution pH. [54]

The thickness of the membrane substrate as nanopore support can be further decreased to single atom layer by using 2D sheet materials such as graphene, BN, and MoS_2.[55-56] Ion beam is usually used to drill a small hole across the 2D sheets. In additional to its minimal thickness, graphene can serve as both membrane substrate and electrodes due to its unique conducting properties. In DNA sequencing applications, single-base resolution is expected by recording the conductance of the nucleotide in the transverse direction.[55]

The nanotubes with well-defined structures also serve as good platforms for nanoscale transport studies. Carbon, BN, TiO_2, gold and self-assembled organic nanotubes have been developed.[57-58] The size of those nanotubes can approach sub-1 nm in diameter, in which case the Van der Waals interactions, hydrogen bonds, and hydrophobic interaction become more pronounced, leading to new transport characteristics. A particular intriguing observation is that water transport speed has been found to be super-fast in carbon nanotubes.[58] BN nanotube with an extremely high surface charge densities have also been fabricated and applied in the osmotic applications.[59]

To actively control the surface properties, the internal surface of the nanopores can be further modified or deposited with conductive materials, i.e. gold,[60-61] or carbon materials[48], which act as a gating electrodes to actively control the electric field and ion concentration inside the nanochannel. The resulting current signal analysis is generally complicated.

1.2 Electric double layer (EDL)

At the nanoscale dimension, the interaction between the surface charges and mobile solution ions becomes predominant, which result in novel electrokinetic features in the transport through the nanopores. Size exclusion and other short range interactions also make significant impacts at atomic and molecular scale. The excess charges, origin from the surface group dissociation and/or ion adsorption-desorption, will attract counter ions from the bulk solution to compensate the surface charges. A layer of counter ions is physisorbed on the interface referred as Helmholtz layer. Other counter ions are not firmly attached to the surface but distributed within the proximity. This dynamic distributed layer is often called diffuse layer. Poisson-Boltzmann (PB) model has been employed to describe the potential and concentration distribution in the diffuse layer. With the assumption of point ions, continue liquid, and constant dielectric constant, the Gouy-Chapman model is developed based on the PB theory to describe the EDL structure. In the case of weakly charged surface (< 100 mV, or 0.1 C/m^2), the surface potential (V_0) display a simple exponential decay with respect to the distance *x* away from the surface in dilute electrolyte solutions:

$$V = V_0 e^{-x/\lambda} \qquad \text{(Eq 1.1)}$$

The decay constant (λ), defined as the Debye length, is a characteristic parameter to describe the diffusion layer thickness. Under normal experimental conditions, its expression can be simplified as:

$$\lambda = 0.3/\sqrt{c}\ (nm) \qquad \text{(Eq 1.2)}$$

The Debye length obvious mainly depends on the ionic strength of the solution, *c*. The ratio of the distance from the surface (or nanopore size in this dissertation) and Debye length (r/λ)

can therefore be used to evaluate the surface effects. For pores with large radius or in high ionic concentration, which has a large r/ λ ratio, the transport features will be very similar to the bulk behaviors. On the other hand, with small pore size or low ionic strength, the surface effect becomes more dominant.

The charged surfaces attract the counter-ions and repel the ions with the same polarity. This charge selectivity feature would make the counter ions the main charge carriers in the nanopore. Accordingly, the ionic conductance of the nanopore is mainly determined by the counter ions in the diffuse layer, or the surface charges of the nanopores if assuming the charge balance in the nanopores. The charge selectivity governed by long range electrostatics in nanopore is therefore fundamentally different from classic membrane-based separation and related applications. Experimentally, plateau ionic conductance was observed from the nanochannels at low ionic strength, this conductance can also be used to evaluate the surface charges of the cylinder nanochannels.[62]

1.3 Electrokinetic transport

Different external forces can drive the fluid and molecules through nanopores, including electric field, pressure, and concentration gradient. Due to the EDL structure and charge selectivity of the nanopores, asymmetric cations and anions transport will lead to very interesting transport features that are suitable for different types of applications.

Electric gradient. The electric field is the most widely used driving force, since most analytes are either small ions or larger species carrying charges. For the potential that is applied across the whole membrane, most of the potential drops in the most resistive region, thus resulting in an extreme high electric field near the pore orifice.

This external field, superimposed with the surface electric field, governs the migration process of the ions. The transport signals, in the form of ionic current or conductance, reveal both surface and applied potential effects. Different external potential waveforms have been applied across the nanopore to investigate and control the mass transport features at both transient and steady states. Cyclic linear/triangular sweeping potential waveform[63-64], AC impedance[65], constant or stepped potential, and current clamping are representative methods employed. Noise analysis in some of those measurements have been performed as well.[66]

Concentration gradient. The concentration gradient is another common force that drive the ion transport through nanopore, analogy to many biological ion channels transport mechanism. Following the Fick's law, both cations and anions would diffuse through the nanopore from the high concentration to the lower ones. Due to the EDL and charge selectivity of the nanopore and their respective diffusion coefficient (ion mobility), uneven transference numbers of the cations and anions would result in a net current/potential signal. A transmembrane potential is established and can be simply described by the Nernst equation:

$$E = zF/RT \ln (c_1/c_2) \qquad \text{(Eq 1.3)}$$

where c_1 and c_2 are the concentration at the two sides of the nanopore/membrane. The concentration gradient across the nanopore membrane could be used as a promising energy harvesting approach, by converting the concentration gradient into output potential or current. Experimentally, it is worth pointing out that the measured potential from concentration gradient across the membrane would also include the asymmetrical formal potentials of the two electrodes in different concentrations. For example, the formal potentials of the commonly used Ag/AgCl electrodes depends on the concentration of the KCl solution.

Pressure gradient. Pressure is another force to drive the fluid, non-selectively for ions and neutral molecules. The pressure needed to drive the fluid transport through the nanopore could be extreme high. As more counter ions are in the diffuse layer, the movement of the fluid would also result in a net current flow, which is known as streaming currents/potentials. The streaming current could be proportional to the applied pressure, and of course strongly depend on the surface charges. The streaming potential/current is a typical method to calibrate the surface charges of the substrate in capillary transport.

Thermal fluctuation/ Brown motion. Brownian motion of the ions or molecules in the liquid also plays an important role in the mass transport[67] process through nanopores, such as DNA sequencing.[68] Although random in nature, the transport through individual nanopores might not generate sufficient transport activities to satisfy ensemble statistics.

1.4 Modeling of the mass transport through nanopores

The nanopore transport features are extensively investigated via various simulation methods, in which the nanopore geometry and surface properties can be easily defined and optimized. In addition, the simulation also offer better fundamental insights into the electrostatics and concentration details inside the nanopore, which cannot be directly accessed in experimental methods. The commonly used simulation approaches span over multiscale from classic Poisson and Nernst-Planck and Navier-Stokes equations (PNP-NS model) to molecular dynamics (MD). In the simulations, the geometry of the nanopore is built first, and the governing equations and boundary conditions are then defined.

PNP model: The PNP model is based on a mean-field approximation. Both ion concentration and electrical potential distribution are assumed to be continuum. The electrostatics inside the

nanopore, i.e. the surface charges and external potential, are described by the Poisson's equation. The mass transport processes, including migration and diffusion, are calculated by the Nernst-Planck equation. The Navier-Stocks equations can be coupled to describe the convection processes such as pressure-driven or electroosmotic flows in the nanopore. Briefly, after defining the nanochannel geometry based on experimental characterizations, a simplified model can then be established with proper boundary conditions addressing certain properties. After applying external driving forces, the ion flux at selected cross sections, often at one of the electrodes, can then be integrated to obtain the resulting transport current. By tuning the corresponding parameters and boundary conditions, the transport current in experimental studies can be either qualitatively or quantitatively fitted by the simulation.[63, 69] In general, the PNP model works very well to explain steady-state experimental ion transport features from nanopores larger than few nanometers. The surface charges can be elucidated by fitting experimental potential-current responses in simulation studies. In addition, the rectified, oscillated, and hysteresis current responses have been successfully simulated from the nanopores with proper surface and geometry boundary conditions. However, since the PNP model is still a continuum theory, molecular-level descriptions of the interactions between ions/ions and ions/walls is not considered that could explain some unaddressed phenomena.

MD simulation. MD simulation generally offers more quantitative insights in the structure, dynamics and energy of the solid-liquid interfaces with more rigorous force field and molecular level definitions. MD simulations have reproduced well-known nanopore transport features such as ionic current rectification and DNA molecule transports.[70-71] Besides, new features such as quantized ionic conductance and memcapacitive effects have been observed in nanopore

transport recently.[72] However, the MD simulation is very time consuming and has high demand in computation resources because the simulation size is always very large. The simulation is generally limited in the time range of nanoseconds and few nanometer dimension at the most.

1.5 Surface charges in nanopores

In most nanopores, the surface charges play a key role in the mass transport processes, thus its density and distribution are the key parameters to the nanopore transport. Several methods have been used to characterize the surface charges in nanopores. In nanopores, the surface charges originate from the surface group dissociation/ion adsorption. Despite the surface nature of the materials and fabrication techniques, the pKa of the surface group under the nanoscale confinement could be affected by many other factors, such as surface adsorption, electric field, and ionic strength. In this section, I will briefly summarize these important factors that influence the surface charges of the nanopores.

Surface adsorption. At ambient solution pH, the surface of most synthetic nanopores is negatively charged. However, the surface charges are found to be reversed in polarity when the transport cations have multivalence and their concentration is relatively high, such as Ca^{2+}, Co^{2+} and $Cosep^{3+}$.[73-74] The surface adsorption and over screening mechanism are proposed to explain the surface charge inversion. In addition, the cations can also be trapped in the gel layer formed at the substrate-solution interface, such as glass-water, or PET-water interfaces. Extra trapped cations can also change the polarity of the surface.

Ionic strength. The protonation/deprotonation equilibrium of the surface active group is also affected by the ionic strength, as higher ionic strength will enhance the breakdown of the O-H bond by better stabilizing the produced charges (i.e. surface-O^- and H^+). Experimentally, the sur-

face charges of the carbon nanotube in 100 mM KCl are found to be 50 times higher than the value in 1 mM KCl based on the fluorescence intensity.[75] Taking into account of the confined nanogeometry and concentration polarization, the enriched/depleted concentration inside nanopores could have unexpected effect on the intrinsic surface charges retrospectively.

External Electric field. Ion transport driven by the external electric field is called migration. Due to the small nanoscale opening, the external potential will mainly drop at the narrowest nanopore region and establish an extremely high electric field (i.e. 1 V/100 nm=10^7 V/m). The extreme high E field could affect the distribution of the surface charges along the pore wall/substrate greatly. Such high electric field could be sufficient to change the dissociation constant of the H_2O molecules, altering the local H^+ concentration and thus surface charges.[76]

Non-uniformly SCD. Various non-uniformly distributed surface charges have been proposed based on specific experimental conditions. An exponential decay surface charges distribution was proposed by Juan et. al,[69] through which the simulated rectified currents show very good agreement with the experimental results, especially at the low conductivity states. Other type of nonuniform, including linear, bimodal and hyperbolic SCDs, have also been proposed primarily in simulation work that requires experimental validation.

1.6 Asymmetric mass transport

Affected by both the nanopore geometry and surface charges, the mass transport processes through nanopore generally include many different processes and thus are very complicated. The nanopores have a variety of geometries, such as conical, bullet, and trench shape, determined by the fabrication techniques and applications. In most cases, asymmetrical nanopores display more interesting and unique but unfortunately more complicated mass transport fea-

tures compared to the nanopores with symmetrical geometry. The broken symmetry of the nanopore could be either asymmetrical nanogeometry or surface charge polarity and distribution.

1.6.1 Transport limiting zone

The conductance of the conical nanopore is quite different from the cylinder ones. For the conical nanopore, the total resistance would be the sum of the nanopore resistance and the access resistance (pore opening to the electrode), expressed as[77]:

$$R_p = \frac{1}{\kappa r}\left(\frac{1}{\pi \tan\theta} + \frac{1}{4}\right) \quad \text{(Eq 1.4)}$$

where κ is the conductivity, r is the radius, and θ is the half cone angle. Because the depth of the nanopore is significantly larger compared to the pore radius, mass transport is limited by the most resistive zone only near the smallest pore orifice region. For example, in a typical 40 nm-radius nanopore, the transport limiting zone would be around the first hundreds nanometers. This interesting feature would make the conical nanopore a promising platform to realize the sensing at molecular level, i.e. single molecule detection. The high sensitivity is achievable through localizing the signal-limiting zone to nanoscale and better surface controls. The radius of the nanopores can be conveniently calculated from the Eq 1.4 with a known half cone angle and volumetric conductivity. The ionic conductance should be measured in high electrolyte concentration (i.e. 1 M) and small potential perturbation (i.e. 0.05 V) to exclude the surface charge contribution.

1.6.2 Concentration polarization

The ionic concentration polarization (ICP) is a common and important phenomenon that have been observed at electrode surface, membrane transport and micro- and nanofluidics. Driven

by the external sources, such as potential and pressure, the concentration profile in the transport limiting zone can be polarized, either enriched or depleted with respect to the bulk. This ICP are the physical origin of many interesting current patterns in the nanopore transport, and have also been applied in developing nanofluidics or membranes for sample concentrator or desalination.[13-14]

The potential-dependent concentration enrichment and depletion at the transport limiting zone lead to the high and low conductivity states of the nanopores, well known as ionic current rectification (ICR). The ICR is found to be a slow dynamic process responding sluggishly to the external stimuli. Pinched hysteresis current loops were observed from the nanopores when applying a sweeping external potential waveforms, and an intriguing non-zero cross point, which represent the averaged surface potentials was found to separate the concentration enrichment and depletion.[64] During the enrichment process, or at high conductivity states, the current loops were inductive while regular capacitive loops were displayed during the depletion process at the low conductivity state. However, the ICP processes in the nanopores have been rarely studied, not mentioning its quantitative description.

1.6.3 Ionic current rectification

The most well-known transport features in asymmetrical nanopores would be the ionic current rectification (ICR). In ICR, the current at certain potential is much higher than that at the same potential amplitude but opposite polarity, referred as high and low conductivity respectively. Many physical models have been proposed to describe this interesting phenomenon. Briefly, the high and low conductivity states are resulted from the potential-dependent concentration polarization process.[18, 78] The rectification factor (RF), the current ratio at the same po-

tential amplitude but opposite polarity, is often used to describe the non-linearity of the current-potential curves. Originated from the potential induced ICP inside the nanopore, the ICR and RF depend on many factors, which will be briefly summarized next.

Potential. Besides the nonlinear rectified current-potential relationships, the transport current is found to reach a threshold at relatively high potentials. The correlation between the potential and limiting current has not been fully understood and quantified. Under extreme high potentials, the water molecules can be split near the pore orifice. The interesting activity at extreme high potentials has been employed to generate small bubbles, clean the nanopores, and other applications.

Surface charge. The most straightforward demonstration of surface charge effects would be the pH dependent ICR in various nanopores.[79] In theory, the RF increases as the surface charge density increases. Various studies have been reported to modify the surface groups to either increase or decrease the RF values. ICR diminishes if the surface charges are neutralized even in nanopores with asymmetric geometries. Both uniform and nonlinear surface charge distributions have been proposed and studied in simulation work, among which a gradient SCD distribution along the pore wall provided satisfactory fitting of experimental results.[80] Experimentally, the nanopores with bipolar distributed surface charges have been fabricated and a very large RF was obtained.[81]

Electrolyte concentration. The ionic strength effect on the rectification behavior is not simple. A maximum RF value is observed at a medium solution concentration (ca. 50 mM), while both higher and lower ionic concentration would result in decrease of the RF values for nanopores in the size range of few to lower tens nanometers.[20]

Geometry. Although it is widely accepted that the size of the nanopore orifice determines the mass transport features of the nanopores, it has been shown that different asymmetrical geometries such as conical, bullet-like, cigar-shape, increasing half cone angle, and depth also affect some transport features.[21-22] Besides the different volumetric conductance, the EDL structure will be affected by the geometry as well.

1.6.4 Dynamic transport processes

Though steady state transport features in nanopores have been well studied, little is known about their transport dynamics. This important topic remains rarely studied primarily due to the great technical challenges for measurements and analysis. The RF was observed to decrease from conical nanopores when the scan rates of the potential increased in both simulation and experiments.[82-83] Previous AC impedance results have demonstrated multiple dynamic processes with different time constants are involved in the mass transport processes through conical nanopores.[65] Specifically, two semicircles are displayed in the Nyquist plot, suggesting two dynamic processes are involved in the ion transport processes. The first process at high frequency domain is relatively consistent to be resistive-capacitive at all different potentials while the second dynamic process at low frequency range is polarity dependent. Regular capacitive features are observed at negative potentials, while inductive behaviors are discovered at the positive potentials. The polarity dependent dynamic transport process is attributed to the electrostatic interaction between the charged surface and mobile ions in the bulk solution.

Built upon the aforementioned literature studies, the dynamic mass transport processes through single nanopores are investigated in this dissertation. An interesting hysteresis response as pinched current loops is observed from the nanopores under sweeping potential. The

current loop at the high conductivity states is inductive, while the loop at the low conductivity states are inductive. More interestingly, these two loops are separate by a constant non-zero cross point in i-V plots. This cross point are found be independent of the external potentials, both the amplitudes and scan rates. Chapter 2 mainly focus on this interesting feature.

When further increasing the frequency or scan rates of the sweeping triangular potential, the cross point starts to shift to more positive potentials, and a new cross point develops near the switching potential. Through numerical simulation, by simulating the current responses with and without glass membrane substrate, I successfully differentiate the transport current from charging-discharging current of the exterior surfaces at the extreme scan rates. The experimental results have been well fitted by the numerical simulation with proper boundary conditions. These findings are included in chapter 3. The chapter 4 further explore the intriguing non-zero cross point. The full physical meaning of the cross point is elaborated and correlated to the surface and geometry properties of the nanopores.

The dynamic ion concentration polarization in nanopores is quantified through charge analysis of the pinched hysteresis i-V curves, as included in chapter 5. The full dynamic picture of the concentration enrichment and depletion is provided. The charge depletion is relatively constant in different concentrations and nanopore geometry, which is believed to directly reveal the surface charges inside the nanopores.

The charging dynamics at constant potentials is quantified in chapter 6 through potential-step analysis. Different charging dynamics are observed at the high and low conductivity states respectively, from which the current contributed by polarized concentration and the corresponding time constants are quantified. Based on these findings and quantifications, an empiri-

cal equation was proposed and validated by the numerical simulations. The empirical equation is believed generalizable to quantify and predict the current-potential relationship of various nanopores.

2 SURFACE POTENTIAL IN SINGLE CONICAL NANOPORES AND RESULTING MEMRISTIVE AND MEMCAPACITIVE ION TRANSPORT

(This chapter has been published as "Wang, D. C.; Kvetny, M.; Liu, J.; Brown, W.; Li, Y.; Wang, G. L., Transmembrane Potential across Single Conical Nanopores and Resulting Memristive and Memcapacitive Ion Transport. *J. Am. Chem. Soc.* **2012,** *134*, 3651-3654." Reprinted with permission from Ref 64. Copyright 2014, American Chemical Society.)

Memristive and memcapacitive behaviors are observed from the ion transport through single conical nanopores in SiO_2 substrate. In current-voltage (*i-V*) measurements, the current is found to depend on not only the applied bias potential, but also the previous conditions in the transport-limiting region inside the nanopore (history-dependent, or memory effect). In *i-V* curves measured at different scan rates, a constant cross-point potential is observed that separates the low and high conductivity states in the rectified ion current. The hysteresis loop in the low conductivity state follows normal capacitive responses, while the loop in the high conductivity state appears to be negative with respect to the applied potential waveform. The interesting memory effects are attributed to the finite mobility of ions as they redistribute within the negatively charged nanopore under applied potentials. The cross-point potential between the two hysteresis loops approaches an asymptote upon the increase of electrolyte concentration. The effective surface potential across individual nanopores is obtained based on the quantitative correlation between the cross-point potential and electrolyte concentration.

2.1 Introduction

Memory effects refer to the responding signal being determined not only by external stimulus, but also the former states or the history of the system.[72] In electronics, resistive, capacitive, and inductive elements with memory effects differ from their traditional counterparts in that their magnitudes vary with time rather than being constant values. The resulting history-dependent properties are defined as memristive, memcapacitve and meminductive behaviors respectively.[84] The memory effects originate from the dynamic properties of charge carriers (electron or ions).

Ions transport (IT) confined at nanometer scale pores and channels have received considerable interests recently.[1, 3, 85] Strongly affected by nanodevice geometry and charged interface, interesting diode-type non-linear *i-V* conductivity responses are frequently observed under steady-state (S-S) measurements, known as ionic current rectification (ICR).[86-87] The non-steady-state and S-S IT affected by the structurally-defined nanoscale confinement unveil fundamental information vital to the further development of nano-electronics and high-density electrochemical energy storage and conversion devices.[8] For example, this IT process directly reflects the charging and discharging of a supercapacitor with non-parallel electrode surface (electrochemical capacitor) at nanometer scale.

Artificial solid-state nanopores and nanochannels can be regarded as mimics of protein ion channels, and have been developed for sensing applications.[88] The current signal, resulting from the movement of ions, is determined by the most resistive region, normally close to the smallest cross-sectional area in the pore channel. Based on Coulter-Counter concept, various nanopores and nanochannels are developed for single molecular sensing, single nanoparticle

trafficking and DNA sequencing.[89] Dynamic responses of IT at non-steady-states are obviously more relevant to stochastic sensing applications, in which the signal is based on the disturbance of ion flux by the analytes at the signal-limiting nanopore region. Importantly, the distribution of ions flux is not uniform inside charged conical nanopore, determined by both external applied potential and intrinsic nanopore surface potential. Quantification of their respective impacts on ion flux would require information inaccessible by mostly used time-domain steady-state conductivity measurements.

Frequency domain impedance analysis of IT through conical nanopores reveals multiple processes with different time constants.[65] An apparent inductive response was detected at low frequency range (sub-1 kHz) in the high conductivity state, while additional capacitive feature is observed in the low conductivity state at comparable frequency range. The low frequency responses are induced by the electrostatic interactions of mobile ions (charge carrier for the detected current signal) with those fixed charges at substrate-solution interface. Interestingly, molecular dynamics simulation suggested negative capacitance in the IT through single nanopores. The proposed negative capacitance mechanism is in excellent agreement with the apparent inductive responses observed in impedance measurements.

In this chapter, time-domain and frequency-domain ionic current responses of single conical glass nanopores were analyzed. Under selected scan rates and potential ranges, interesting hysteresis loops corresponding to normal and negative capacitance in IT through single nanopores are discovered. The measurements directly reveal the memory effects in the IT near the charged interface at nanometer scale. Furthermore, the effective transmembrane potential across nanodevice substrate is non-invasively determined under measurement condition. In

analogy, the trans-membrane potential in biological cells is of great importance for many biological functions.

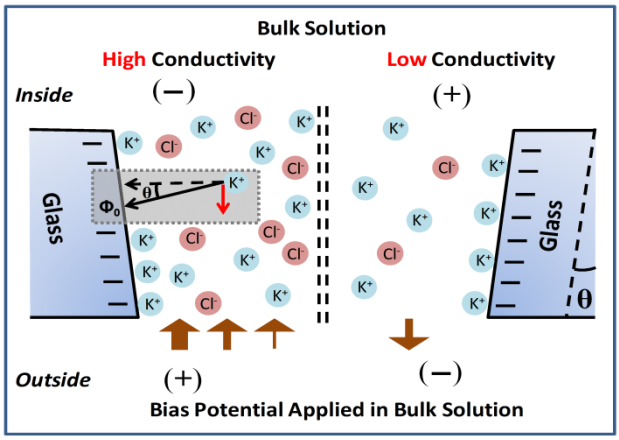

Figure 2.1 Visual representation of ion transport through a conical nanopore (half-cone angle θ). Visual representation of ion transport through a conical nanopore (half-cone angle θ). The left and right sides of the diagram illustrate opposite applied bias potential polarities that establish high and low conductivity states respectively. The block arrows at the bottom represent the corresponding K+ flux driven by the external bias potential. The impacts of surface potential to the K+ flux are illustrated in the dot-line-frame. Not drawn to scale. The figure was reprinted with permission from ref 64. Copyright 2012, American Chemical Society.

The high and low conductivity states of a conical nanopore during the measurements are illustrated in Figure 2.1. Nanopore preparation and electrochemical measurements follow previous reports.[38, 90] Basically, a conical glass nanopore is loaded with KCl solution (inside) and then immersed in the KCl solution at the same concentration (outside). Two Ag/AgCl wires were used as inside and outside electrodes to control the applied potential waveform (V_a) and to measure the responding current. The detected current signal is limited by the most resistive region along the whole circuit, originated from the ion flux near the nanopore orifice. Meanwhile, fixed negative charges at the substrate-solution interface (due to the deprotonation of silanol groups on glass surface) establish a surface potential profile. The parameter ϕ_0 corresponds to the surface potential induced by surface excess charges following classic double layer

description. In a conical nanopore (half-cone angle θ), the surface electrostatic field, perpendicular to the surface, will have a component along the direction of ion current, shown as red arrow in the gray dot line frame of Figure 2.1. This surface field component (correlation factor of sinθ) will establish an effective potential profile across the membrane (V_m) superimposed with the applied potential V_a. Note the component of electrostatic field normal to V_a does not directly affect the measured current but change the ion distribution within the nanopore.

2.2 Experimental section

Materials. Pt wire (25 μm diameter), silver wire (99.9985%, 0.5 mm diameter), and silver conductive paste from Alfa-Aesar were used as received. $CaCl_2$, H_2SO_4, HNO_3, H_2O_2 (30%) and acetone are from Sigma-Aldrich. Water (~18.2 MΩ·cm) was purified with a Barnstead E-pure water purification system. CORNING 8161 glass capillaries (OD = 1.50 mm, ID = 1.10 mm, Warner Instruments) were used.

Preparation of single conical nanopore membrane. The glass nanopores are fabricated followed the reported procedures. Briefly, the end of a Pt wire (length : 2 cm, radius: 25 μm) was electrochemically etched into a sharp tip using a waveform of 300 Hz at ~ 4 V peak to peak amplitude (BK Precision 4003A function generator). After sequencing washed in piranha solution and nanopure water, the sharpened Pt tip was sealed into a glass capillary by thermo-melting. This sealing process was monitored by an optical microscope (American Scope, USA). The Pt tip then is exposed by mechanical polishing the sealed end (Buehler Microcut paper discs 400-1200 GRIT). After further electrochemically etching to remove the Pt away, a glass membrane with a conical-shaped pore, replicating the geometry of the Pt tip, can be obtained by complete removal of Pt wire out the glass shroud.

Electrochemical Measurements. Voltammertric response and AC impedance spectra of the prepared glass nanopore membranes were studied with the potentiostat of Reference 600 (Gamry). In impedance spectra, the amplitude of the waveform was set to 10 mV while the recording frequency ranged from 500 mHz to 1 MHz.

Two Ag/AgCl wires were used as the electrode. The bias polarity is defined by electrode potentials outside versus inside the nanopore. The electrolyte is the KCl solution, used both inside and outside of the glass nanopore. The orifice radius of GNP membrane was calculated on the basis of the absolute current number at ± 0.050 V in 1M KCl solution following a previously described procedure.

2.3 Results and discussions

The current-voltage (*i-V*) responses of a 45 nm-radius nanopore at different scan rates in 10 mM KCl solution are presented in Figure 2.2. The *i-V* curves show obvious current rectification behavior in agreement with literature.[23] For conical nanopores with negatively charged surfaces, the high conductivity state is established if positive bias potential is applied externally relative to the inside electrode. By increasing the scan rate, the current amplitude slightly increases at the low conductivity state, but decreases more significantly at the high conductivity state. The overall reduction in the rectification factor as scan rate increases is qualitatively in agreement with previous experimental and computational studies by Zhang[83] and Girault[82], in which significant charging current was observed at much higher scan rates. The rectified ionic conductivity changes at different scan rates, indicating a time-dependent resistance, in accordance with the memristive effects described in electronics.

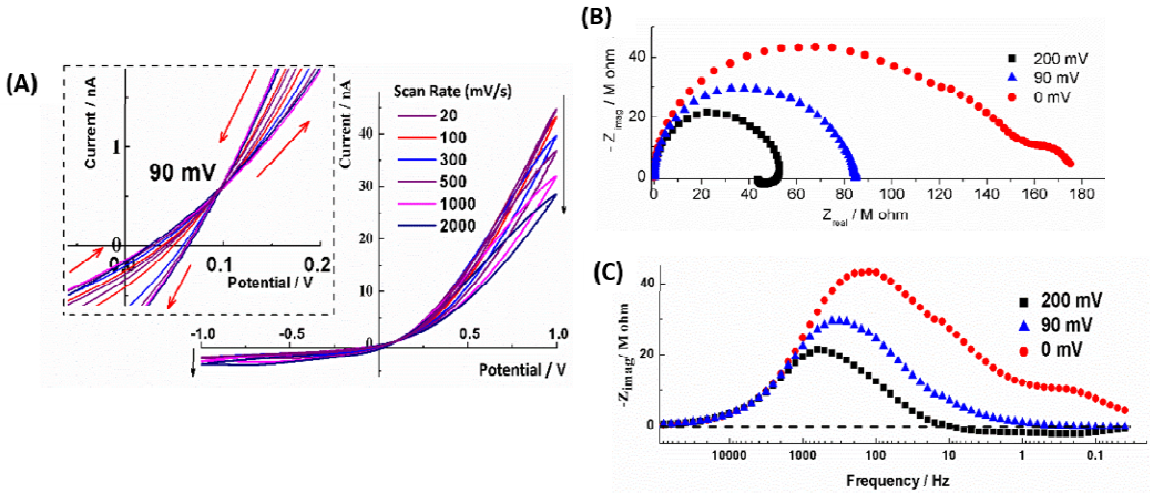

Figure 2.2 (A) The overlaid *i-V* curves at different scan rates in 10 mM KCl solution. Note the cross-point potential remains at 90 mV at all scan rates. The black arrows next to the curves indicate the changes in current with the increase of scan rate. The red arrows in the inserted panel illustrate the direction of potential scan. (B) and (C) show the impedance taken above, below, and at the cross-point potential in the form of Nyquist and Bode plot. The figure was reprinted with permission from ref 64. Copyright 2012, American Chemical Society.

Interestingly, the current amplitudes of different scan directions (i.e. -1.0 to +1.0 V versus +1.0 to -1.0 V) are different and cross at a common potential near zero. Two hysteresis loops are separated by this constant cross-point potential shown in Figure 2.2A. Analogous to the isosbestic point in spectroscopic measurements, this potential indicates the transition between the high and low conductivity states. As seen in the enlarged view in Figure 2.2A, the cross-point potential is independent of the scan rates. While the loop at the low conductivity state displays normal capacitive responses, the loop at the high conductivity state exhibits a "negative" capacitance with respect to a normal capacitive feature. In other words, the current is higher if the applied potential is scanned from higher to lower conductive state, i.e. from +1.0 V toward 0 V. The capacitive and ICR features are highly consistent for repeated scans, and are

independent of the initial potential or scan directions. The first scan is generally discarded in this analysis. The two hysteresis loops suggest that the ionic current depends on the previous states as well as the applied bias potential, referred as memcapacitive effects.

The normal and “negative” capacitive behaviors in low and high conductivity states are confirmed by impedance analysis. In the Nyquist plot (Figure 2.2B), an additional RC loop was observed at the low conductivity state (0 mV), while an apparent inductive loop in forth quadrant was observed at the high conductivity state (200 mV). The additional low frequency loops, better seen in Bode plot (Figure 2.2C), diminish if the DC bias potential was held at the cross point (90 mV). At the exact cross-point potential, a well-defined semicircle in Nyquist plot or a single peak in Bode plot indicates a simply one-time-constant mass transport process. With a slight deviation from this cross-point potential, the impedance spectra transforms from inductive to capacitive behavior or vice visa. The cross-point potential separates the signature of IT through the nanopore and reflects the nature of the nanopore geometry and surface charge.

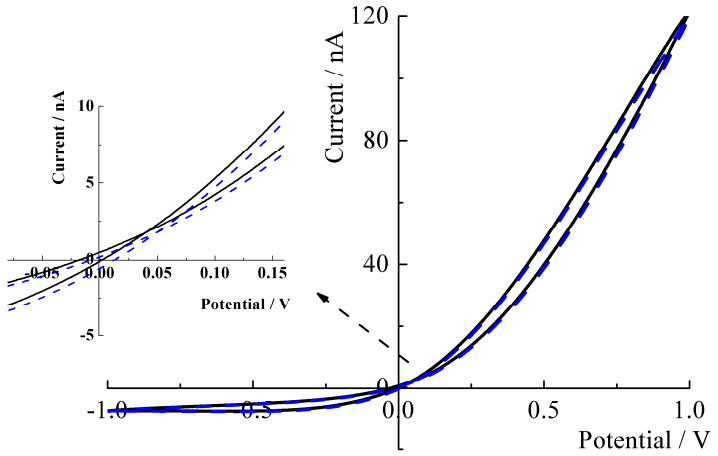

Figure 2.3 The i-V curves for switching the Ag/AgCl electrodes of the 50 nm nanopore in 100 mM KCl, and the scan rate is 500 mV/s. The inset shows zoom in part of crossing point potential. The non-zero cross point remains there, indicating a real property of the nanopore membrane. The figure was reprinted with permission from ref 64. Copyright 2012, American Chemical Society.

A constant cross-point potential connecting two hysteresis loops at different scan rates in *i-V* curves has been observed from other nanopores (more than 10). Furthermore, the cross-point potential is confirmed to be largely independent of asymmetry of the two Ag/AgCl electrodes. By switching the position of the inside and outside electrode, a slight shift at ca. 5-10 mV was observed, as shown in Figure 2.3. The value is much less than the cross-point potential. Those highly reproducible results rule out the possibility of measurement artifacts such as electrode preparation or instrumental offset.

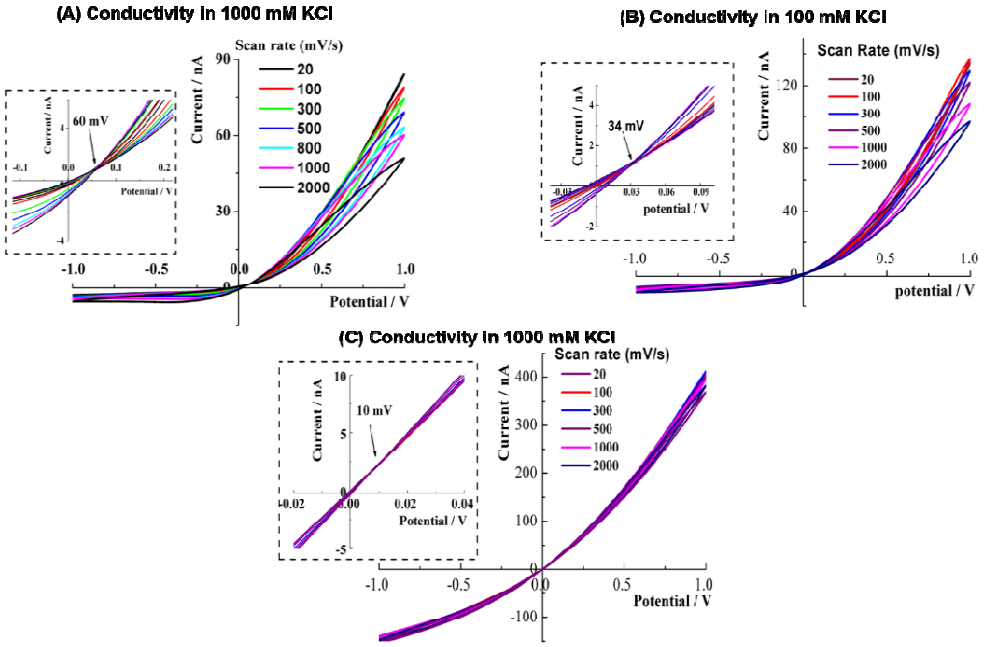

Figure 2.4 The i-V curves for the 50 nm-radius nanopore at different scan rates in(A) 50, (B) 100 and (C) 1000 mM KCl, the insets are the zoom in part near the cross point.

The non-zero cross-point potential is independent of scan rate, but varies in different electrolyte concentrations, as shown in Figure 2.4. In each concentration, the pinched hysteresis current loops are displayed with a constant non-zero cross point. More interestingly, the cross-point potential, referred as effective transmembrane potential V_M, decreases and approaches an asymptote upon the increase of electrolyte concentration. We quantify the correlation between the cross point potential and the ionic strength in the Figure 2.5. Quantitatively, the cross-point potential is found to display an exponential dependence with the square root of concentration, expressed as

$$V_M = V_0 \exp(-C^{1/2} / A) + V_e \qquad \text{(Eq 2.1)}$$

Where C is electrolyte concentration, A is a constant related to temperature, V_0 is effective surface potential, and V_e addresses non-ideal factors in the measurement. This is further illustrated by the excellent linear fitting in the inserted plot. This correlation is directly adapted from the Debye length description in classic double layer theory. The fixed negative charges at the glass-solution interface establish a surface potential profile and double layer away from the surface. The surface potential will in turn affect the IT driven by the external applied potential. As the electrolyte concentration increases, the electrostatic interactions between mobile ions and surface charges are more effectively screened. Correspondingly, the cross-point potential, which reflects the effective surface potential along the transport direction, will decrease. The value of V_0 is obvious significant, representing the surface potential (ϕ_0, Figure 2.1) determined by the excess surface charges or the charge density on the effective interior surface area. From the plot, the V_0 is found to be 153 mV for this specific nanopore. If the electrostatic interaction becomes negligible at sufficiently high electrolyte concentration, the cross-point potential should approach zero. Experimentally, thermal fluctuations, solubility of the electrolyte, and the asymmetry of the two Ag/AgCl electrodes limit the measurement resolution, expressed in Eq 2.1 with V_e at ca. 5-10 mV. Since the surface electric field is determined by electrolyte concentration, nanopore geometry, and surface excess charges, the cross-point potential is therefore independent of measurement condition such as scan rate.

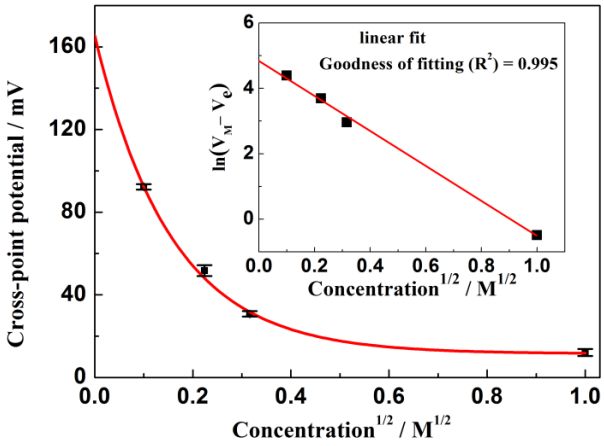

Figure 2.5 The correlation of electrolyte concentration with the cross-point potential. At each concentration, the cross-point potential was averaged from the i-V curves with scan rates ranging from 100 to 2000 mV/s. The fitting was performed with the equation of $V = V_0 \exp(-C^{1/2}/A) + V_e$, and its nature logarithm form is in the inserted plot. The figure was reprinted with permission from ref 64. Copyright 2012, American Chemical Society.

Next I demonstrate the diverging capacitance and charge-potential (Q-V) dependence to correlate with the theoretical predictions of nanopore memcapacitance.[2] The memory effects can be quantitatively described by the change of charges at specific potentials. Under a triangle scanning potential waveform, the instantaneous transported charge *Q* in Figure 2.2 is calculated from

$$Q = I \times \Delta t = I \times \frac{\Delta V}{v} \qquad \text{(Eq 2.2)}$$

where *v* is scan rate, *I* is the measured current. The potential step (ΔV) was at 1 mV interval. Note this is the instantaneous transported charges through the nanopore. Unlike the typical capacitor charging and discharging process, the charge continues to accumulate at the high conductivity state, even though the bias potential decreases, or discharging the nanopore (shown as the process 4 in Figure 2.4). The gap between the two curves (i.e. segment 4 vs. 3 or 1 vs.6) directly reflects the memory effects. Inserted in Figure 2.4, the history-dependent capac-

itance (calculated by C = Q/E) is evident with the dashed line highlighting zero, and the crossing of curve 3 and curve 4. The full dynamics of the transport charges are discussed in chapter 5.

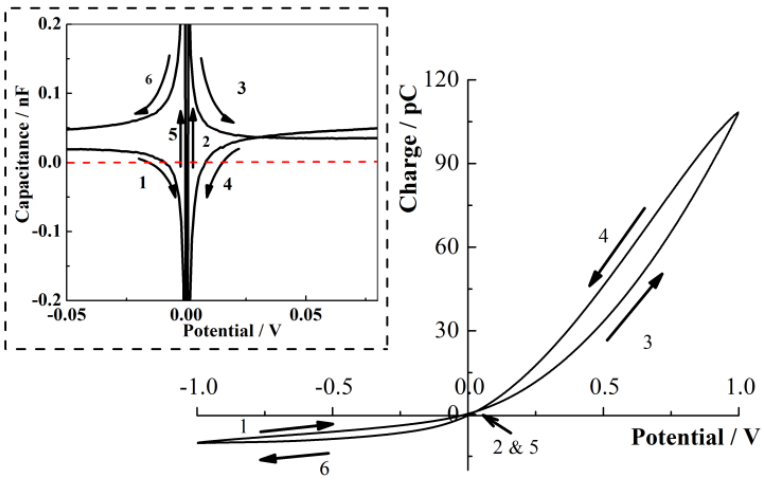

Figure 2.6 Memory effects of transported charges and nanopore capacitance (as inset) at controlled potential. The data was collected in 100 mM KCl solution at scan rate of 1 V/s. The arrows and numbers along the curve indicate the direction of potential scan. The inset is the relationship of calculated capacitance and potential. The figure was reprinted with permission from ref 64. Copyright 2012, American Chemical Society.

The mechanism of the observed memory effects is proposed in the context of finite mobility of ions. Four scenarios are qualitatively illustrated in Figure 2.7. For negatively charged surface, the K^+ cation is known to be the main charge carrier due to coulombic interaction, thus the following discussion will be focused on cation transport. The contribution of the anions follows the same mechanism but has opposite direction. Separated by the cross-point potential (e.g. 0.090 V in 10 mM), the top two panels illustrate the high conductivity state while the bottom two panels represent the low conductivity state. At rest with no bias potential applied, the diffuse layer extends parallel from the surface. The black dash line illustrates the double layer structure

(i.e. the Debye length plane). Because the pore interior has a taper, the direction of the double layer is separated from the applied potential by half cone angle θ. When a positive bias potential relative to the pore interior is applied (high conductivity state), the ion distribution is polarized toward the interior of the pore, represented as red dash line. At low conductivity states the displacement is reversed toward the pore exterior (shown as blue dash line). Since those dashed lines illustrate the impacts of surface potential, the trend is actually opposite to those simulated overall conductivity profile inside nanopore. For forward scan from lower to higher conductivity states, the direction of effective transmembrane potential is against the applied potential. Conversely, the two potential profiles have the same direction in the backward scan. Therefore, the forward current is lower than the backward current.

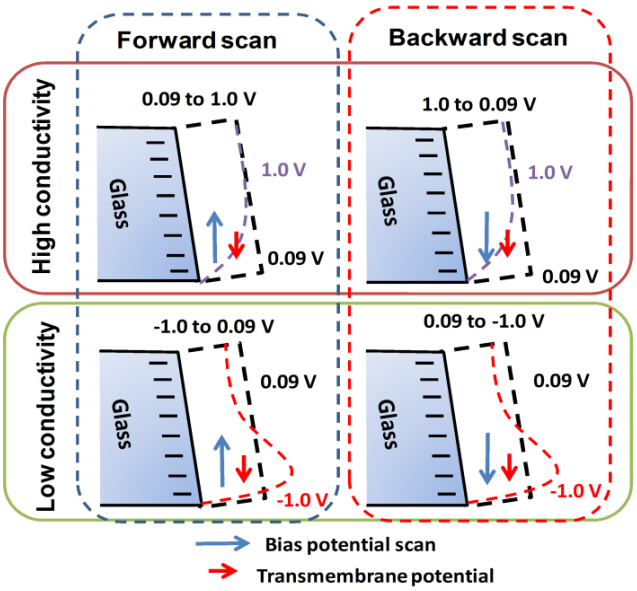

Figure 2.7 Visual representation of the mechanism governing IT memory effects in nanopores. Blue arrow represents the scan direction of applied potential: the forward scan is defined as from lower to higher conductivity states while backward scan the reverse. Red arrow illustrates the direction of electric field resulted from negative charges on glass substrate. The dash lines illustrate the undisturbed and polarized double layer structure respectively. Note those lines do not reflect conductivity profiles reported in simulation studies. Not drawn to scale. The figure was reprinted with permission from ref 64. Copyright 2012, American Chemical Society.

The time scale of the polarization of ion distribution inside nanopore can be estimated directly from the ion mobility and the applied potential. The ion mobility of K^+ and Cl^- at ca. 8×10^{-4} $cm^2s^{-1}V^{-1}$ is used. At 0.5 V applied potential, assuming the effective pore depth at 1×10^{-4} cm, the average velocity would be 4 cm/s. The time for ions in the middle of the nanopore to migrate out of the current-limiting region with negligible surface interaction would be 1.25 ms. This corresponds to the fast process shown in impedance measurements (800 Hz). At 1 mV potential intervals in *i-V* measurements (e.g. from 0.5 to 0.501 V or from 0.5 to 0.499 V), the scan rate to observe this memory effects due to non-instantaneous ion re-distribution, or a difference in forward and backward current, would be 1 mV/1.25 ms, or 0.8 V/s. This corresponds to the polarization of ion distribution at the whole current-limiting nanopore region, thus the maximum memcapacitive effects. The surface electric field would tend to maintain the ion distribution inside the nanopore and induce a range of scan rate (i.e. 20X w.r.t 0.8 V/s) for analyzing this interaction and the resulting memory effects. If the scan rate is too slow (i.e. 0.020 V/s or less), the phase shift would be negligible. The resistance/memresistance behavior will dominate the measurements. At very high scan rate (i.e. 8 V/s or higher), the capacitive behaviors corresponding to the charging and discharging of external interfaces of glass substrate will dominate the measurements. This has been reported previously by Zhang and coworker.[11] Overall, the rationale agrees well with the measured *i-V* results.

2.4 Conclusions

In summary, memory effects have been discovered in the ion transport confined by nanoscale geometry and interface. In time and frequency domain electrochemical measure-

ments, a non-zero cross-point potential is found to separate normal RC behavior from negative capacitive or inductive behavior in low frequency range (sub 1 kHz). The cross-point potential is quantitatively correlated to solution ionic strength, through which the effective surface potential inside single nanopores is noninvasively determined. The physical origin of the memory effects is attributed to the relative kinetics between the stimulus (applied potential) and the responding ion transport, which induces the polarization of diffuse layer within the current-limiting region in nanopores affected by ion mobility and surface potential. The analysis provides fundamental insights of the structure and dynamics of electrical double layer at nanometer scale.

3 DYNAMIC ION TRANSPORT FEATURES THROUGH SINGLE CONICAL NANOPORES: PHYSICAL ORIGINS

(This chapter has been published as "Wang, D. C.; Liu, J.; Kvetny, M.; Li, Y.; Brown, W.; Wang, G. L., Physical Origin of Dynamic Ion Transport Features through Single Conical Nanopores at Different Bias Frequencies. *Chem. Sci.* **2014,** *5*, 1827-1832." Reproduced by permission of The Royal Society of Chemistry.)

Ionic transport through nanometer scale channels or interfaces is the physical origin of the detection signals in stochastic single molecular sensing, DNA sequencing and nanostructured electrodes. Dynamic transport regulated by systematically varied bias frequencies has not been explored. In this chapter, ion transport through single conical nanopore platform is studied by applying an alternating electrical field at a wide range of scan rates. Rich frequency-dependent features of the measured transport current are discovered. The full transition in characteristic transport features from low to high scan rates or bias frequencies is demonstrated experimen-

tally. Key dynamic features include: multiple hysteresis loops separated by one or two non-zero cross points in *i-V* curves, shift in cross point potentials at different scan rates, and growth and diminishment in the hysteresis loops with normal and negative phase shifts. Combined theoretical and experimental studies reveal different processes contributing and dominating the total current responses at different time scale. The respective contributions of each type of transport process to the overall measured current signals are quantitatively separated based on the fundamental insights gained. Albeit those exciting experimental observations are successful simulated using an optimized model by solving PNP equations, the experimental studies at this nanoscale dimension suggest substantial deviations from continuum regime. The inputs from molecular theory are needed to further validate the proposed physical mechanism.

3.1 Introduction

Transport behaviors through solid-state nanopores have attracted extensive attention recently due to the promising applications and implications in sensing, DNA sequencing, separation and high density energy storage and conversion.[1, 3, 85, 91] Albeit steady-state transport has been extensively studied, with ion current rectification (ICR) being a well-known feature,[10, 20, 23] transient or non-steady-state transport behaviors have not been systematically explored. The lack of fundamental understanding imposes many scientific and technical challenges, because the dynamic transport behavior, rather than the static view, are the physical processes that are directly relevant to concentration enrichment or depletion in separation,[92-94] charging and discharging at nanostructured electrodes, and current oscillation induced by transient transport in sensing and nanoprecipitation.[95-96]

At nanoscale confinement, the interactions between the fixed charges on the substrate and the mobile ions in solution are known to be significant, thus contribute to and even dominate the transport behaviors. An applied potential will establish an electrical field that superimposes with the surface electrical field at the transport-limiting nanopore region. Consequently, static ion distribution (concentration profile) and steady-state ion transport will be regulated by the overall electrical field and are known to deviate from bulk behaviors.

Novel transport features emerge if a transient or alternating potential waveform is employed. AC impedance studies of ion transport through single conical nanopores reveal multiple transport processes with different time constants.[97] A surprising negative phase shift in the current responses induces apparent inductive loop at the high conductivity side of the rectified *i-V* curve. The experimental observation is in agreement with the negative capacitance proposed in a molecular dynamic simulation study.[84] Under a triangular potential waveform, the rectification factor (current ratio at the same potential amplitude with opposite polarities) was found to decrease at high scan rates of potential sweeping.[82-83] Memristive behaviors, reflected by pinched hysteresis *i-V* loops, were discovered from dynamic ion transport through single conical nanopores if the scan rate of the cyclic sweeping potential increases and deviates from those steady-state conditions.[98] Since most of the nanopore-based applications are realized by analyzing the resulting current signal, understanding and quantification of dynamic ion transport processes would be of great significance.

Several dynamic processes with different time constants could potentially contribute to the ion transport through channel-type nanodevices. Shown in Figure 3.1, ion current signals from a conical nanopore with radius at hundreds nanometer or smaller could arise from: surface con-

ductance (I_s) defined by the surface electrical field originated from the fixed surface charges on glass substrate inside nanopore; bulk current (I_b) defined by volumetric conductance at the transport-limiting nanopore region; and the capacitive charging and discharging (I_c) of glass membrane that involves large exterior membrane surfaces.

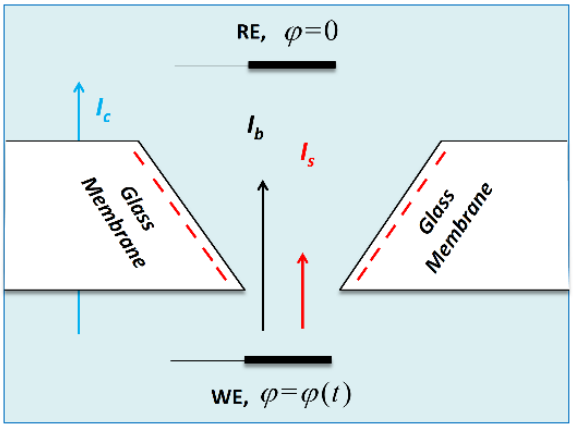

Figure 3.1 Physical origins of the transport current signals measured across a single conical nanopore. Two electrodes are placed on either side of the glass membrane in an electrolyte solution, on which a bias potential is swept at controlled frequencies. Note the direction of surface electrical field is normal to the glass surface inside nanopore due to the negative surface charges, and thus is separated from the direction of applied field or ion flux by half cone angle.

In this chapter, continuous transition of experimental *i-V* features at a wide range of potential scan rates is systematically studied on single conical nanopore platform. Those dynamic ionic transport behaviors are subsequently modeled and quantitatively fitted in numeric simulation by solving time-dependent Poisson and Nernst-Planck (PNP) equations. The proposed model and the physical origin of the dynamic ion transport features are validated by the excellent correlations between the experiments and simulation.

3.2 Experimental section

3.2.1 Experimental details.

The fabrication and characterization of the single conical glass nanopores follow previous reports[38, 77, 99]. Briefly, a 25 μm radius Pt wire was electrochemically etched to form a sharpened conical nanotip. This tip is then sealed into a thermally-melted end of a glass capillary. CORNING 8161 glass capillaries (OD 1.50 mm, ID 1.10 mm, and relative permittivity 8.3, Warner Instruments) were used. After the nanotip is exposed by polishing the excess glass, full removal of the Pt wire inside the capillary will result in a single conical nanopore replicating the Pt nanotip geometry embedded in large glass membrane substrate. The radii of the nanopores used in this report ranges from ca. 20-200 nm characterized by conductivity. The electrochemical measurements were conducted with a Gamry Reference 600 potentiostat. Two Ag/AgCl wires were used to control the bias and to collect the current signal. In the potential sweeping measurements, the potential step is 1 mV. The scan rate in *i-V* measurements can be converted to the frequency of the cyclic sweeping triangular waveform by the reciprocal of potential window divided by scan rate.

3.2.2 Computational methods.

Poisson and Nernst-Planck (PNP) equations were used based on the literature to describe and predict the ion transport behaviors through nanopores and nanochannels:

$$J_i = -D_i \nabla c_i - \frac{z_i F}{RT} D_i \nabla c_i \nabla \phi \qquad \text{(Eq 3.1)}$$

$$\nabla^2 (\varepsilon_0 \varepsilon_r \phi) = -F \sum_i z_i c_i \qquad \text{(Eq 3.2)}$$

where D_i is the diffusion coefficient, C_i is the concentration, z_i is the valence of the ionic species i, F is the Faraday constant, R is the gas constant, T is the temperature, ϕ is the electrostatic potential, ε_0 and ε_r are the relative permittivity of the vacuum and medium respectively. Flow is ignored because its contribution is negligible compared to the diffusion and migration components under the low surface charge density (SCD) and the low bias applied in this study.

The two 2D axis-symmetrical models used in the simulation are shown in Figure 3.2. Model 1 is a simplified model that only includes the structure near the transport-liming nanopore region. Note this is the model employed in previous studies that proven to be effective in steady-state simulations. In model 2, by adding a large glass membrane domain (FEGH, ε_r= 8.3), a 2D conical nanopore was connected with two large reservoirs (30 × 2 μm), in which EF and GH represent the large exterior glass membrane/solution interfaces. The boundary conditions and other details follow previous papers.[100-101] A time-dependent triangular potential waveform ($d\phi/dt = \pm v$) with different scan rate v is applied. The PNP equations are solved with finite elements analysis using COMSOL Multiphysics.

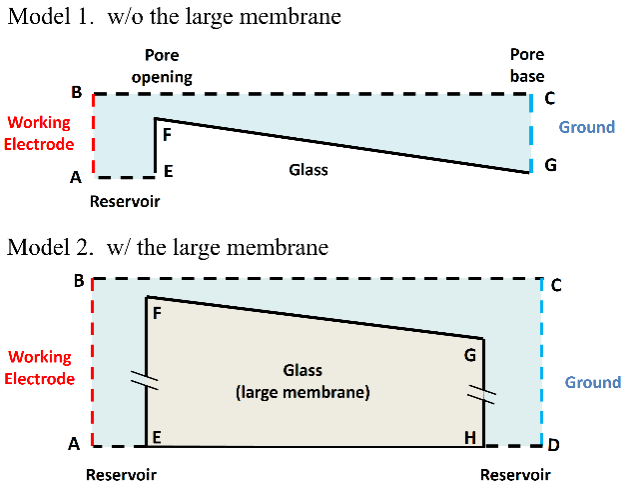

Figure 3.2 The two models used in the simulation. Half of the nanopore is constructed based on the axis symmetry (BC). In Model 2, FE and GH represent the extra exterior surface introduced (30 µm).

3.3 Results and discussions

3.3.1 Experimental i-V features at different frequencies

The *i-V* curves of a 200 nm radius nanopore in 1 mM KCl solution measured under a wide range of potential scan rates are shown in Figure 3.3. The results from this large pore are representative for different nanopores, and better illustrate the full transition of the *i-V* features at different scan rates (frequencies of the bias) than the smaller ones. It is obvious that the current responses involve different dynamic processes at different scan rates.

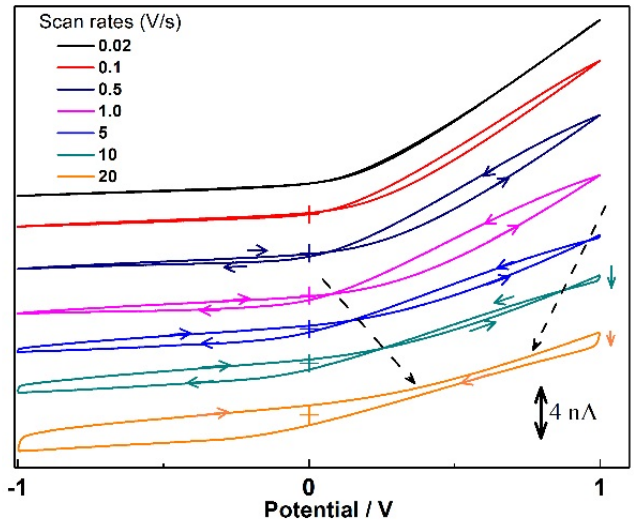

Figure 3.3 Experimental *i-V* features from a 200 nm radius nanopore in 1 mM KCl at different scan rates. The cross at each curve indicates its axis origin (0 V, 0 A) to better present non-zero cross point and its transition. The arrows indicate the potential sweeping directions and the dash arrows show the changing of the cross point at relative high scan rates.

At low scan rates (i.e. 0.02 V/s), the rectification of steady-state current is observed: the conductivity is higher at positive than negative polarities at the same bias magnitude. The well-studied ion current rectification (ICR) arises from the asymmetric nanogeometry and fixed negative surface charges on glass substrate. The current curves of the forward and backward potential scans, corresponding to potential sweeping away from and toward the origin respectively, almost overlap with negligible hysteresis effect.

At medium scan rates, i.e. from 0.1 to 1 V/s, pinched hysteresis loops emerge and superimpose with the rectified current responses. Two loops are discernible at high and low conductivity states separated by a non-zero cross point at positive bias (outside vs. inside). The hysteresis effect is due to the slower redistribution of ions with respect to the variation of the applied potential that is being swept at the respective scan rates. The ion redistribution corresponds to the polarization of the electrical double layer (EDL) established by the surface electrical field

within the transport limiting nanopore region. In comparison with the steady-state current responses under constant bias or bias at low scan rate, when the applied potential is swept faster, the ions inside the nanopore do not have sufficient time to redistribute accordingly. Because the ion redistribution affects the surface electrical field in turn, the effective surface electrical field will display phase shift with respect to the sweeping applied electrical field and changes in its magnitude. It is noteworthy to reiterate that the electrokinetic transport of ions is determined by the overlapping effects of both externally applied and intrinsic surface electrical fields. The direction of the surface field is constant, determined by the negative surface charges. Consequently, the component of the surface electrical field along the transport direction (by the half cone angle of the conical nanopore) has the same and opposite directions with the applied field at positive and negative bias polarities, thereby displaying negative and positive phase shifts accordingly. In this scan rate range, the cross point (V_M) remains constant, reflecting the balance between the applied and surface electrical fields. The size of the hysteresis loops, current gap between the forward and backward scans at the same bias, is an indication of the surface current (I_s), which increases with the scan rates.

At higher scan rates, i.e. 5 and 10 V/s, the cross point shifts toward more positive bias. Meanwhile, a new cross point appears near the upper potential limit and negative shifts. The loop on the low conductivity side grows large and the high conductivity loop becomes smaller. With sufficiently high scan rates, the two cross points merge and then disappear (i.e. 20 V/s). The forward and backward current curves separate, displaying typical but distorted capacitive charging/discharging responses of electrode-electrolyte interfaces. The trend suggests a classic capacitive charging/discharging current (I_c) that is superimposed over the nanopore-transport

current over the full potential range. As the capacitive processes begin to dominate the overall current response, the steady-state ICR effect and surface current contributions become less distinct. Interestingly, the non-parallel distortion between the forward and backward scans in *i-V* measurements at high scan rates resembles some charging and discharging behaviors frequently observed from ensemble electrodes and membranes in energy devices. Therefore, the results from single nanopores might have significant implications that the efficiency and efficacy in high density energy devices can be further improved by minimizing the cancellation effects from the amorphous ensemble nanoporous structures at electrode-electrolyte interfaces.

3.3.2 Time-dependent simulation

Apparently, the experimentally measured current responses involve multiple processes with different time constants. Two simulation models with and without the exterior glass membrane surfaces are employed in the simulation to differentiate and quantify these processes separately. The exterior substrate-solution interfaces are generally ignored in the simulation literature studying ion transport through channel-type nanodevices. This is a valid approach for the steady-state and low frequency transport studies in which the current signal primarily originates from the through-transport. However, for transient measurements in wide frequency range, especially at relatively high scan rates, the aforementioned approach appears to oversimplify the problem. A complete model incorporating both nanopore structure and substrate membrane with exterior surfaces is required to simulate and interpret the experimental results.

The simulated *i-V* curves at different scan rates using Model 1 and 2 are shown in Figure 3.4. The size of the conical nanopore is 100 nm with a half cone angle of 11 degree. The surface

charge density (SCD) is kept constant at -0.01 C/m^2. Those parameters are representative for the nanopore devices used in experiments. At low scan rates, Model 1 and 2 output same results. This is expected as the current is mainly from the steady-state transport current limited by the nanopore. At higher scan rates, the current responses from Model 1 and 2 are different. Without the exterior interfaces defined (Model 1), the non-zero cross point appears at a constant positive bias (20 mV) over a wide scan rate range tested, which fails to describe the experimental trend. By introducing the glass membrane with exterior interfaces in Model 2, the transition of the current responses at different scan rates reproduces the experimental trend successfully. A second cross point appears near the high potential limit first. The two cross points approach each other, merge and finally disappear at higher scan rates. The finding strongly supports the proposed mechanism that the transport current signals are superimposed with significant capacitive current at high scan rate, which arises from the charging and discharging processes across the glass membrane exterior interfaces.

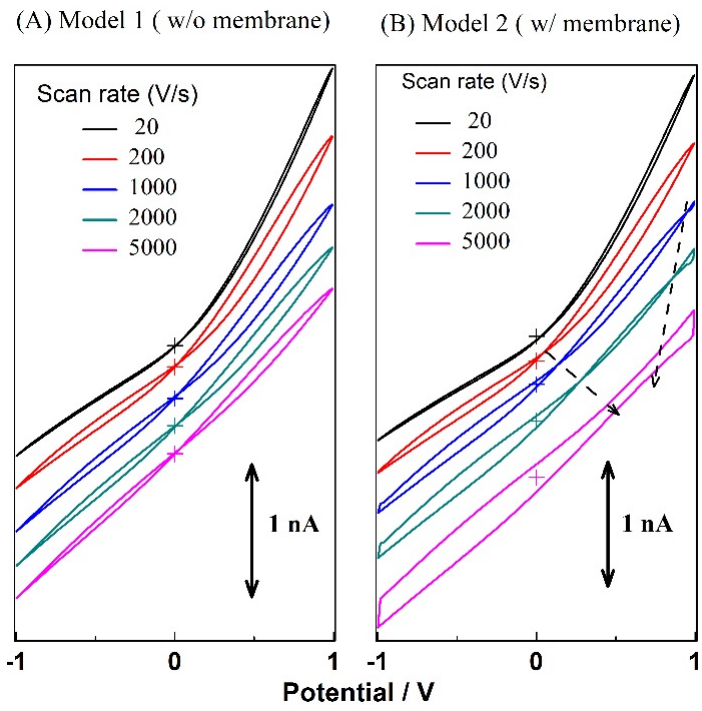

Figure 3.4 Simulated *i-V* responses from a 100 nm radius nanopore with Model 1 and 2 at different scan rates in 1 mM KCl. The cross at each curve indicates its axis origin (0 V, 0 A). The half cone angle is 11 deg, and the SCD are kept constant at –0.01 C/m^2. The spikes at the switching potentials (±1V) are attributed to the digital noises in simulation. The discrepancy in scan rates between experiments and simulation is discussed in the next section.

3.3.3 Delineation of transport and capacitive charging processes.

Next I deconvolute the two dynamic processes quantitatively. The current curves in Figure 3.5A were obtained by subtracting the simulated current in Model 2 by that in Model 1 at each scan rate, which corresponds to the elimination of transport current through the nanopore (I_b and I_s). If the proposed mechanism is valid, the residue current responses should display pure capacitive charging/discharging loops (I_c). At each scan rate, capacitive loop can be clearly seen. Shown in Figure 3.5B, the gaps between the forward and backward current curves display an excellent linear relationship with the scan rates *v* and become negligible at low scan rate. The computed capacitance of 0.021 pF matches with the geometric capacitance of glass membrane

defined ($C = \varepsilon_0 \varepsilon_r A/d$ = 0.021 pF, with radius 30 µm, separation distance 10 µm and relative permittivity 8.3).

This linear correlation is characteristic for capacitive behaviors and thus further affirms the proposed mechanism. The significance of this analysis is that the capacitive charging/discharging processes (I_c) can be quantified independently, through which the factors affecting each type of transport processes could be elucidated.

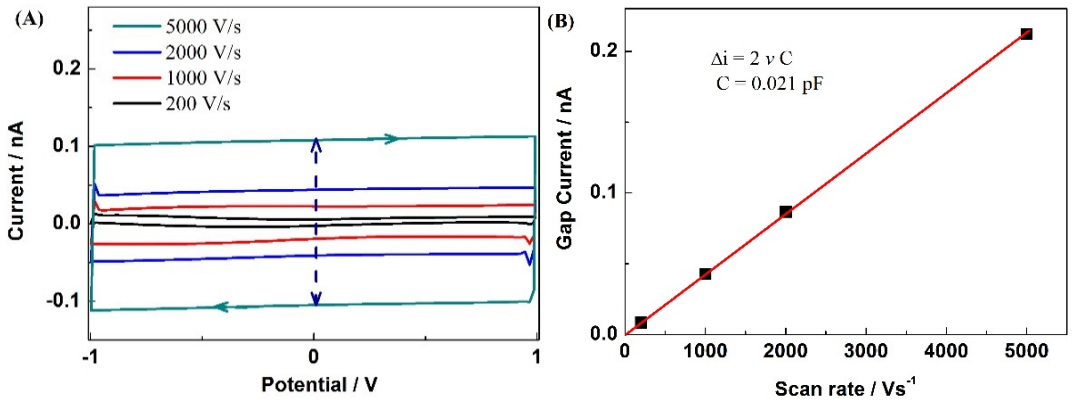

Figure 3.5 Analysis of the deconvoluted capacitive current. (A) The residue current by subtracting the simulated current using Model 1 from that of Model 2 at each scan rate. The spikes at the switching potentials (±1V) are due to the digital noises in simulation. (B) Gap current and scan rate correlation. The gap current was calculated from the differences between the forward and backward scans in panel A at 0 V.

In retrospect, the experimental observations of cross point shifts and hysteresis loop variation at relatively high scan rates shown in Figure 3.2 can be further analyzed. At low scan rates when the capacitive charging/discharging contributions are negligible, the measured cross point potential (58 mV) in Figure 3.2 would reflect the balance between the surface and applied electrical field. This balance should be independent of the scan rate and does not shift at the high scan rate based on the simulation results using Model 1. Therefore, the current difference

between the forward and backward current at this potential is from the capacitive charging/discharging process at the exterior membrane, and should be proportional to the scan rate. The current differences at 58 mV bias are plotted against scan rates in Figure 3.6. A linear relationship is clearly obtained. Because the gap current corresponds to the capacitive charging/discharging that can be expressed as 2*v*C, where *v* is the potential sweeping scan rate, the effective membrane capacitance *c* of this specific nanopore under the measurement solution conditions is calculated from the fitted slope at the value of 37 pF. Following similar analysis of Figure. 3.5B, the effective geometry of the glass membrane used in experiments is characterized as $A/d = C/(\varepsilon_0\varepsilon_r)$ = 37 pF/(8.85E-12 F/m *8.3) = 0.5 m. Accordingly, subtraction of the charging/discharging current at each scan rate reveals pure transport current through the nanopore regulated by the applied and surface electrical fields. The constant cross point at all different scan rates shown in panel B agree well with the trend predicted in Figure 3.4 A (model 1) and further affirm our analysis.

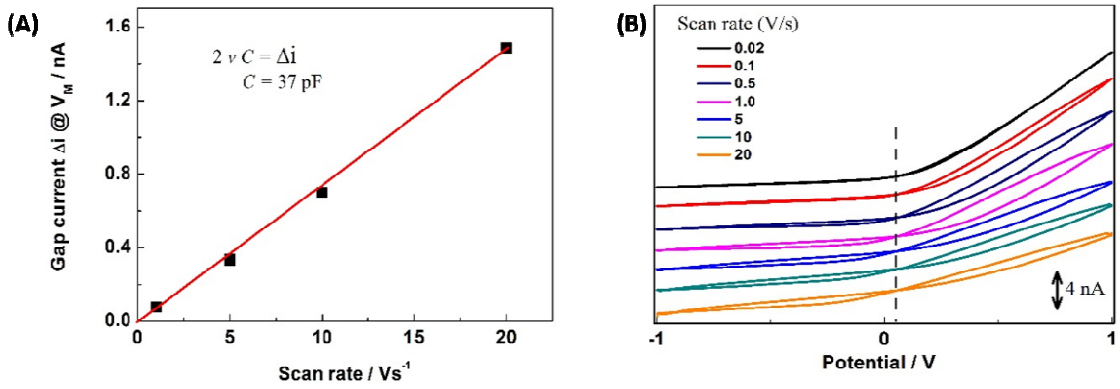

Figure 3.6 (A) The current difference at the cross point potential from the nanopore in Figure 3.2 at various scan rates. Clearly, perfect proportional relationship between the gap current and scan rate indicate an ideal capacitive behavior and the membrane capacitance for this nanopore is 37 pF. The current responses after subtraction are shown in the panel B, a constant cross point is displayed at all different scan rates.

However, to observe comparable *i-V* features, the scan rates in the simulation need to be defined much higher than those in the experiments. Several factors could contribute to this disconnection that requires further investigation. The immediate possibility is that the membrane area defined in simulation is much smaller than a real device in experiments as estimated from capacitive charging analysis. For simple parallel plate capacitor (or capacitance of planar electrode surface), a larger surface area will have larger capacitance, which would result in larger gap current at a given scan rate. Clearly larger substrate membrane will generate larger capacitive current superimposed on the transport current at the same scan rate. Therefore the two-order scan rate difference between the experiments and simulation at high scan rates, 20 V/s in the experiments and 5000 V/s in the simulation for example, could probably result from the membrane radius difference. The membrane radius and channel length effect on the resulting currents are shown in Figure 3.7. At the same scan rate of 1000 V/s, the current simulated from the 100 μm-radius membrane are dominated by the capacitive membrane charging and discharging processes, while the 2 μm-radius membrane only display pinched hysteresis currents. The channel length effect on the simulated currents are included in the panel B, basically the transport currents are similar at different channel length. It is as expected as the effective length, or most resistive region for the conical nanopores is generally within the first 1 μm from the pore orifice.

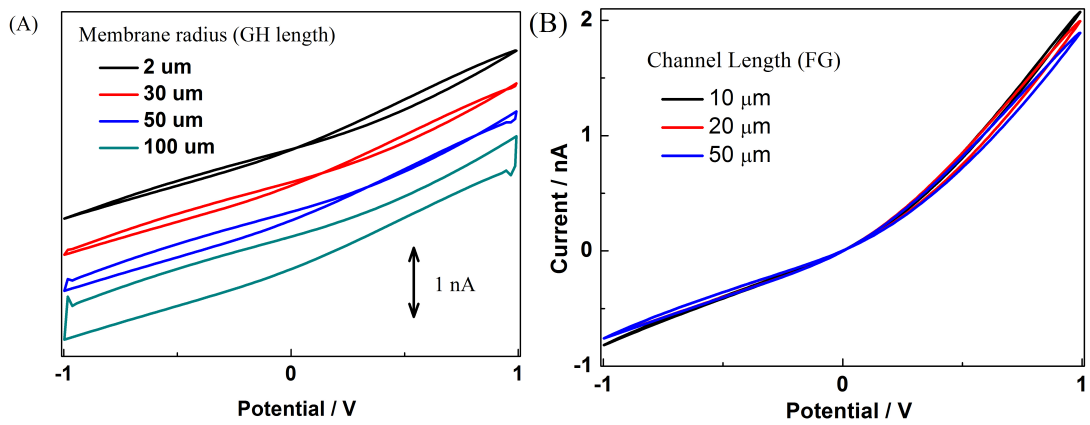

Figure 3.7 Simulated current using model 2 at (A) different membrane radius (GH) and (B) different channel length (FG). A constant SCD of -0.01 C/m^2 is applied on FG. The KCl concentration is 1 mM with the scan rate at 1000 V/s in the simulation.

For Model 2 in the simulation, the membrane radius is 30 μm while in the experiments, the glass membrane has a radius of 200 μm. Unfortunately a larger exterior substrate-solution interface definition will significantly increase the computation load and cause converging issues. Because of the pure capacitive responses based on the almost perfect linear correlation shown in Figure 3.5B, it can be easily deconvoluted from the total current and allow the study of ion transport dynamics through the nanopore. Therefore, I opt to use this higher scan rate in simulation instead of a larger dimension in the following studies. Other factors such as ion size, the ion-ion interactions and ion solvent interactions could also play important roles. To account for those factors, molecular theory is required that is beyond the scope of this report.[102-103]

3.3.4 Fitting of experiments by simulation.

In general, the first step in simulation is the construction of the nanopore geometry based on experiments. A uniform surface charge density (SCD) is then defined on the boundaries limiting the ion transport processes. However, the SCD values have to be adjusted based on individual

measurements or nanodevice even though the same type of substrate materials is used. To overcome the fact that the simulated current at low conductivity side is consistently overestimated compared to experiments, a gradient SCD is defined inside the nanopore surface following reported procedure:[104]

$$\sigma(z)=\sigma_0\, e^{-z/L}+\sigma_b \qquad \text{(Eq 3.3)}$$

At the pore orifice (z=0, point F), the SCD has the maximum value $\sigma_0+\sigma_b$, then it decay to the bulk value σ_b (-0.001 C/m^2 in this work) along z direction, and decay constant *L* describes distribution length of the gradient SCD, and is generally in the range of 0.5 to 1 µm. It is also worth pointing out that at this low scan rate, since the simulated current is at steady state and the capacitive current is negligible, Model 1 and 2 output the same results.

The experimental *i-V* curve from a 60 nm nanopore in 1 mM KCl solution is firstly fitted in simulation shown in Figure 3.8A. At low scan rate (overlapping forward and backward scans), by adjusting the SCD maxima $\sigma_0+\sigma_b$ and distribution length *L*, a unique SCD maximum (-0.03 C/m^2) will generate perfect fitting of *i-V* curve on the high conductivity state side. With that SCD maximum fixed in the next series of simulation, a unique distribution length *L* (1.6 µm) will allow the fitting of *i-V* curve on the low conductivity side. The two parameters are then fixed in the simulations in which the potential scan rates are systematically varied. To correlate with the experiments, Model 2 including the exterior glass-solution interface was used here. Shown in panel B, it is clear that the simulation (red dots) and experiment (black lines) are in excellent agreement, notably the cross point and hysteresis loops. The only disconnection is the scan rate, with the

experimental *i–V* responses measured at the 0.8 V/s while the simulated curve obtained at 30 V/s.

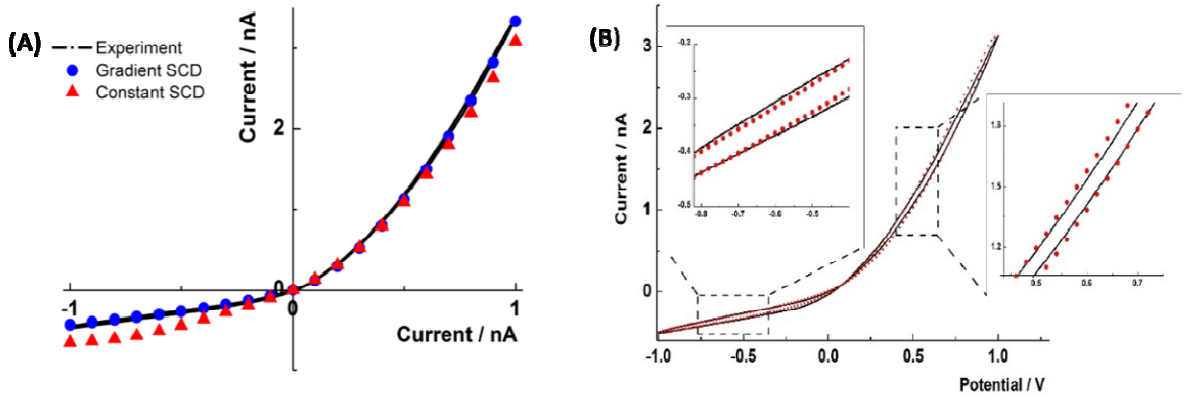

Figure 3.8 (A) The comparison of simulated currents at the constant and gradient SCD. The gradient SCD result in a better fitting especially at the low conductivity states, the fitting parameters are $\sigma_0 + \sigma_b$ at -0.03 C/m2 and L at 1.6 µm obtained from panel A. (B) With the obtained SCD value, the comparison of the i-V responses from simulation (red dots, scan rate 30 V/s) and experiment (black line, scan rate 0.8 V/s). Data were collected using a 60 nm radius nanopore in 1 mM KCl solution. The enlarge views at positive and negative potential windows are shown as insets.

3.4 Conclusions

Dynamic ionic transport processes are regulated experimentally by sweeping an externally applied potential at wide frequency range using conical nanopore platform. Three types of transport processes are found to contribute to the measured *i-V* features, including the geometry defined volumetric conductance I_b, surface electrical field induced hysteresis effect I_s, and the capacitive charging and discharging processes of the glass membrane with exterior substrate-solution interfaces I_c. Through a combined experiment and simulation approach, these processes are shown to have different time constants and thus can be differentiated by proper selection of measurement frequencies. The fundamental understanding of the frequency-dependent transport current responses is believed generalizable in other channel-type

nanodevices and has significant implications in related applications such as sensing and energy conversion. The elucidated physical origins and the proposed mechanism are further validated by the excellent fitting of transport current features through numeric simulation at all bias and frequency ranges.

4 SIMULATION AND PREDICTION OF THE NON-ZERO CROSS POINT FROM HYSTERESIS CURRENTS IN SINGLE CONICAL NANOPORES

(The results in chapter is being prepared for publication: "Correlating Non-zero Crossing in Pinched Hysteresis Current-potential Curves from Single Conical Nanopores with Nanogeometry and Surface Factors")

The intriguing non-zero cross point, resolved from the pinched hysteresis current-potential curves from conical nanopores, is quantitatively correlated to the surface and geometry properties of the nanopores through simulation studies in this chapter. The analytical description of the cross point is further developed based on the classical double layer theory. The potential at the cross point is shown to represent the averaged surface potential in the nanopore and the cross point current includes both the surface and volume conductance. Some parameters such as pore radius, half cone angle, and surface charge descriptions are systematically varied in simulation that would be challenging experimentally. The elucidated trend is supported by experiments and offer predictive guidance for further experimental studies. The results also offer more quantitative and systematic insights in physical origins of the ionic current rectification (ICR) and concertation polarization (CP) inside conical nanopores. The cross point also serves as a simple but important parameter to evaluate the surface potential and conductance of broadly defined nanopore-type devices.

4.1 Introduction

Ionic current rectification (ICR), observed in various biological and solid state nanopores, is important for both fundamental understanding of nanoscale mass transport and broad applications including molecular sensing, nanofluidics, and fluidic circuits.[3, 6, 105] The ICR is believed to result from the asymmetrical geometry and/or surface charge distribution in the nanopores. The ionic concentration profile near the pore orifice, particularly inside, can be depleted or enriched by the applied potentials, pressure and other factors.[19, 23] The ICR of the nanopores have been extensively investigated experimentally and theoretically. Many factors have been found to affect the ICR behaviors, such as surface charge density, concentration, geometry, potential, pressure, and concentration gradient.[20 22, 24, 26]

The ICR is also found to be a dynamic process, as the rectification factor decreases at higher scan rates of the sweeping potential.[82-83] We have reported the pinched hysteresis current loops from the conical nanopores when applying a cyclic sweeping potential waveform experimentally. The rectified current shows a hysteresis dependence on its previous conductivity states.[63-64] More interestingly, the pinched hysteresis current loops cross at a non-zero point, which is independent of the external potential waveforms, neither the amplitude nor scan rates under the experimental conditions. This unique cross point therefore reflects some intrinsic properties of the nanopore itself. The physical origin of the cross point needs to be better elucidated, especially its quantitative correlation to the surface and geometry properties factors that govern the ion transport processes. These results could offer new physical insights of the ICR behaviors in nanopores, which also allow further quantification of the rectified currents in nanopores.

The potential at the cross point is proposed to represent the averaged surface potential across a nanopores. As shown in Figure 4.1, in conical nanopores, the surface electric field will have a component (V_s) in the mass transport direction, analogous to the build-in potentials in the diodes. The surface potential superimposes with the external bias (V_{app}) and polarizes ion concentration profile. In the specific case when the V_{app} balance out V_s, the potential induced net polarization is zero. Therefore the cross point would be the boundary of the potential induced concentration enrichment and depletion inside nanopores. In other words, the cross point separates the high and low conductivity states of the nanopores. Also, at this specific point, the conductance would be at steady-state including the bulk and surface conductance, without any contribution from the polarization of ion concentration distribution. Because the cross point define the boundary of the ICR and concentration polarization in the nanopores, quantitative correlation to the surface and nanogeometry factor is therefore very important for the development of the fluidic circuits and the nanofluidics for sample concentrator, ion desalination, or energy harvesting.

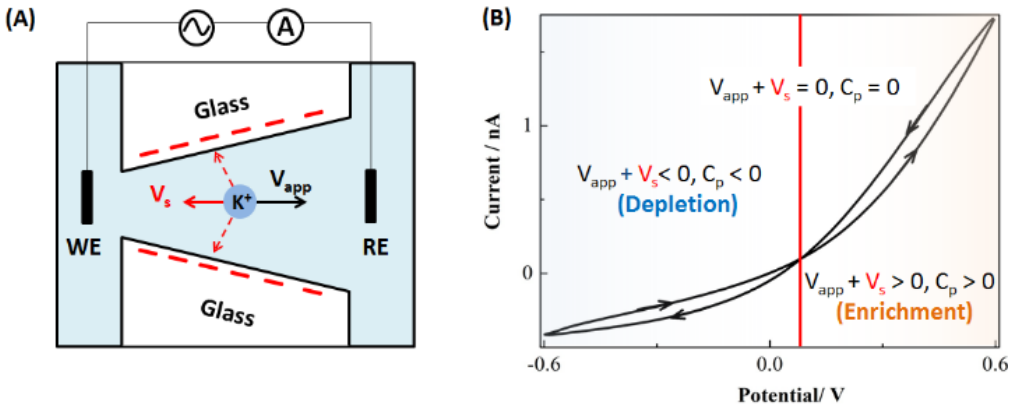

Figure 4.1 (A) In single conical nanopores, the surface field have a component in the mass transport direction. (B) The cross point in the pinched hysteresis current-potential curves (C_p = 0) separates the high and low conductivity states, or the concentration enrichment ($C_p > 0$) and depletion ($C_p < 0$).

The cross point potential and conductance, could also serve as descriptive parameters to evaluate the surface potential and conductance. The widely used rectification factor (RF), calculated from the current ratio at the same potential amplitudes but opposite polarity, can qualitatively describe the surface effects of the nanopores. However, it varies at the potentials amplitude that is generally selected arbitrarily. Further the RF is not suitable to describe the dynamic ICR features. The streaming potentials, measured form the pressure driven fluid through nanopores, are generally two orders of magnitude smaller than the expected value.[59] The cross point potential and conductance, which rule out the polarization contribution, will allow a more meaningful comparison of the surface effects between nanopores.

In this chapter, I will systematically investigate the cross points via numerical simulation of the dynamic mass transport in the conical nanopores under sweeping potentials. The cross points under different surface and geometry properties are simulated and analyzed. The analytical expressions of the surface potential and conductance are developed based on the classical double layer theory to explain the cross points.

Averaged surface potential. Based on the Gouy-Chapman theory, the potential distribution normal to a charged surface can be simplified as:

$$\phi_x = \phi_0 e^{-\kappa x} \qquad \text{(Eq 4.1)}$$

where Φ_0 is the potential at the surface. The decay constant κ (m^{-1}) is a characteristic parameter to indicate the thickness of the double layer, i.e. $1/\kappa$ is the Debye length. At normal conditions of room temperature and in dilute aqueous solutions

$$\kappa(nm^{-1}) = \sqrt{c}/0.3 \qquad \text{(Eq 4.2)}$$

The full analytical expression for the averaged surface potential (ϕ_{avg}) in a conical nanopores is complicated. Here I simplify the expression in two cases, either with fixed geometry or fixed surface properties. For a nanopore with fixed geometry, the variables would be the surface charge density (SCD) and solution concentration. It is worth emphasizing that the SCD inside the nanopore can be heterogeneous and vary at different location, applied potential, and in different electrolyte solutions. Assuming the surface potential at certain position (r_0, z_0) could represent the effective potential across the nanopore ϕ_x,, then at 293K in 1:1 electrolyte, the cross point potential V_M then can be expressed as:

$$V_M = \overline{\phi_x} = \phi_0 e^{-\kappa r_0} = \phi_0 e^{-\sqrt{c} r_0 / 0.3} \qquad \text{(Eq 4.3)}$$

In the case of the geometry effect on averaged surface potential, considering the half cone angle is small (ca. 11 degree) in our experimental studies, the averaged surface potential is approximated to that of cylinder geometry, therefore the analytical expression along radius direction:

$$V_M = \overline{\phi_x} = \frac{\int_0^r \phi_0 e^{-\kappa x} dx}{\int_0^r dx} = \frac{\phi_0}{\kappa r}(1 - e^{-\kappa r}) \qquad \text{(Eq 4.4)}$$

Cross point conductance. At the cross point, there is no net concentration polarization. The conductance here would be comprise the diffuse layer conductance, or the surface induced and the volumetric conductance:

$$G_M = I_M / V_M = G_s + G_{bulk} \qquad \text{(Eq 4.5)}$$

For a conical nanopore with a radius r, half cone angle θ, and bulk concentration C_0 (molar conductivity is Λ_m), the volumetric conductance can be estimated from the bulk resistance R_{bulk} based on the ohm's law:

$$R_{bulk} = \frac{1}{C_0 \Lambda_m r}\left(\frac{1}{\pi \tan\theta} + \frac{1}{4}\right) \qquad \text{(Eq 4.6)}$$

With a small half cone angle of 11 degree, the cone resistance term, 1/ (π tanθ), is much larger than the access resistance term (1/4). Ignoring the access resistance leaves the bulk conductance in approximation as:

$$G_{bulk} = 1/R_{bulk} = C_0 \Lambda_m r \pi \tan\theta \qquad \text{(Eq 4.7)}$$

By assuming the charge balance is maintained inside the nanopore, the surface enhanced ion concentration would be only determined by the surface charge density:

$$G_M = G_s + G_{bulk} = G_s(\sigma) + C_0 \Lambda_m r \pi \tan\theta \qquad \text{(Eq 4.8)}$$

4.2 Theoretical model

I have demonstrated that Poisson and Nernst-Planck (PNP) equations describe the pinched hysteresis and non-zero cross points of i-V curves from the conical nanopores very well with proper boundary conditions.[63] The electroosmotic flow is ignored here and in most nanopore transport studies because its contribution is negligible compared to the diffusion and migration components with small SCD and low bias potentials. The simulation models and boundary conditions established in our previous reports are employed.[63, 69] Because I am focusing on dynamic mass transport processes signaled by the non-zero cross point, the large glass membrane is not included to reduce the demands on the simulation. The glass membrane substrate gener-

ates a charging current experimentally that can be deconvoluted as reported previously. A time-dependent triangular potential waveform with different scan rate *v* is applied. The PNP equations are solved with finite element analysis using the commercial software COMSOL Multi-physics 4.3.

Gradient SCD. A gradient distributed surface charge density along the nanopore is found necessary to match the experimental i-V curves.[69] The SCD profile in the nanopore is defined as:

$$\sigma(z) = \sigma_0 \, e^{-z/L} + \sigma_b \quad \text{(Eq 4.9)}$$

At the nanopore base (large L), the SCD takes the bulk value σ_b. At the pore orifice (z=0), the applied potential establishes a high electric field that will alter the surface equilibrium. A maximum SCD is defined as $\sigma_0 + \sigma_b$. The SCD then exponentially decays along the z direction toward to the pore base. The decay constants *L* is normally within hundreds nanometers or few microns from the nanopore orifice indicating the distribution length of the high SCD.

4.3 Results and discussions

4.3.1 Pinched hysteresis loops with non-zero cross point.

The simulated current-potential (*i*–*V*) responses from a 46 nm-radius nanopore in 1 mM KCl at different scan rates are shown in Figure 4.2. The maximum SCD is − 0.07 C/m^2 with a distribution length of 1.5 μm. These parameters are selected that best fit the experimental reults from concial nanopore usd previously. Same to the experimental results, pinched hysteresis current loops with a non-zero constant cross point are observed at different scan rates. The enlarge view near the cross point is show as an inset, in which the red arrows indicate the potential

sweeping directions. The cross point potential V_M (86 mV) represents the averaged surface potential across the nanopore, and the conductance G_M (0.11 nA/ 86 mV) would include both the surface and volumetric conductance, G_s and G_{bulk}.

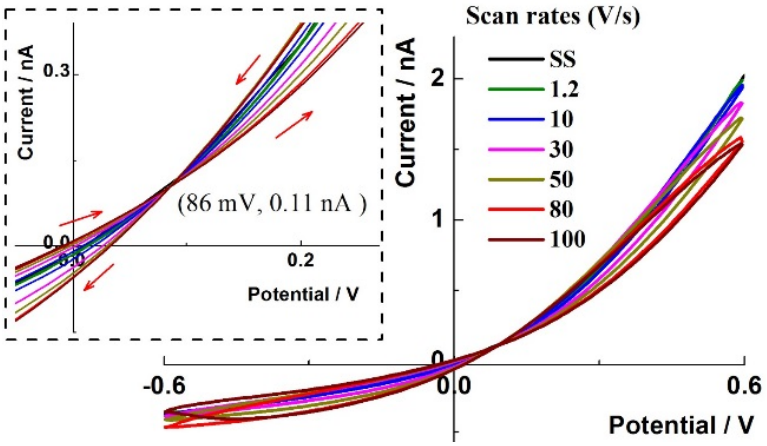

Figure 4.2 The simulated i-V responses from a 46 nm radius nanopore at different scan rates in 1 mM KCl. The enlarge view near the cross point is shown as an inset. The pinched hysteresis loops cross at a non-zero cross point, which is independent of the scan rates.

To correlate the transport features, specifically the potential and conductance at the cross point with experimental conditions, the following parameters were systematically varied: surface charge density of the nanopore, ionic strength, and nanopore geometry. Since the cross point is independent of the scan rates by excluding the glass membrane substrate, a fixed scan rate of 100 V/s was used that generates comparable responses with experiments at few volts per seconds. The discrepancy in scan rates between experiments and simulation remain unknown and postulated to the missing molecular-level interaction in our simulation that requires further theoretical studies.

4.3.2 Surface charges effect

The SCD effect on the cross point are shown in Figure 4.3. The cross point potential V_M increases as the SCD increases, which is expected becayse high SCD resulted in higher surface potential, and thus the averaged surface potential. Furthermore, in accordance with Eq 4.3, a well-defined linear relationship at a ratio of 0.47 was observed between the calculated surface potential and resolved cross point potential at various SCD. The surface potential under different SCD values are calculated based on the Grahame equation.

The K^+, Cl^-, and the total conductance at the cross point under different SCD values are included in the panel B. Since the conical nanopore is negatively charged, the Cl^- conductance at the cross point appears insignificant and independence of the surface charges, while the K^+ conductance increase as the SCD values increases and constitutes the majority of the total cross point conductance.

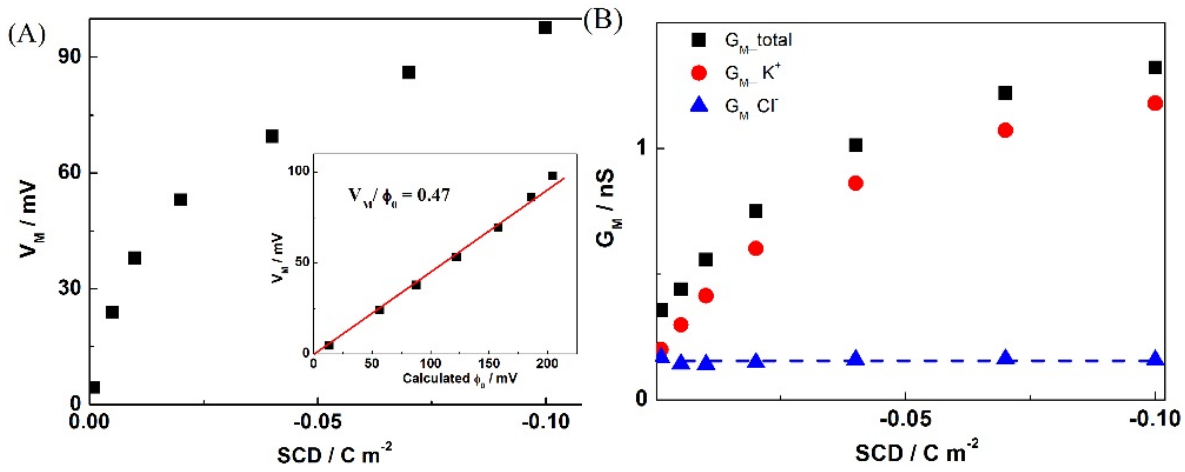

Figure 4.3 (A) The cross point potentials V_M and (B) the total and separate ion conductance at the cross point at various SCD values in 1 mM KCl solution. The cross point potential display a linear relationship with the surface potential. For the cross point conductance, the K^+ conductance increases as the SCD increases while Cl^- conductance is relatively constant to its volumetric value.

4.3.3 Ionic strength effect

For the ionic strength effect on the cross point, it is expected to see the decreasing of the cross point potential when increasing the ionic strength due to the electrostatic screening effect. The V_M and G_M in different ionic strengths are shown in Figure 4.4. The cross point potential V_M and the calculated surface potential ϕ_0 under different ionic strength are correlated by the Eq 4.3 very well. An excellent exponential relationship between the V_M and $C^{1/2}$ was observed. Interestingly, because the SCD remains unchanged and thus the surface potential ϕ_0 remains constant in those simulation, the V_M should display an exponential relationship with the square root concentration, which is in agreement with the equation Eq 2.1 as proposed in previous experimental studies.

The cross point conductance at different ionic strength is shown in Figure 4.4B. Clearly, the cross point conductance has a non-zero intercept value as shown in the inset. The intercept at infinitely low ionic strength results from the volumetric conductance. The same surface charge definition at various ionic strengths result in a constant offset between the cross point conductance and volumetric conductance, or the surface conductance. In the low conductivity regime, the surface conductance is basically independent of the bulk concentration, which agrees with the threshold conductance observed from cylinder nanochannels.[62] At higher concentration, as the surface conductance is too small, the cross point conductance is dominant by volumetric value. This trend directly support the proposed Eq 4.8 that the cross point conductance include both surface and volumetric conductance.

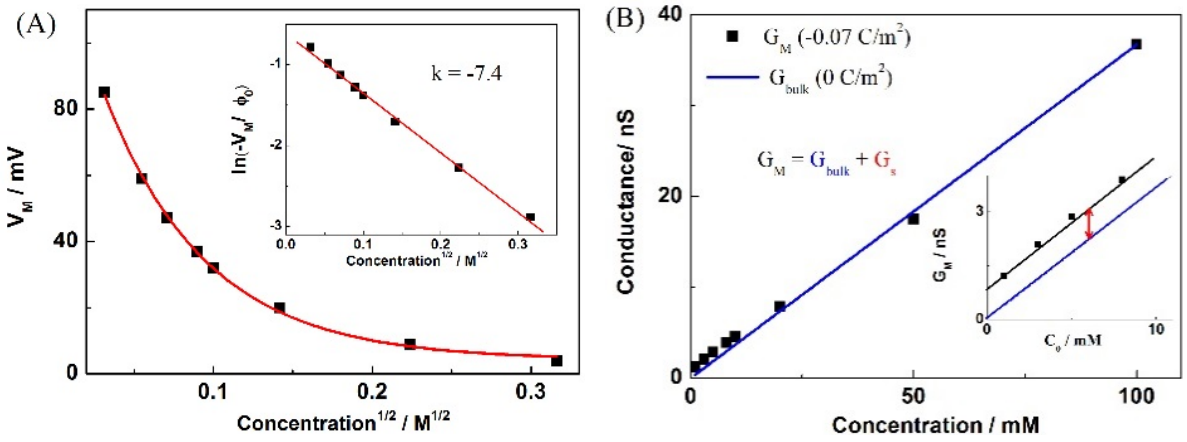

Figure 4.4 (A) The cross point potential V_M and (B) the cross point conductance G_M as a function of the ionic strength. As the concentration increases, the V_M decreases due to screening effect, while the G_M relatively remains at the low concentration region. Their trend can be quantitatively fitted by the proposed equations.

This cross point conductance is therefore an effective parameter to evaluate the respective contributions by surface and volume, just like the commonly used concentration-conductance plots for nanochannels with cylinder geometry: the cross point conductance at low concentration directly reveal the surface charges, since the G_{bulk} is negligible compared to the G_s; while the cross point conductance at high concentration would be mainly G_{bulk}. Noting that, expect for this specific cross point conductance, the conductance values under any other potential values will include the polarized ion contribution, which is both dynamic and nonlinear.

4.3.4 Radius effect

The radius effect on the cross point are included in Figure 4.5. Under the same interface properties (SCD and ionic strength), it is expected to see the decrease in the cross point potential upon the increase in the pore radius. At extreme conditions, for the pores with micrometer radii or larger, the cross point potential would be zero. It can be seen that the Eq 4.5 fitted their trend very well, with fitting parameters ϕ_0= 135 mV, 1/κ = 11 nm. In 10 mM KCl, Debye length

1/κ is about 3 nm at planar surface. The calculated ϕ_0 is 127 mV, which is very close to the fitted parameters.

For the conductance shown in panel B, Eq 4.8 also works very well to describe the linear relation between the cross point conductance and nanopore radius. The constant different between the G_M and G_{bulk} would be the surface conductance G_s. Again, the surface conductance is not affected by the nanopore radius as well. This is due to the unchanged surface charge definition in the simulation; the extra number or concentration of the counter ions remains unchanged, regardless of the pore size.

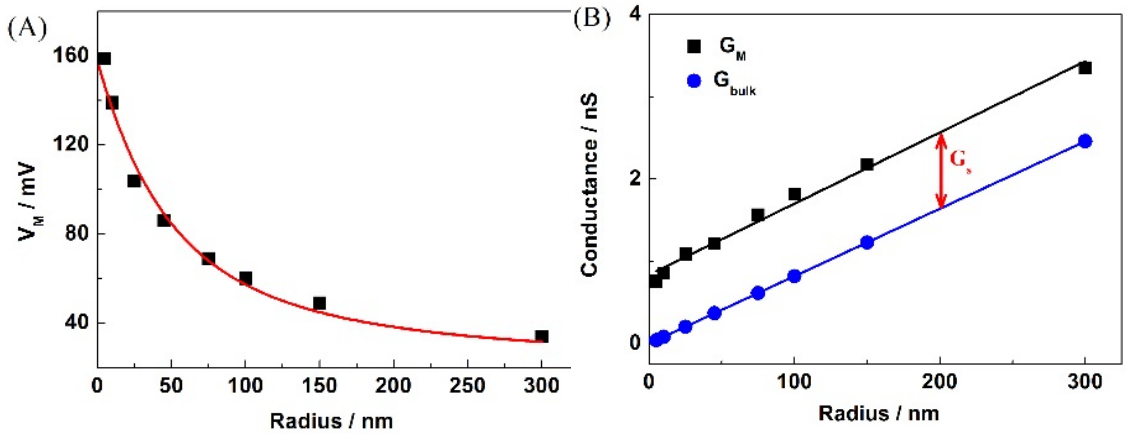

Figure 4.5 (A) The cross point potentials V_M as a function of the radius at a fixed half cone angle of 11 deg. (B) The G_M as a function of the radius.

4.3.5 Half cone angle effect.

Last but not least, within a small variation corresponding to our experimental results, the half cone angle and the nanopore depth (membrane thickness) should have less impact on the cross point potential at a given radius. Larger variation of the half cone angle should change the simulated results significantly. Shown in Figure 4.6, one can clearly see that the cross point potential

is a weak function of sharp half cone angles. However, the cross point conductance display a linear relationship with the tan θ. The increase of the surface conductance when θ increases suggest the surface induced concentration would also be a component of the diffuse layer in the mass transport direction.

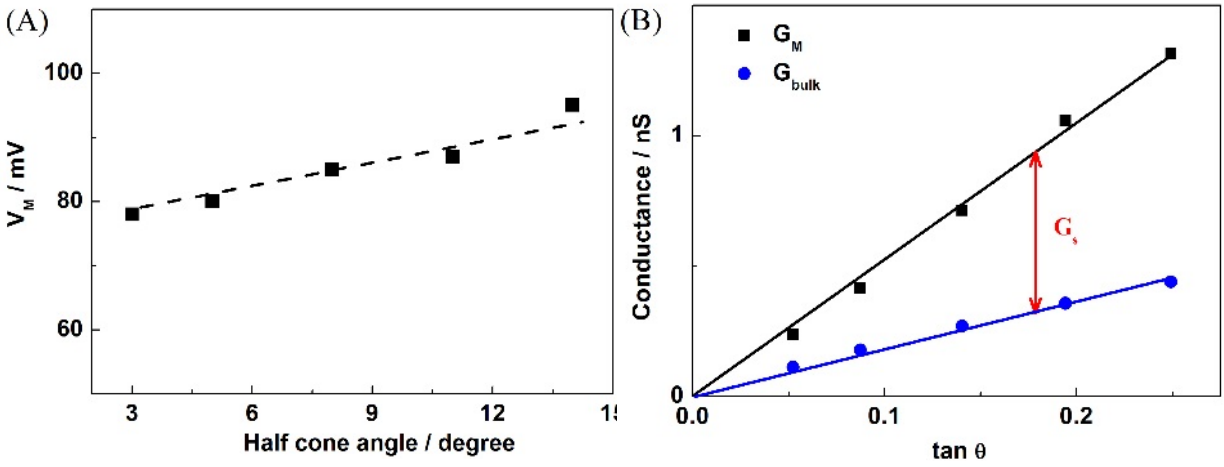

Figure 4.6 (A) The cross point potentials V_M as a function of the half cone angle. (B) The G_M dependence on the half cone angle with a radius of 46 nm.

4.4 Conclusions

In conclusion, the unique cross points in the pinched hysteresis current loops from ion transport through single conical nanopores are investigated and analyzed. I have confirmed that the cross point potential represent the averaged surface potential, and the cross point conductance would be the diffuse layer conductance without any polarization, as their trend can be quantitatively described by the models developed from classical double layer theory. By keeping other parameters constant while varying a single factor systematically, definitive and quantitative correlations are established regarding the dynamic ion transport characteristics inaccessible for experimental studies.

5 QUANTIFICAITON OF THE POLARIZATION CHARGES IN CONICAL NANOPORE

(The results in this chapter are in preparation for publication: “Dynamic polarization of ion concentration in single conical nanopores”)

Novel transport phenomena through individual structure-defined nanochannels, such as rectification, oscillation, and hysteresis currents, are important to offer insights inaccessible from ensemble systems for new and better applications including molecular concentrator, seawater desalination and energy harvesting. In this chapter, dynamic ion concentration polarization (ICP) process inside a charged conical nanopore is quantified. The analysis in charges or current complement our recent reports on the electric potential analysis of the memristive ion transport and resulting pinched hysteresis current-potential loops in conical nanopores/nanopipettes. Taken together, a comprehensive view of the charges distribution and dynamics at nanoscale interfaces is offered. Specifically, in cyclic voltammetry type measurements for a conical nanopore, the ion transport current responses are stimulated by applied triangular potential swept at a range of scan rates or frequencies. The area enclosed in each of the pinched hysteresis current loops are correlated with the magnitude of polarization of ion distributions, while the direction tells ion enrichment or depletion at the transport-limiting region. A model is proposed that successfully describe this dynamic process at different ionic strength and solution pH.

5.1 Introduction

The electrical double layer (EDL) structure at solid-solution interfaces is key concept in energy conversion and storage devices[92, 106] such as supercapacitors, electrochemistry, membrane transport, analytical separations and sensing[107-108]. Classic EDL structure is described by two key

parameters: potential or excess charges at surface, and electric field or counter ions distribution in solution. When the EDL is confined at nanometer scale, in nanopores or nanochannels for example, the comparable dimension of nanopore size and EDL thickness lead to many novel transport features. The EDL or the ionic concentration near the nanopore orifice can be polarized by external electric field or pressure, also well known as ionic concentration polarization (ICP).[78] The potential induced ICP and its dynamics are the physical origins of many intriguing transport current patterns, including rectification, oscillation and hysteresis in transport current responses.[18, 95]

A representative potential-induced ICP inside a conical nanopore is shown in Figure 5.1. At a positive bias potential, both the negative surface charges and the external potential would facilitate the cations to migrate into the nanopore, resulting in the ion enrichment inside the nanopore; while under the opposite polarity, the opposite direction of the external electric field and the surface field would lead to ion depletion respectively. The ion enrichment and depletion will result in the high and low conductance, also well known as ionic current rectification. The enriched concentration of ions could be sufficiently high to induce salt precipitation that current responses oscillate due to particle blocking events. When applying a sweeping potential, hysteresis current responses are observed due to the dynamic or sluggish ICP process, especially at high frequency domain. Besides its fundamental importance, this ICP phenomena inside the nanochannels find important applications as well. Two types of applications are envisioned based on this interesting ion enrichment and depletion phenomena. The ion enrichment has been used for molecular concentrator to improve the detection limit and sensitivity.[13, 105]

On the other hand, the depletion phenomena has been used in separation, such as seawater desalination[14].

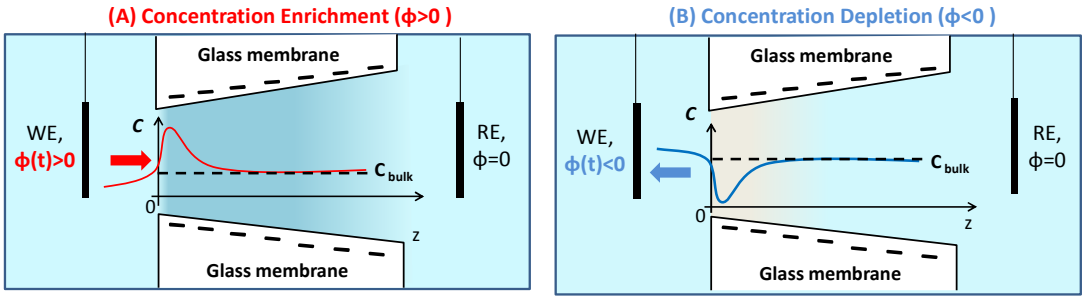

Figure 5.1 The bias potential induced ionic concentration polarization at the transport limiting zone inside a single conical nanopore. The concentration profile near the pore orifice will be enriched and depleted by the bias potential, and the dash line indicate the bulk concentration value.

Although the ICP phenomena have been widely studied, no quantitative model has been established that successfully explain the dynamic features discovered experimentally to best of our knowledge. Experimentally, it is very difficult to characterize the polarized charges as well as the nanopore properties as they are coupled and confined at nanometer scale, which cannot be accessed easily. On the other hand, from the theory perspective, the classical theory (Gouy-Chapman theory) is known to be ineffective to explain many nanoscale phenomena. The external electric field applied further complicates the analysis due to its impacts on the local ionic concentration profile and nanopore surface properties.

In this chapter, the polarized charge distributions and dynamics inside a conical nanopore are analyzed using the pinched hysteresis current-potential (i-V) loops. The enclosed areas in both i-V loops, at certain scan rates, are quantified to elucidate the respective enriched and depleted charges. The full picture of the ICP dynamics, including both time scale and total polarized

charges, were obtained by varying scan rates. A simple in-series RC charging/discharging model is successfully developed to describe the dynamic process. The surface properties as well as the geometry effect on the polarization dynamics are also investigated. Interestingly, the enriched charges vary with different surface and geometry properties, the total depleted charges are relatively constant, which is believed to directly reflect the total excess surface charges.

5.2 Experimental section

Single conical nanopore fabrication. Single conical nanopores are fabricated from bench-top method as previous reported.[77] Briefly, one end of the Pt wire (radius: 25 μm) is firstly attached to a tungsten rod with silver conductive paste. By using a waveform of 300 Hz and 4 V amplitude (BK Precision 4003A function generator), the Pt wire was electrochemically etched to form a sharpen nanotip in wt. 10% KCl and acetone solution, followed by sealing this tip into the glass capillary with thermal heating, and mechanic polishing to expose the Pt tip. Fully removal of the Pt wire sealed in glass would leave a conical nanopore which maintains the shape the Pt nanotip.

Electrochemical Measurements. The nanopores are filled with and then immersed into the same KCl solution, two Ag/AgCl electrodes inside and outside the nanopore are used to control the potential and collect the transport current. The Gamry Reference 600 potentiostat was used to conduct the cyclic sweeping potential tests. The sample rate for the cyclic sweeping potential measurements is 1 mV.

Numerical simulation. The finite elements simulation was performed by solving the Poisson and Nernst-Planck equations with COMSOL 4.2a. The simulation model and boundary conditions followed our previous reports.[63]

5.3 Results and discussion

5.3.1 Polarized charge distribution

When applying a sweeping bias potential, pinched hysteresis current loops with a cross point ($V = V_M$) were observed from single conical nanopores, as shown in the panel A from Figure 5.2: the forward scan current is always smaller than the one at backward scan, and pinched hysteresis loops are resulted. The current curves cross at an interesting non-zero point instead of the axis origin. This intriguing non-zero cross point represent one component of the surface field in the ion transport direction. At this point, the bias potential balances the averaged surface potential, and the net potential polarized charges would be zero, which is the initial state of the ion enrichment and depletion. Extra external positive or negative potential perturbation from this point would result in ionic enrichment and depletion respectively.

To better calculate the polarized charges, the current difference (Δi) between the forward (I_f) and backward (I_b) scan currents are shown in panel B. Noting at the cross point potential (at V_M, $\Delta i = 0$) rather than origin ($V = 0$) separates the ion enriched and depletion zone. The enriched and depleted charges at certain scan rate then can be easily calculated by the integration of the Δi over time duration t_D:

$$Q_{t_D} = \int_{V_M}^{V_2} \frac{\Delta i dV}{v} = S_{area} / v \qquad \text{(Eq 5.1)}$$

V_M is the cross point potential and V_2 are the potential limits, *v* is the scan rate, and S_{area} is the area enclosed inside each loop, shown as the shadow part. The different sign of the area indicates the polarization direction of the charges, either polarized into (enrichment) or away from (depletion) the pore orifice region. At a given scan rate *v*, the time duration is ΔV/*v*, the enriched and depleted charges can then be obtained, and including calculated charges at various time durations completes the full picture of the enrichment and depletion dynamics. At extremely high scan rates (short time duration), the polarized charge start from zero, and gradually increase to a threshold value at extremely low scan rates, under which condition the polarization process is finished and the system reached to the steady state.

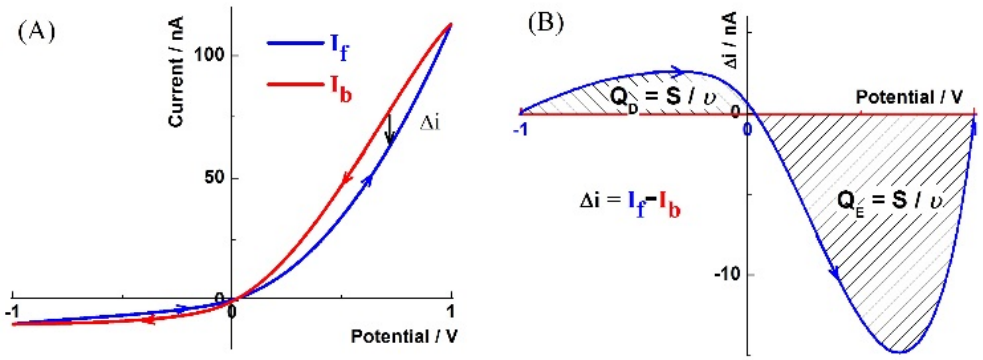

Figure 5.2 (A) Representative pinched hysteresis current loops separated by cross point from a single conical nanopore at a scan rate of 0.8 V/s. The arrows indicate the potential sweep directions. (B) The difference between the forward and backward current *Δi*, and the integrated polarized charges Q_E and Q_D, shown as shadow area divided by the scan rate *v*, and different sign of the area at the high and low conductivity states indicate the enriched and depleted charges respectively.

5.3.2 Mathematical model

The charges polarized by external potential would be analogous to the concept of charges accumulating at the plates of a capacitor, and the ion polarization dynamics would be comparable

to a capacitor charging/discharging kinetics. The total polarized charge Q_p at steady state under a potential window ΔV could be described by a capacitor ($C_p = Q_p/\Delta V$) and the resistivity of this polarization process can be represented by a resistor R_p. Then the time constant τ for this polarization process is $\tau = R_p C_p$.:

The charging current for an in-series RC circuit at a certain scan rate v would be:

$$i = vC_p(1 - e^{-t/R_pC_p}) \qquad \text{(Eq 5.2)}$$

During certain time period t_D, or $\Delta V/v$, the charge stored in the capacitor is:

$$Q_{t_D} = \int_0^{t_D} vC_p(1 - e^{-t/R_pC_p})dt$$

$$= vC_pt_D + vC_pt_D(R_pC_p/t_D)(e^{-t/R_pC_p} - 1) \qquad \text{(Eq 5.3)}$$

At steady state ($t = +\infty$), $Q_{t_D} = vC_pt_D = C_p\Delta V$ is the total polarized charges Q_p, and R_pC_p is the time constant τ, also noting that the charges I calculated from the hysteresis loops including both the charge and discharging process, which should be double of that in Eq 5.3, the final expression is then be,

$$Q_{t_D} = 2Q_p + 2Q_p(\frac{\tau}{t_D})(e^{-t_D/\tau} - 1) \qquad \text{(Eq 5.4)}$$

For small time duration t_D, or high scan rate v, the Taylor expansion of the exponential term is

$$e^{-t_D/\tau} = 1 + (-t_D/\tau) + 1/2(-t_D/\tau)^2 \qquad \text{(Eq 5.5)}$$

Then the polarized charge is:

$$Q_{t_D} = Q_p(t_D/\tau) \qquad \text{(Eq 5.6)}$$

A linear relationship between the polarized charge Q_{t_D} and the duration time t_D is expected at the small t_D region, and finally reach to the steady state $2Q_p$ at large t_D region. Noting that Q_p is

the total charges accumulating when reach to the steady state, or at extremely low scan rate, τ is the time constant of the charge enrichment/depletion process. t_D is the time duration, noting at different scan rate *v*, this time duration t_D is different. At low scan rate, or large t_D, the polarized charge Q_{t_D} would approach to a steady-state threshold value $2Q_p$; for small t_D, a linear relationship between the polarized charge Q_{t_D} and the duration time t_D, shown in Eq 5.6.

5.3.3 ICP dynamics

The charge enrichment and depletion dynamics from a 100 nm-radius nanopore in 50 mM KCl at different scan rates are shown in Figure 5.3. Obviously, both the enriched and depleted charges increase as the time duration increases and gradually reach to a threshold value. More interestingly, both of them can be quantitatively fitted (red line) with the proposed Eq 5.2, except small deviations at the small and large time duration regions. For this 100 nm radius nanopore, the total enriched charges are 21 nC and the time constant is 1.4 s; while the total depleted charges are about 0.87 nC, and the time constant is 0.4 s. The total enriched charges are about 20 times larger than the depleted ones.

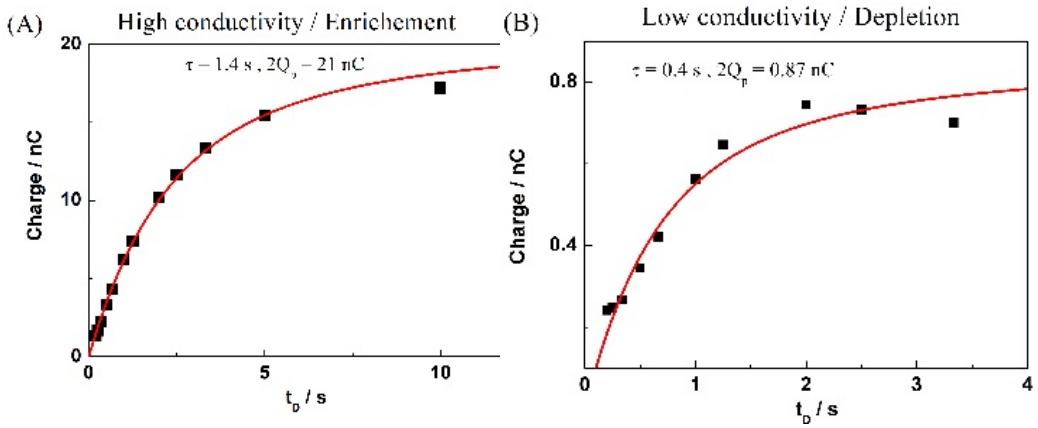

Figure 5.3 The fitting of the (A) enriched and (B) depleted charges (black dots) with proposed model (red lines) at different time duration t_D from a 100 nm-radius nanopore in 50 mM KCl.

Similar trend have been observed from two other nanopores. For a 35 nm-radius nanopore in 50 mM KCl, the total enriched charges are 4.9 nC and the total depleted charges are 1.0 nC. For a 46 nm-radius nanopore in 10 mM KCl, the total enriched charges are 22 nC while the depleted ones are 1.75 nC. Though the total enriched charges can be quite different from pores to pores, the depleted charges are relatively comparable (ca. 1 nC). Assuming the charge neutrality inside the nanopore, the total depleted charges are supposed to indicate the maximum amount of ions that can be depleted away from the nanopore, which should directly indicate excess surface charges on the substrate.

Two main factors accounts for the deviations between the experiments and proposed equation. It is known that, at high scan rates, another dynamic processes, the charging/discharging over the large glass membrane (capacitance is ca. 40 pF), would also contribute to and even dominating the current signals, thus the integrated charges would also include this component (the charges accumulate at the large membrane would be Q = 40 pF*1 V = 0.04 nC). This charging/discharging process is very fast (time constant is ca. 1 ms), so that this component is always concluded in when integrating the hysteresis current loops, especially at high scan rates. On the other hand, at very large t_D, the measured system is almost at steady-state, in which case pinched hysteresis current loops greatly decrease or disappear. The integrated polarized charges are therefore much smaller than expected. Other factors such as thermal fluctuations, asymmetrical inside and outside electrodes could also affect the applied potential and resulting current.

5.3.4 Physical meaning of RC component

Interestingly, in the ion enrichment case or at the high conductivity states, both the equivalent capacitance C_p and the resistance R_p have negative values, which is in agreement with the inductive loop in the Nyquist plot from the impedance measurements, as we reported previously. For the depletion process, however, regular capacitive loop or positive C_p and R_p are obtained. The physical meaning of this proposed equivalent polarization capacitor C_p would be one component (in the transport direction) of the EDL at the interior substrate/solution interface: at the high conductivity state, the surface electric field have an opposite direction to the applied electric field, resulting in a negative capacitance; while at the low conductivity state, regular capacitive charging/discharging loop displayed as the external and surface electric field has the same direction.

The in-series polarization resistance R_p would mean the surface contributed resistance: at high conductivity states, a negative value means surface enhanced conductance, and a positive value at low conductivity states indicate an increase of the total resistance of the system. Then the EDL structure at the solution/substrate interface could be revealed from the fitted values, including charges and time constants. It is worth pointing out the both equivalent C_p and R_p would dependent on the external bias potential, and thus the fitted values here would be averaged ones through the whole potential window ΔV. Next I will experimentally change the EDL structure and explore the ICP dynamics to further establish their correlations.

5.3.5 Surface charge density effect

The surface charges on the glass substrate origins from the dissociation of the surface silanol groups, and the surface pKa was found to be centered at ca. 5 at planar surface. By adjusting

the solution pH, the amount of the dissociated silanol groups, or surface charges can be controlled. The nanopore is the same 100 nm-radius one, the pH is varied by adding concentrated KOH and HCl in 50 mM bulk KCl solution. The polarization dynamics under different solution pH are then investigated and shown in Figure 5.4. The polarization dynamics can be fitted very well by the proposed equations, and the fitted total enriched and depleted charges at different solution pH are shown in panel C. It is not surprising to see an increase of both enriched and depleted charges as the solution pH increases, since high SCD would attract more counter-ions, and thus more ions there can be polarized inside the nanopore. The depleted charges, however, shows a more direct relationship with respect to the surface charges since a pH titration curve is displayed. Similar trends have been observed from two other pH dependent examples from 50 and 380 nm radius nanopores. Both enriched and depleted charges increase as the solution pH increases, however, the total depleted charges shows a more direct relationship with the surface charges.

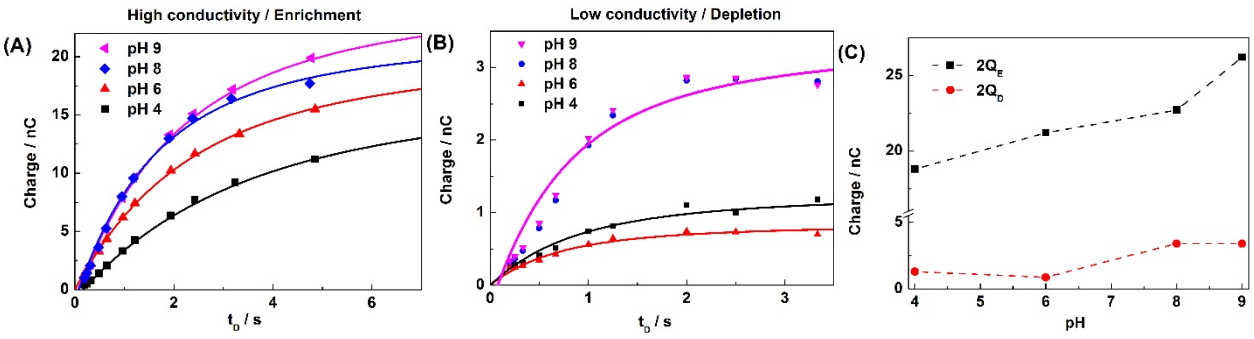

Figure 5.4 The pH effect on the polarized charges from a 100 nm-radius nanopore in 50 mM KCl. (A) Enrichment dynamics (B) Depletion dynamics at different solution pH. (C) The fitted total enriched $2Q_E$, and depleted charges $2Q_D$ at different pH.

5.3.6 Ionic strength effect

The ionic strength dependence of the polarization dynamics for this 100 nm nanopore at ambient pH (ca. 6.2, unadjusted) is shown in Figure 5.5. Panel A and B shows the enrichment and depletion dynamics at various ionic strength, and the fitted total polarized charges are listed in the panel C. It is expected to see the increase of both enriched and depleted charges as the solution concentration increases, since more ions are available to be polarized. Still compared to drastic increase of the enriched charges at different bulk concentration, the depleted charges are relatively unaffected. The small increase could come from the increase of the SCD as high ionic strength would facilitate the dissociation of the surface silanol groups.

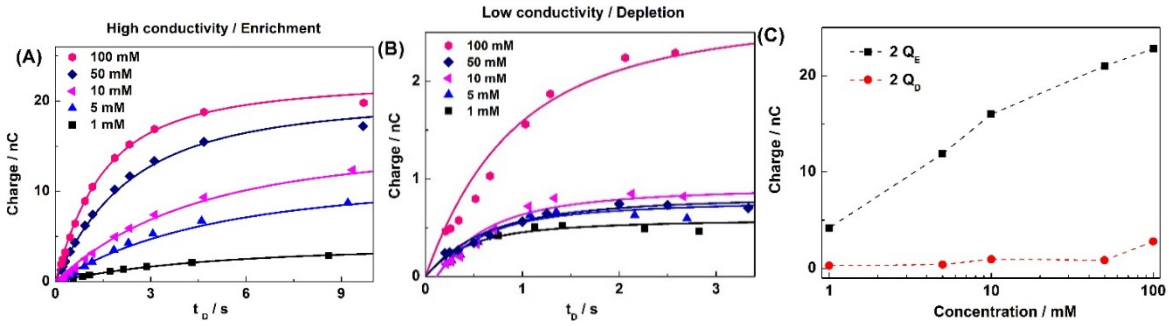

Figure 5.5 The ionic strength effect on the polarized charges from a 100 nm-radius nanopore in different KCl solution at pH 6.2. (A) Enrichment dynamics (B) Depletion dynamics. (C)The fitted total enriched $2Q_E$, and depleted charges $2Q_D$ at different solution concentration.

5.3.7 K^+ and Cl^- contribution

To better understand the ion contribution to the enrichment and depletion loops, the numerical simulation was conducted. The pinched hysteresis loops with non-zero cross point potential can be well reproduced by the numerical simulation based on Poisson and Nernst-Planck equations. An example was shown in Figure 5.6, the conical nanopore has a radius of 50 nm, the SCD is -50 mC/m^2 and the solution is 1 mM KCl. The hysteresis current response, and the contribution from K^+ and Cl^- are displayed. Interestingly, the total pinched hysteresis current loops consist of an inductive K^+ loop and a regular capacitive Cl^- loop. At the high conductivity states, both K^+ current and Cl^- current contribute to the total current responses though the enclosed current loops are mainly from K^+; while at the low conductivity, the current is mainly from K^+, and the enclosed loop is from the subtraction of K^+ loop from Cl^- capacitive loop.

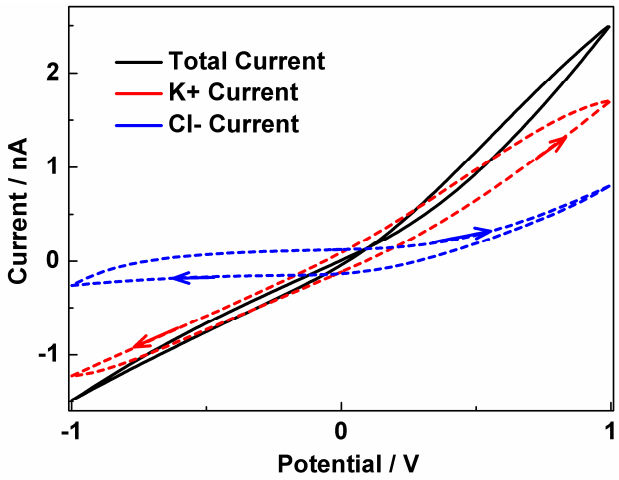

Figure 5.6 The simulated currents from K^+ and Cl^- at a scan rate of 200 V/s from a 45 nm-radius nanopore in 1 mM KCl with a SCD of -50 mC/m^2. The arrows indicate the potential scan directions. The pinched hysteresis current loops actually include a capacitive anion loop and an inductive cation loop.

5.3.8 Cations and anions polarization

The physical origin of both cations and anions polarization process are shown in Figure 5. 7. When applying a negative potential outside, as shown in the left part, the ions in the transport limiting zone will be depleted, and both Cl^- and K^+ migrate out from the nanopore. The anions act as a regular capacitor charging process with respect to the external electric filed, while the cations have an opposite polarization direction thus an inductive loop displayed. When switching the external polarities, both the cations and anions will be enriched at the transport limiting zone, the anions still have the same polarization direction to the external electric field and the cations still have an opposite one.

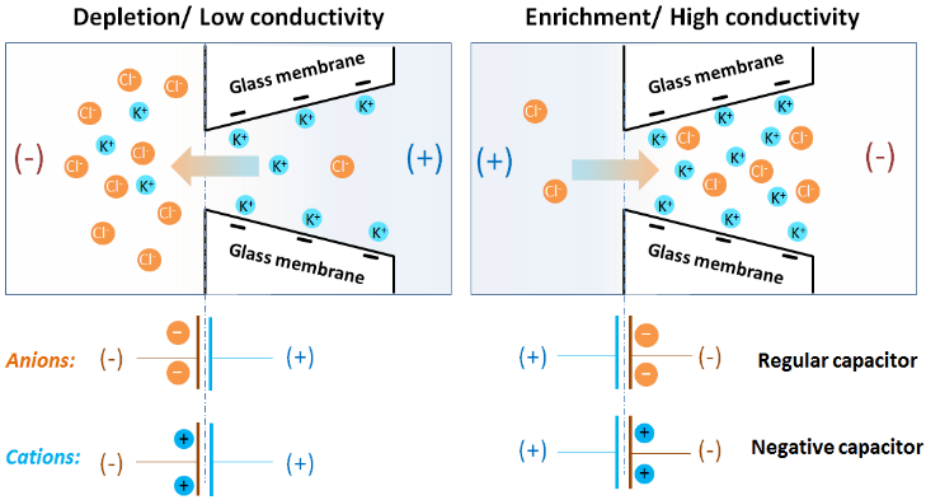

Figure 5.7 The physical origins of capacitive anion loops and inductive cation loops during the concentration polarization process. During the depletion process, both anions and cations are polarized outside the nanopore, while both ions are polarized during the enrichment process.

5.3.9 Quantification of the polarized charges in simulation

The pinched hysteresis loops at different scan rates are also obtained when applying a sweeping potential waveform in the simulation, as shown in Figure 5.8. Similar to the experimental results, inductive loops are displayed at the high conductivity states, while the low conductivity show a regular capacitive loop, and this two loop are separated by the non-zero cross points. The charges at both loops are then calculated and plotted with respect to the time duration, as shown in panel B and C. Surprisingly, the proposed polarization dynamics (Eq 5.4) also fitted the enrichment and depletion dynamics very well, and the total depleted and enriched charges can then be obtained. Compared to the experimental results, the total polarized charges are about 100 times smaller and the time constants are also about 50 times smaller than the ones obtained from the experiments. These disconnection between the simulation and experiments could come from the

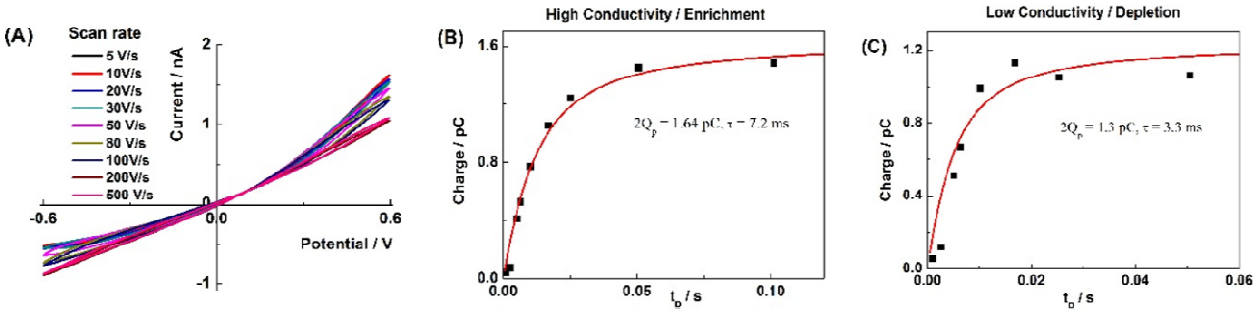

Figure 5.8 (A) The simulated i−V curves of a 50 nm nanopore at different scan rates in 1 mM KCl. (B) the enriched and (C) depleted charges at different time duration can also be fitted with the in-series RC charging model very well.

5.4 Conclusions

In conclusion, the dynamic ICP processes inside a single conical nanopore are investigated, mainly focus the charges distribution and their polarization dynamics near the pore orifice region, or the transport-limiting region. The enriched and depleted charges, polarized by the external bias, are quantified from the enclosed area in respective i-V loops, and their dynamics are fitted very well by a proposed in-series RC charging model. More charges inside the nanopore can be polarized in the case of higher SCD values of the substrate and solution ionic strength, and the depleted charges are found to directly reveal the surface charges. The numerical simulation results further tell the contribution from both ions, the pinched hysteresis loops include capacitive anion loop and inductive cation loop. This study complement our earlier reports of memristive mass transport behavior and a constant cross point potential, and now a comprehensive view of the EDL structure confined inside a nanopore can be seen, including both surface potential, concentration distribution, and its dynamics under external perturbations.

6 CHARGING SINGLE CONICAL NANOPORES: QUANTIFICATION of CHARGING DYNAMICS AND NONLINEAR STEADY STATE TRANSPROT

(The results in this chapter are unpublished)

In this chapter, the charging dynamics inside the nanopores are quantified under switching potentials. Different capacitive and inductive charging dynamics have been observed at the low and high conductivity states respectively, and their time constants and polarized currents can be modeled by a simple in-series RC equivalent circuit. The fitted depleted currents are relatively constant at different potentials and concentration, while the enriched currents are linear to both applied potentials and potential steps. Moreover, a very simple equation have also been developed to quantitatively describe the rectified current-potential relationships from single conical nanopores.

6.1 Introduction

Interesting rectified ionic currents have been observed in various nanopore devices with asymmetrical geometry and/or surface charge distribution.[23] As demonstrated in Figure 6.1, two different current responses i_1 and i_2 are recorded at two different potential V_1 and V_2, and the potential and current relationship do not follow simple linear ohm's law. When switching the potential from V_1 to V_2, the corresponding currents will change from V_1 to V_2 respectively. There are several interesting questions need to be answered during this process. 1) How long will it take for the i_1 change to i_2, and what factors would affect this time durations? 2) How would i_1 change to i_2, following what type of charging mechanism? 3) Can we finally develop a simple equation to describe the relationship between currents and potentials? The answers to these questions not only help understand the current dynamics in the single nanopores, but

also directly applies in many practical systems that involve the nanoscale transport processes, such as the supercapacitors with nanostructured electrode.

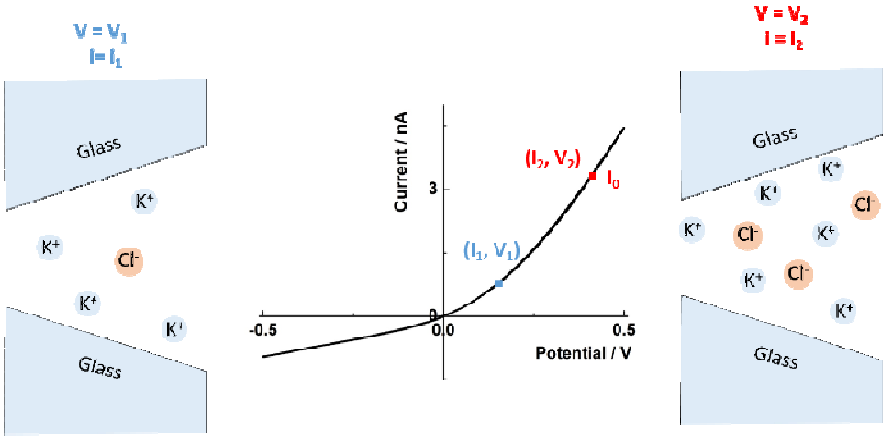

Figure 6.1 Representative nonlinear current-potential curves in single conical nanopores. The transport currents are n not proportional to the potentials, when switch the applied potential from V_1 to V_2, the currents will change from i_1 to i_2 correspondingly.

Different dynamic processes are known to contribute to the current responses in nanopores, including the membrane charging/discharging, dynamic polarization processes, and ionic current rectification at steady states.[63] Dependent on the polarity of the applied potential and surface potential, the concentration profile can be either enriched or depleted. The dynamics of both enrichment and depletion at certain potential window have been quantified based on the capacitive and inductive i-V loops under different scan rates, and an in-series RC component have been proposed to describe the polarization dynamics, as included in chapter 5.

The quantification of the dynamic charging would also help understand steady-state current responses of the conical nanopores. Quantification of the transport current through nanopore is of great fundamental importance for the nanopore-based sensing applications. Due to the strong interfacial interaction and nanoscale geometry, the transport current through nanopores

reveal both surface and geometry effects. Many other factors such as potential and ionic strength are also known to affect the currents, albeit their quantitative correlation have never been established. For the nanopores in solutions with extreme high ionic strength, the surface effect will be negligible due to the screening effect, and the transport feature is thus close to their bulk counterpart. At low concentration, the strong surface effect is expected to result in more rectified currents. However, various experimental and simulation have shown that the highest rectification factor actually lies in a medium concentration zone, around 100 mM, and an inverted rectification direction is observed for nanopores with extreme low concentration profile.[82] Besides, though various simulation work have successfully describe the ionic rectification in nanopores, the expressions are generally very complicated. The simple expression that describe the nonlinear i-V curves has not been established yet.

In this chapter, these questions will be addressed via both experiments and numerical simulation. Briefly, the step-potential waveform was applied on the conical nanopore and its charging/discharging dynamics are quantified. In addition, the ionic strength and the surface charges effect on the polarization dynamics are also investigated. The quantification of the nonlinear current response are also included in the second part of this chapter, basically an empirical equation was proposed to describe the rectified currents at various SCD, concentration and potentials.

6.2 Results and discussions

6.2.1 Polarity dependent polarization dynamics

The representative i-t curves under various potentials are shown in Figure 6.2. Clearly transient dynamic currents are resulted when switching the potentials. Here, we always step the po-

tential from lower to higher to allow more direct comparison, so that the concentration profile in the transport limiting zone would always be enriched, such as -0.4 to -0.3 V and 0.4 to 0.5 V. However, two different type of transition behaviors are displayed: at low conductivity states, -0.4 to -0.3 V for example, the currents first increase, then gradually decrease and finally reach to steady state, following a regular capacitive charging dynamics. While at the high conductivity states, the current increases first, and then keep gradually increase and finally reach to the steady state, following an inductive charging dynamics. More interestingly, both the regular capacitive and inductive dynamic currents followed an exponential decay with respect to the times, as fitted in panel B and C.

The potential dependent capacitive and inductive charging dynamics agree with our earlier reported pinched hysteresis current curves under sweeping potentials. A regular capacitive loop and inductive loop are displayed at the low and high conductivity states. As the in-series RC circuit can be used to describe the polarization dynamics, both the enrichment and depletion dynamics can be quantitatively fitted by the exponential decay equations:

$$i_t = i_p e^{-t/\tau} + i_2 \qquad \text{(Eq 6.1)}$$

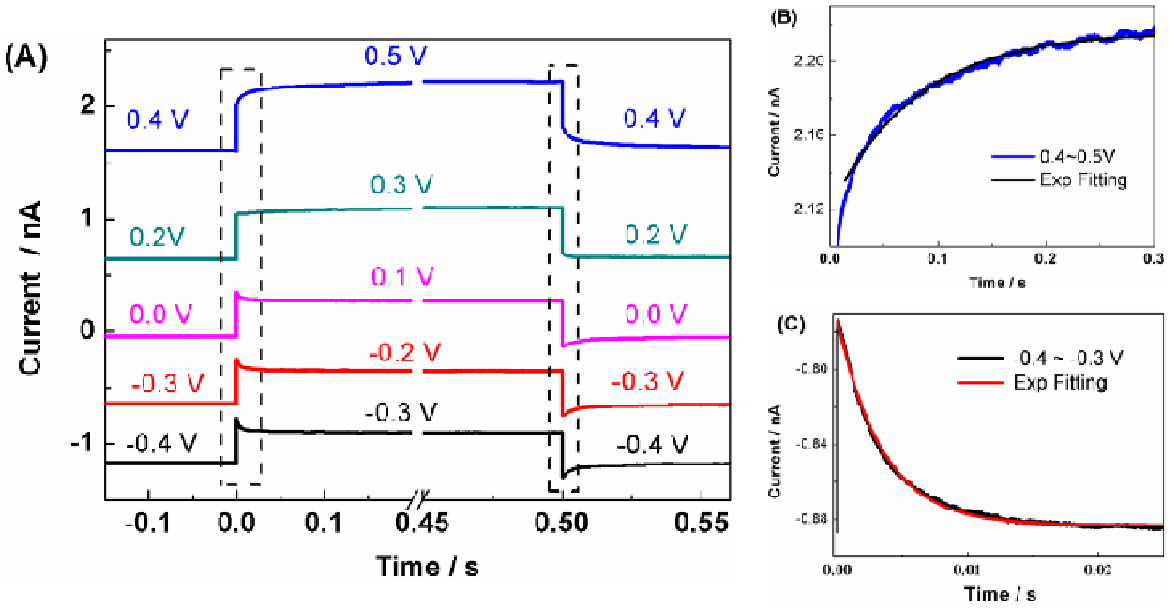

Figure 6.2 (A) The i-t charging curves for single conical nanopores under respective potentials. Different transition current patterns are displayed at the positive and negative potentials, as highlighted inside the dash boxes. The inductive and regular capacitive charging dynamics are shown at the high and low conductivity states, as fitted by the exponential decay patterns, shown in panel (B) and (C).

Since the dynamic currents at transition zones origin form the potential induced polarization, the pre-exponential current i_p is therefore defined as the polarized contributed current. At high and low conductivity states, the i_p have different signs, I define here the i_p at the high conductivity is negative while the i_p at the low conductivity is positive to follow regular capacitor charging dynamics. The time constants τ represents the time constants of the polarization process and i_2 is the current at the steady states under potential V_2 ($t = \infty$). At $t = 0$, $i_0 = i_p+i_2$. Due to the slow concentration polarization process, assuming the concentration profile immediately after potential switching ($t=0$, $V = V_2$) are not changed, thus its conductance ($G=G_1=i_1/V_1$) are also unchanged. At this specific moment, $i_0 = V_2*G= i_1*V_2/V_1$, and therefore

$$I_p = i_2-i_0 = i_2- i_1*V_2/V_1 \qquad \text{(Eq 6.2)}$$

Noting that i_p describes the polarization induced currents, it is not i_2-i_1 and also not just the surface currents. Also i_p is not time dependent, the dynamic processes are described by the exponential term.

6.2.2 Polarization at different potentials and concentrations

The polarization dynamics at different potentials and concentrations are displayed in Figure 6.3. In each concentration, the time constants slightly increase when the final potential goes higher; but they are relatively the same in various concentrations, and the time constants are generally about 0.5 to 1 s.

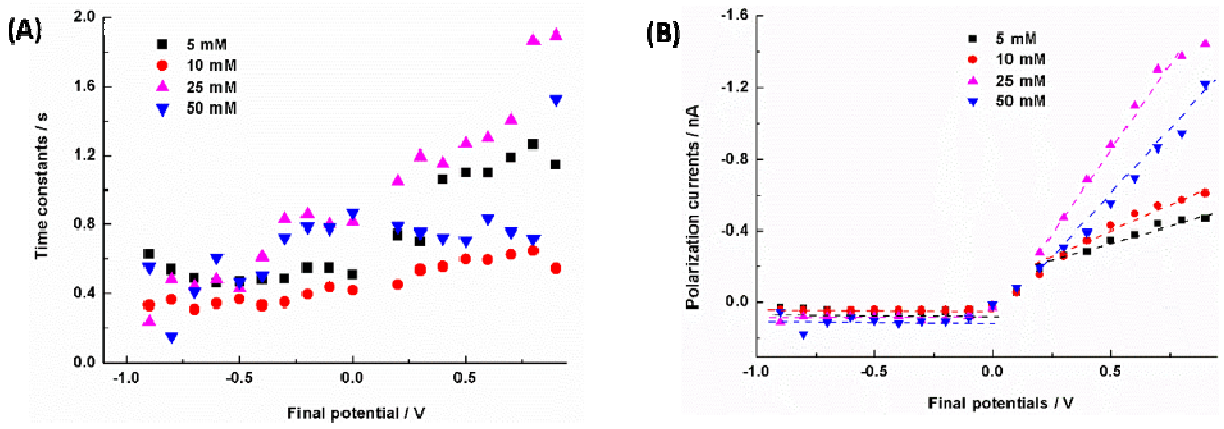

Figure 6.3 The (A) time constants and (B) polarized currents at different final potentials with constant +0.1 V step. Clearly two different trends are shown at the low and high conductivity states. At the low conductivity states, the surface polarized currents are relatively the same, while at the high conductivity states, the surface polarized currents display a linear relationship with the potential.

In panel B, the polarization currents are plotted with respect to the final potentials and the step size of the potential is constant 0.1 V. The polarization currents at the low and high conductivity states, or depletion and enrichment currents, show different trend with respect to the potentials. At the low conductivity states, the depletion currents are relatively constant at all

different potentials and concentrations. This may can be explained by the charge balance inside the nanopore, the total amount of ions inside the nanopore that can be enriched are determined by the surface charges.

At the high conductivity states, the enriched currents display a simple linear relationship with the applied potentials ($i_p = k_1$ V). In different concentrations, the enriched current generally increase as the concentration increase, from 5 mM to 25 mM, but then it decreases at 50 mM and a maximum enriched currents are observed in a medium concentration around 25 mM. This result is in agreement with the concentration dependence rectification factors observed from various nanopores, the highest rectification factor is observed at a medium concentration, further increase and decrease of the bulk concentration would decrease the rectification factor.

6.2.3 The potential step denpdence and the equivilant RC values

The the polarized currents ($\Delta V = V_2$-V_1) at different potential steps (varying V_1 but constant V_2) are also investigated, as shown in Figure 6.4. The polarized currents and time constants at various potential steps are also calculated in panle B, C, E and F. All the transient currents at both -0.5 and 0.5 V can be fitted with the Eq 6.1 very well, and the fitted paratmers are plotted with the potential steps as well. Both the enrichment and depleted currents show a very linear relationship with the potenital steps ($i_p = k_2 \Delta V$) and the time constants are relatively constant. The equivilant resistance and capacitance can then be calculated. The negative value at the high condcutivity states indicate a decrease in the total resistance, and the negative capacitance indicate that the concentration enrichment direction is opposite to the electric double layer direction at the substrate/solution interface.

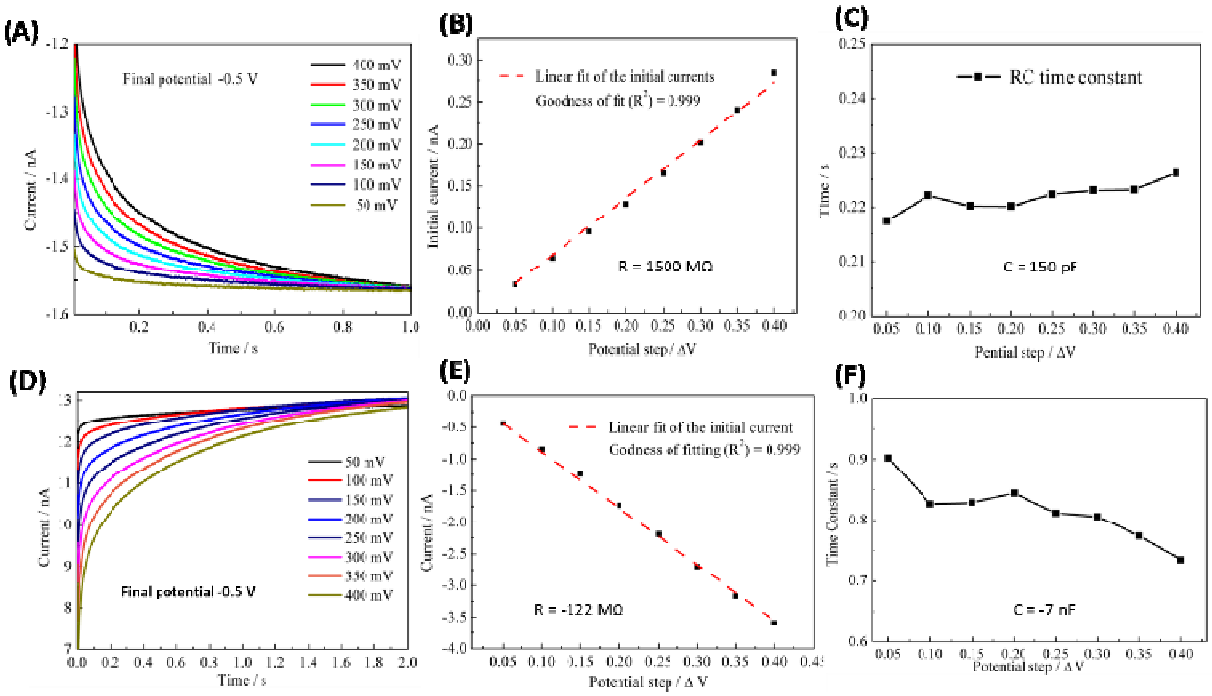

Figure 6.4 Potential step effects on the polarization dynamics, and the fitted equivalent capacitance and resistance at both high (A, B and C) and low conductivity (D, E and F) states. A proportional relationship is displayed between the potential steps and the simulated currents while the time constants is relatively constant at different potential steps.

Therefore, at the high conductivity states, the enriched currents show linear relationship with both final applied potential and potential step when keeping one of them as constant, which can be expressed as $i_p = k_1k_2\ V\ \Delta V$, where k_1k_2 would be a constant that only depend on the surface charges. Assuming i= 0 at V=0 with a conductance of $G_{V=0}$, then staring from V = 0, step to V_2, with equation Eq 6.2:

$$I_p = i_2 - i_0 = k_1k_2\ V\ \Delta V \qquad \text{(Eq 6.3)}$$

$$i_2 - V_2 * G_{V=0} = k_1k_2\ V_2\ (V_2 - 0) \qquad \text{(Eq 6.4)}$$

$$I_2 = V_2 * G_{V=0} + KV_2^{\,2} \qquad \text{(Eq 6.5)}$$

Assuming at V=0, the conductance is close to the volumetric conductance, therefore the steady state currents at V_2 can be expressed as:

$$I_2 = GV_2 + kV_2^2 \qquad \text{(Eq 6.6)}$$

To best of our knowledge, Eq 6.6 is the first simple equation proposed from the experimental results to describe the current-potential curves at high conductivity states in single nanopores. The first term is the volumetric contribution and the second term is the surface contribution.

6.2.4 Surface charge dependence

The surface charge effect on the enrichment and depletion currents at -0.5 and 0.5 are also investigated, as included in Figure 6.5. The slope are calculated from the polarized currents at different potentials steps, and the calculated slopes or conductance at different pH are included in panel c. A titration curve are displayed between the polarized conductance at both -0.5 and 0.5 V, which suggest a linear relationship between the polarized currents and surface charge density.

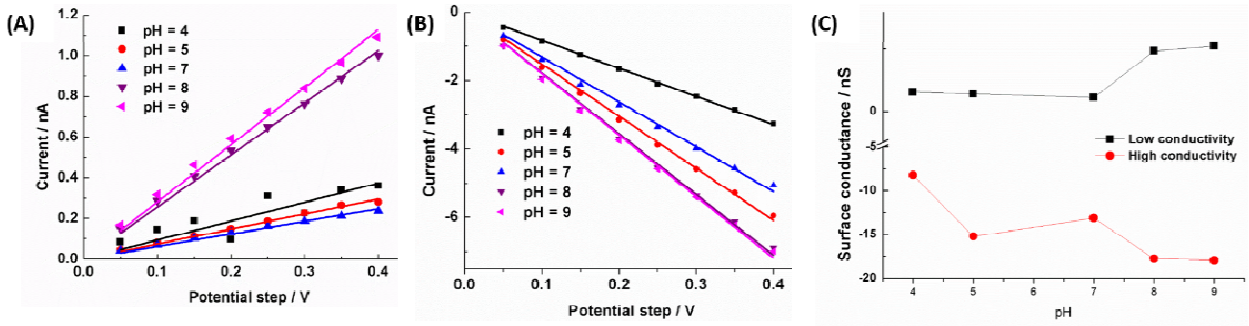

Figure 6.5 The surface charge effects on the polarized currents at (A) -0.5 and (B) 0.5 V. (C) shows the depleted and enriched conductance, and a titration trend suggests a simple linear relationship between the surface charges and polarized charges.

6.2.5 Simulated enrichment and depletion dynamics

The transition features of the nanopores at switching potentials are also investigated with the numerical simulations, as shown in Figure 6.6. Noting that I do not include the large membrane in the model so that all the currents are from the ion transport process through nanopores, instead of the charging/discharging processes at the large glass membrane. The applied potential waveform and the responding current responses are shown. Similar to the experimental results, regular capacitive and inductive charging dynamics are observed at the high and low conductivity states, as represented with -0.3 V and 0.3 V. The fitted time constants are relatively similar, about 3 ms, which is about 50 times smaller than the experimental values.

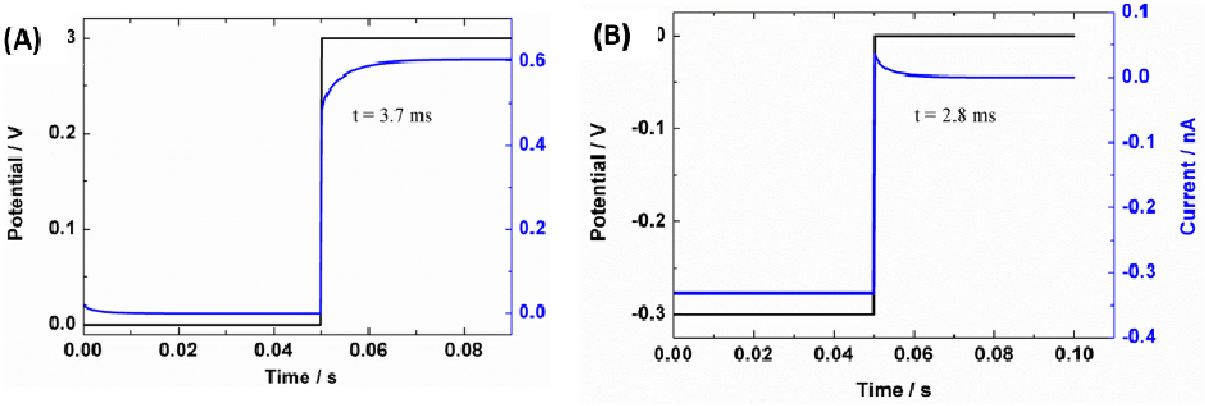

Figure 6.6 The simulated charging currents in single conical nanopores at the high and low conductivity states.

6.3 Steady-state current simulation

After the quantification of the charging dynamics, the polarized currents analysis would also be helpful to the quantification of the nonlinear currents at steady states. For example, a parabolic relationship has already been established between the current and potentials, the linear relationship describes the geometric conductance while the square potential relationship describes the surface currents (Eq 6.6). In this part, an empirical equation was further developed

to describe the rectified currents in single conical nanopores at the steady states based on the numerical simulation. The surface charge density (SCD), potential, concentration, and geometry have been systematically varied and the corresponding currents are simulated and analyzed. Surprisingly, the proposed empirical equation also works well to describe the rectified currents in experiments.

6.3.1 Simulated current at different SCD

The SCD plays an important role in the resulting current responses, as the EDL and local concentration profile inside the nanopore will be different. I have found the simulated current display a simple linear relationship with the surface charge density values, as shown in Figure 6.7. The intercept at the zero surface charge density would indicate the geometry currents at this specific potentials. More interestingly, the linear relationship is displayed at various potentials, as illustrated in the panel B. This can be simply explained by the charge balance inside the nanopore, for a nanopore with fixed geometry, the concentration profile at the transport limiting zone would be proportional to the surface charges, so that the conductance and currents at certain potential would also show linear relationship with the SCD values. Therefore, the slope between the simulated currents and SCD would only be a function of the potential, geometry and concentration, noting that the geometric current is shown as I_b.

$$I_T = I_s + I_b = K(V, r, c)*SCD + I_b \qquad \text{(Eq 6.7)}$$

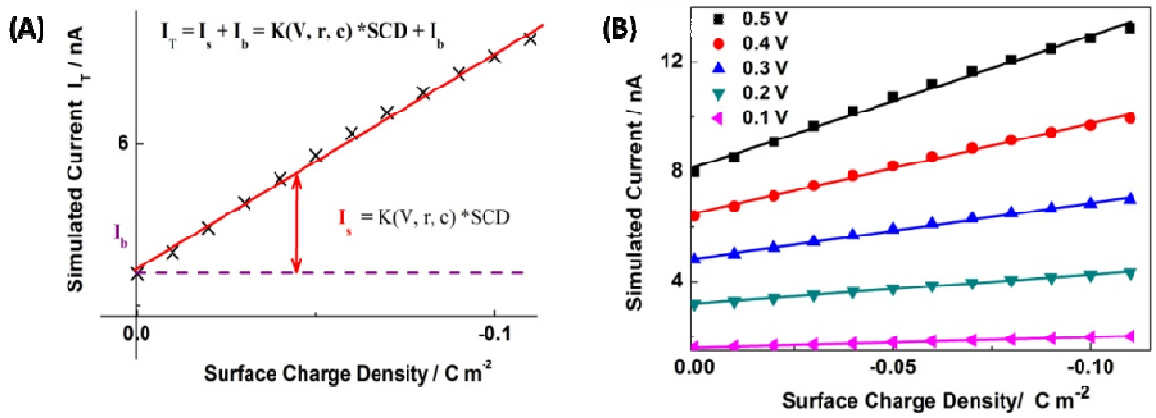

Figure 6.7 The surface charge density dependence of the current responses at various potentials. A simple linear relationship was displayed between the SCD and simulated currents.

6.3.2 Potential dependence

The relationship between the potential and currents are displayed in Figure 6.8. A square relationship was proposed between the surface currents and applied potentials, and the proposed equation fit the simulated current very well, as shown in the panel A. The simulated currents at different concentrations are also offered. As expected, the geometrical currents show linear relationship with the applied potentials, as described by the ohm's law.

$$I_T = I_s + I_b = K(r, c)*SCD*V^2 + G_b V \quad \text{(Eq 6.8)}$$

The results actually are in perfect agreement with the equation (Eq 6.5) I developed from the polarized currents of nanopores. The square could be explained by the potential induced polarization. Assuming a simple RC circuit describes the polarization processes, thus the polarized charge, or concentration would be q=VC. Since the conductance is proportional to the concentration, then the current would be I = GV=k VC*V= KV^2.

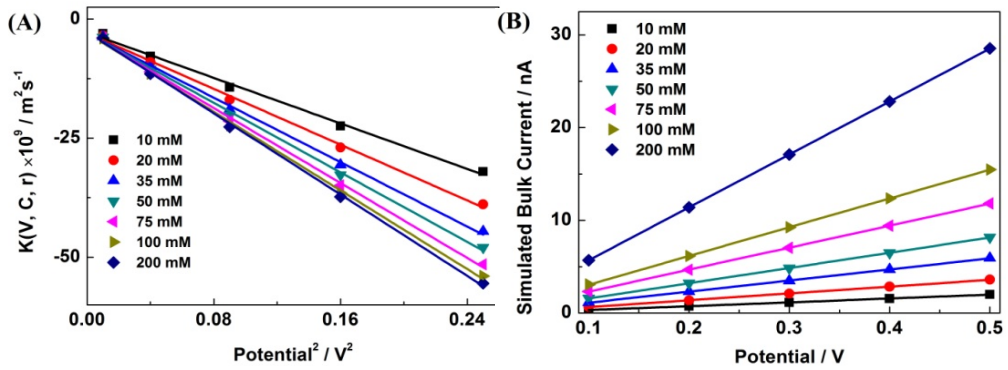

Figure 6.8 The potential dependence of the surface and bulk currents. At various concentrations, the surface current display a linear relationship with the potential square, while the bulk currents show simple linear relationship with the potentials, as expected from the ohm's law.

6.3.3 Concentration effect

After normalize out the potential effect, the leftover slope from Figure 6.8 is then would be only function of concentration and radius. The relationship between the polarized concentration and bulk value are proposed in the panel A:

$$C_p = C_b e^{-\sqrt{c_b}/A} \quad \text{(Eq 6.9)}$$

Two terms are included in the proposed Eq 6.9, the exponential term describe the surface effect, high bulk concentration would result in a smaller surface effect, thus a small value of exponential term. The bulk concentration C_b represent the total amount of ions that can be polarized. At extreme low concentration, though the charged surface can polarize more ions (large exponential term value), but there are not too many ions can be polarized (small C_b). The combination of two would describe the polarized charges at different bulk concentrations, the decay constant A would be a function of the geometry. Several arbitrary numbers are selected and the resulting relationship are plotted to show the trend. Qualitatively, the maximum value displays at medium concentration, which agrees with the trend of the rectification factor in dif-

ferent concentrations. The proposed equations works very well to describe the simulated currents, as demonstrated in the panel B.

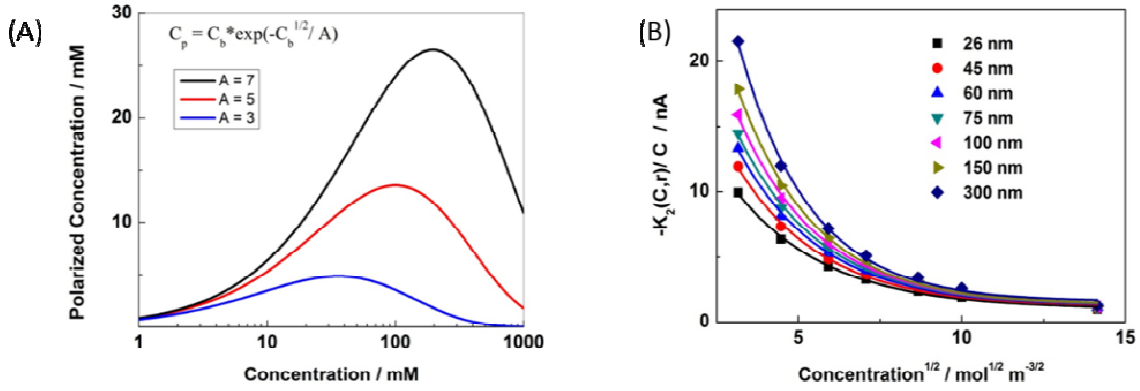

Figure 6.9 The concentration dependence of the polarized charges are proposed in panel A, and the proposed equation work very well for the simulated currents at various radius, as shown in panel B.

6.4 Experimental results

Interestingly, the proposed equations work very well to describe the rectified currents from conical nanopores very well, as shown in Figure 6.10. The radius of the nanopore is 56 nm. The nonlinear rectified i-V curve at the high conductivity states can be fitted by the proposed parabolic equation. The fitted parameters in various concentrations are plotted in panel B and C. The fitted bulk conductance have an excellent relationship with the concentration, while the fitted surface conductance also display an exponential relationship with respect to the square root of the concentration after normalized by the concentration c. Basically, the proposed Eq 6.8 and 6.9 also work well in the experiments.

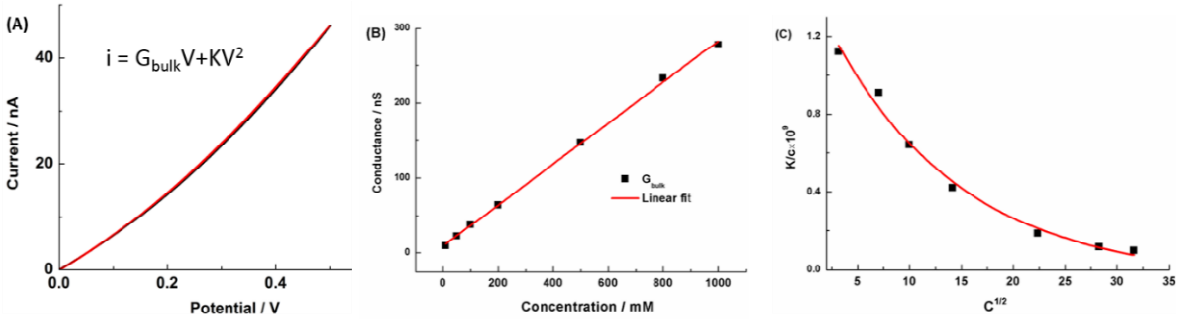

Figure 6.10 (A) Fitting of the experimental i-V curves recorded from a 56 nm radius nanopore in 100 mM KCl with the proposed parabolic equation. (B) The fitted bulk conductance do display a linear relationship with the concentration, and (C) the fitted surface currents also follows Eq 7.3, an exponential relationship was displayed between the normalized current (K/c) and square root of the concentration.

6.5 Conclusions

In this chapter, the charging dynamics of the single conical nanopores are investigated by applying step potential waveform. The regular capacitive charging dynamics are observed at the low conductivity states, while at the high conductivity states, the current dynamics follows an inductive charging dynamics. The time constants at different potentials and concentrations are relatively constant, and generally in the range from 0.5 to 1 s. The depleted currents are relatively constant at the low conductivity states, which believe reflect the surface charges of the nanopores. At high conductivity states, a very simple linear relationship was observed between the polarized currents and final potentials. Most importantly, a parabolic equation have been developed to describe the current-potential relationships of rectified currents in nanopores.

In the second part, the ionic current rectification features observed from conical nanopores are quantitatively described by an empirical equation developed from the simulation. A simple linear relationship was observed between the SCD and current values. The total currents include the geometric and surface currents, which display a linear and square relationship with

the applied potential respectively. In addition, the concentration dependence of the surface currents are also offered. The empirical equations are further validated by the experimental results, as the steady state currents can be well fitted by the equations.

7 ELECTRONIC TRANSTION IN THIOLATE PROTECTED GOLD NANOCLUSTERS

(This chapter mainly includes two papers:
1. Ahuja, T.; Wang, D.; Tang, Z.; Robinson, D.; Padelford, J.; Wang, G.*, Electronic Coupling between Ligand and Core Energy States in Dithiolate-Monothiolate Stabilized Au Clusters. *Phys. Chem. Chem. Phys.* **2015***, in press*. Reproduced by permission of the PCCP Owner Societies.
2. Wang, D.; Padelford, J.; Ahuja, T.; Wang, G.*, Transitions in Discrete Absorption Bands of Au_{130} Clusters upon Stepwise Charging by Spectroelectrochemistry. *ACS Nano* **2015**, accepted.)

In this chapter, the electronic transitions in thiolate protected Au nanoclusters are investigated from various electrochemical and optical measurements. This chapter mainly include three parts: 1) firstly the ET transfer of the gold core, core-ligand interface and ligands Au_{130} clusters stabilized by a monolayer of di- and mono- thiolate ligands are systematically studied via multiple electrochemical techniques. The redox features of the core, ligands and their interplays are quantified. 2) Secondly, spectroelectrochemistry analysis is then employed to resolve previously inaccessible electronic transitions in Au_{130} clusters by selective electrolysis to different core and ligand charge states. Subsequent analysis of the corresponding absorption changes reveal that different absorption bands originate from different electronic transitions involving both metal core energy states and ligands molecular orbitals. An energy diagram is proposed that successfully explains the major features observed in electrochemistry and absorption spectroscopy. 3) Lastly, after figuring out the electronic structure and energy diagram of the nanocluster, its electrochemiluminescence (ECL) features was primary investigated, different

ECL patterns have been observed, corresponding to different electronic transitions in the nanoclusters.

7.1 Introduction

Metal clusters have attracted extensive research interest in nanoscience, classic inorganic chemistry and electrochemistry due to their rich and tunable electrochemical, optical and other properties. Gold nanoclusters stabilized by a monolayer of thiolate ligands[109-112] gained extensive research attentions recently primarily for two reasons: the discovery of a unique thiol bridging (RS-Au-SR) motif at the core-ligand interface,[113-115] and the elucidation of atomic/molecular compositions.[116-117] The information could potentially enable definitive structure-function correlation, which is an important question that challenges broadly defined nanomaterials research. The extraordinary stability of the Au nanoclusters, facile synthesis and isolation, and readily tunable properties make them excellent prototype systems and promising candidates to establish this fundamentally significant concept for broad applications.[118-119]

Controlled resonance coupling between the metal core energetics and ligand energy states has not been established experimentally. Such electronic coupling could add another dimension to tailor the properties of these functional metal clusters. The rationale is rooted on ligand-metal charge transfer, a widely adopted concept in classic inorganic chemistry. The charge density shift via electron resonance between metal ion center and ligand orbitals are often accompanied with changes in absorption, luminescence and electrochemistry activities. Similarly, new properties could emerge from the electronic coupling between the core and the capping ligands of the gold nanoclusters or other nanomaterials.

Two criteria are believed keys to achieve and to manifest the electronic coupling: 1. Metal cores with well-defined energetics and 2. Proper linkers between the metal core and the structure of the ligand molecules that have accessible orbitals. Inert ligands are typically employed serving the primary function to stabilize the metal cores. Correspondingly, the ligands themselves, excluding the sulfur atoms that bound with Au core, are generally believed to have negligible contributions to the overall energetics of Au nanoclusters. Ligands with accessible energy states, such as electroactive molecules as redox probes, have been introduced as part of the ligands to a variety of nanoparticles, especially with Au nanoclusters. Albeit multi-electron transfer activities have been observed corresponding to those redox molecules, the impact by the nanoparticles on the electrochemical potential of the redox probe was unremarkable. The observation suggests negligible electronic coupling between the nanocore energetics (Au and S) and the molecular orbitals of the redox probes, often at the outer surface separated from the Au-thiolate interface by the linker portion of the ligands.

The energetics of Au nanoclusters is routinely characterized by electrochemical and optical methods. Multiple electron transfer peaks separated by relatively uniform charging energy have been observed over wide potential range in voltammetry studies from Au nanoclusters with relatively larger cores (i.e. Au_{130} and $Au_{140\text{-}147}$). Each peak represents single electron transfer activity, which is well-known as quantized double-layer (QDL) charging or Columbic staircase behaviors. For those Au nanoclusters with relatively smaller core size (i.e. Au_{13}, Au_{25}, Au_{38}, Au_{55} and Au_{75}), molecular-level energy states emerge in voltammograms that can be correlated with the discrete absorption bands in UV-visible spectra. The experimental energy diagrams and structural information of several Au nanocluster systems are often employed to validate and to

gain fundamental insights from density function theory calculations. The contribution of the ligands to the overall nanoclusters energetics is primarily evaluated by Au-S bonding, i.e. in superatom theory.

At the transition size range from small molecules to plasmonic Au nanoparticles, discrete absorption transitions or intensity decays with less distinct features can be observed in UV-visible-near-infrared spectrum range from different Au clusters. Electrochemically, quantized double layer charging and split HOMO-LUMO type electron transfer (ET) behaviors have been observed from larger (i.e. more than 100 Au atoms) and smaller (few tens) clusters respectively. Electrogenerated chemiluminescence (ECL) has been reported recently enriching the electrochemical and optical activities of these Au clusters. Once photoexcited, the Au clusters display broad and intense near IR photoluminescence (i.e. 650 nm-1000 nm) with long lifetime (up to microseconds), suggesting an energy relaxation process. While atomic orbitals from Au (d) and S(sp) have been employed to explain some optical and electrochemical features, the respective contributions of Au, S and the remaining ligand molecular orbitals to individual optical and electrochemical transitions remain to be established for various clusters. Further, because the remaining portion of the ligands, other than sulfur atoms that bind to Au as considered in most cases, is mostly inert in earlier studies, whether the molecular orbitals of the ligands (if adopted and within the energy range) could interact with or affect the electronic transitions of Au clusters remain to be established experimentally.

In this chapter, the electronic transitions involving both Au_{130} nanocores and the stabilizing durene-dithiolate ligands and their interplay are first quantified.[120] Strong coupling between the Au core and ligand energy states is evidenced for the first time by multiple electrochemical

techniques. Scan-rate dependent cyclic voltammograms reveal single electron transfer QDL charging behaviors at lower potentials; while single-step multiple electron transfers (ETs) involving ligand energy states are observed at higher potentials.

Based on the electrochemical features of the Au_{130}, subsequent analysis of the corresponding absorption changes under controlled charge states of the core and ligands. The spectroelectrochemistry results reveal the absorption bands originate from different electronic transitions involving both metal core energy states and ligands molecular orbitals. An energy diagram is proposed that successfully explains the major features observed in electrochemistry and absorption spectroscopy. The electrochemiluminescence of this Au_{130} nanocluster was primary investigated based on the proposed energetic structures.

7.2 Experimental section

Chemicals. Tetrachloroauric acid trihydrate ($HAuCl_4 \cdot 3H_2O$, >99.99%), 2-phenylethanethiol (PET, >99%), tetraoctylammonium bromide (TOABr, 98%), sodium borohydride ($NaBH_4$, 99%), tetrabutylammonium perchlorate (TBAP, >99%), and all other solvent (HPLC grade) including toluene, methanol and CH_2Cl_2 were all used as received from Sigma-Aldrich. Durene-α_1, α_2-dithiol (Durene-DT, >95%) was obtained from TCI-America.

Instruments. The UV-vis absorbance spectrum was recorded with Shimadzu UV-1700 spectrophotometer. A CH instrument 700C electrochemical workstation was used in electrochemical measurements.

Au_{130}(Durene-DT)$_{29}$(PET)$_{22}$ synthesis and characterization. The synthesis and purification procedure of Au130 nanoclusters mainly follow previous reports.[120] Briefly, the gold salt

($HAuCl_4 \cdot 3H_2O$) was first phase-transferred into toluene with TOABr, followed by adding in a mixed Durene-DT/PET solution under stirring, and the final ratio of Au/Durene-DT/PET is 1.5:1:2. Then freshly prepared $NaBH_4$ (20 equiv. of gold) aqueous solution was added. After 3 days, the organic layer was separated and washed with water and then precipitated by methanol. The Au_{130} nanoclusters composition was confirmed by the UV-vis and MALDI following previously described analysis. The composition of the synthesized Au_{130} nanoclusters are shown in Figure 7.1.

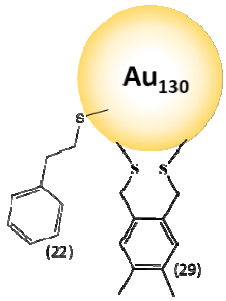

Figure 7.1 The composition of the synthesized Au_{130} nanoclusters stabilized by mono- and di-thiolates.

Electrochemistry. All the electrochemical tests were conducted in CH_2Cl_2 solvent containing 0.1 M TBAP as supporting electrolyte, and all the solutions are purged with Argon gas for 20 min prior to testing. The Au_{130} nanocluster concentration is around 0.1 mM. The working electrode was a 0.24 mm-radius Pt disk electrode. Before use, this Pt electrode was polished with alumina oxide powder, washed and sonicated with water, acetone and CH_2Cl_2. The counter electrode was Pt foil, and Ag/AgCl wire was used as quasi-reference electrode (QRE). The potential of the AgQRE (0.22 V vs. SHE) was calibrated by measuring the ferrocene (Fc^+/Fc) redox peak at 0.48 V.

Spectroelectrochemistry: A three electrodes electrochemical cell was built in a thin quartz cuvette. Bulk electrolysis was performed with WaveNano potentiostat (Pine Instrument) using a

large Pt mesh as working electrode, a Pt foil counter electrode and an Ag wire quasi-reference electrode. The concentration of the Au_{130} nanoclusters was around 10 μM, and 0.1 M TBAP used as supporting electrolytes in CH_2Cl_2. The UV-vis absorption spectrum was recorded with Shimadzu UV-1700 spectrophotometer.

Electrochemiluminescence (ECL). Similar to the experimental setup in the spectroelectrochemistry, three electrodes electrochemical cell was built, the charge states of the Au_{130} nanoclusters are also controlled by electrolysis with WaveNano potentiostat (Pine Instrument). The emission was recorded with an Andor iDUS CCD camera.

7.3 Results and discussions

Steady-state UV-visible absorption and voltammetry features are shown in Figure 7.2, which serve as reference points for the following spectroelectrochemistry analysis. Four discrete absorption bands around 360 nm, 493 nm, 585 nm and 716 nm are resolved (by first derivative) from the absorption spectrum. Uniformly spaced QDL peaks (ΔE = 0.193 V) are separated by a 0.35 V gap toward more positive and negative potentials as shown in the differential pulse voltammograms (DPVs). The small gap is consistent with the earlier prediction of the transition from Au_{14x} (x varied from 0-7 in earlier literature) to Au_{130} size ranges.[121] The constant 59 mV potential difference between reduction and oxidation peaks in each pair of QDL peaks suggest facile and reversible core charging/discharging electron transfer (ET) activities. Therefore, the Au_{130} clusters at different core charge states have very good stability, allowing further spectroelectrochemical studies.

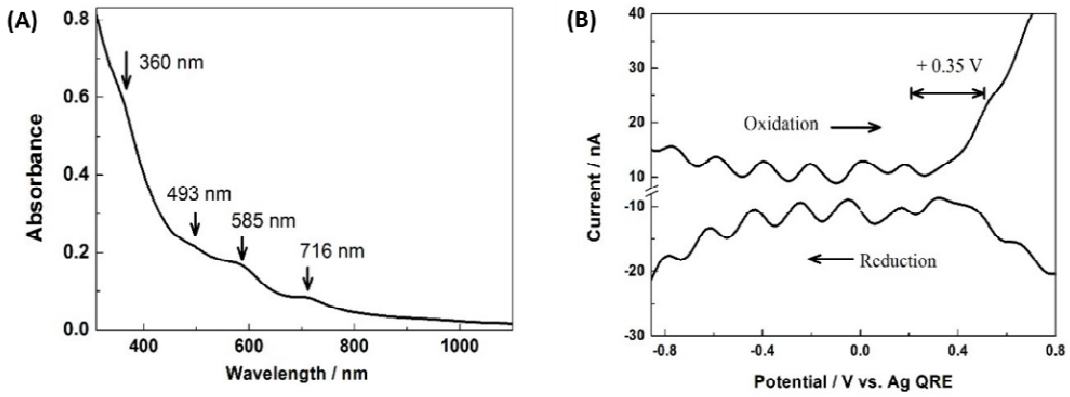

Figure 7.2 (A) The UV-vis absorption spectrum and (B) the differential pulse voltammograms (DPVs) of the Au_{130} nanoclusters in CH_2Cl_2.

The uniform spacing of the QDL peaks correspond to the charging energy of individual electrons transferred to the same energy states (inner Au core plus Au-S interface). A capacitance of C = e/ΔV = 0.76 aF is determined accordingly. Based on the concentric sphere model (C = 4pi εR(R+d)/d), and given the similarity in Au core sizes (R), the larger capacitance is attributed to the lower dielectric constant (ε) and thinner thickness (d) of the mono-layer arising from the aromatic ligand molecular structures (Durene-DT and PET). Another pair of peaks is separated by a ca. 0.35±0.01 V gap upon further oxidation around +0.40 V (panel B). Because the open circuit potential of the Au_{130} clusters is typically near 0 V, this pair of charging peaks in both oxidation and reduction scans reveal a discrete energy state that is 0.35 V below the degenerated frontier orbitals/states, i.e. HOMO, instead of a HOMO-LUMO gap. Regardless, this 0.35 V gap is another feature not observed from the well-studied $Au_{140\text{-}146}$ clusters in which the QDL peaks are relatively symmetric around frontier states. The large spacing can-not be explained by counter ion penetration (or polar solvent) into the ligand monolayer, which are known to increase the dielectric constant ε and thus decrease the charging energy.

At higher potential scan rates, the peak current in-creases while the peak positions remain largely unchanged, with ca. 59 mV peak separation between the forward and backward scans. The observations suggest diffusion-limited processes, or facile (electrochemical reversible) and chemically reversible ET processes. The overall ET features within this narrow potential range are reminiscent of the continuous QDL charging behavior observed for larger Au nanoclusters composed of 140 or more total Au atoms. The continuous energy states are supported by the similar inner core structures containing 105-Au atom in truncated-dodecahedral geometry re-solved recently through combined electron diffraction scanning TEM measurements and DFT calculations.

7.3.1 Oxidation of ligands and induced reversal reductions

At higher potential amplitudes, ca. + 1.34 V, large anionic peaks were recorded at different scan rates shown in Figure 7.3. Because this oxidation process is not observed from other Au-thiolate clusters especially those with PET ligands, simple dissociative oxidation at Au-S bonding interface is ruled out. The multi-electron oxidation processes have been attributed to the radical formation involving Durene-DT ligands. The Durene-DT is very different from monothiols such as PET. The oxidation peak at +1.34 V displays characteristics of facile ET followed by a chemical reaction at lower scan rates. Note the current is already divided by the square root of the scan rates ($\upsilon^{1/2}$) to normalize the diffusion contribution. The peak potential is insensitive to scan rates while the peak shape is non-broadened and can be fitted by one-electron kinetics, which sug-gest multiple electrons transferred to individual non-interacting orbitals.

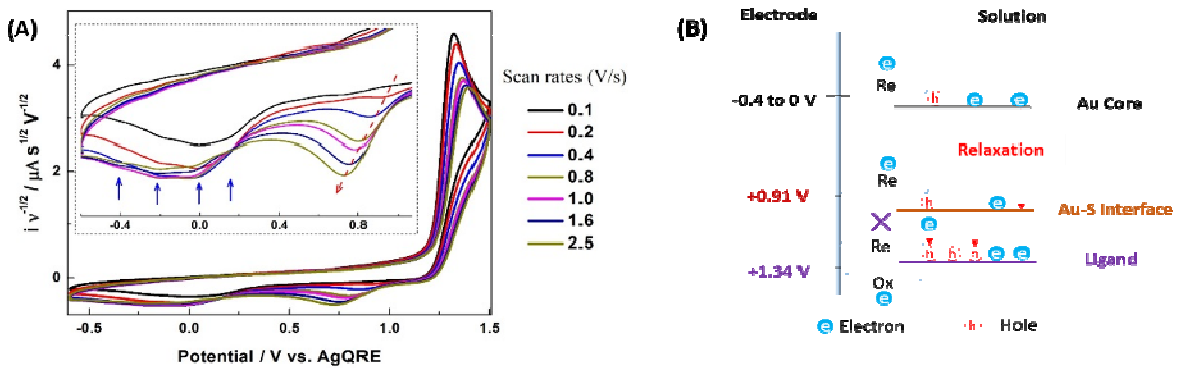

Figure 7.3 (A): CVs including Durene-DT ligand oxidation under different scan rates from 0.1 to 2.5 V/s. Arrows in the inset indicate the increase in scan rates. Electron relaxation processes are proposed in the panel (B), the electrons from the Au core and Au-S interface can relax into the empty ligands orbitals once the ligands are oxidized.

Next I focus on those reduction features only observable after the ligand is oxidized. At lower scan rates (panel A inset), additional reduction currents were captured at drastically shifted and broad reduction potentials (-0.4 to 0 V), arising around 0 V and approached a plateau around -0.4 V. The significant decrease in current amplitude compared to the +1.34 V oxidation can be explained by the mass transport loss and possible chemical/structural changes of the oxidized products when scanned to those potentials. Another discrete reduction peak around +0.9 V becomes more prominent at higher scan rates. The +0.9 V peak shifts toward less positive, suggesting a diffusive quasi to irreversible ET process. Interestingly, relative to the increase in the +0.9 V peak current at higher scan rates, the broad reduction features at -0.4 to 0 V become less defined and diminish into baseline current. The +0.9V peak becomes distinguishable at 0.4 V/s scan rate, which suggest a lifetime of up to 2 s of the corresponding species.

Taken together, I propose an electron relaxation mechanism illustrated in panel B. Because I am studying dynamic ET processes, the two electrons constitute the Au-S bonding should not be considered the same as those delocalized in Au core energy states. After the oxidation at +1.34

V, those created non-interacting empty ligand orbitals are filled by the delocalized electrons in the Au_{130} core and those involved in Au-S bonding energy states, -0.4 to 0 V and +0.9 V respectively. The two relaxation processes clearly display different time constants. Under fast potential scan rates in CVs, multiple electron reduction process can be detected at a non-spread potential around +0.91 V. The reduction by electrode fills those non-interacting Au-S bonding orbitals after the initial electrons relax into the vacant + 1.34 V states. If the reversal reductions were captured at a larger time scale, such as slow potential scan rates, the +0.9 V reduction peak disappears while reduction at potential ranges around -0.4 to 0 V becomes more prominent. This clearly suggests that the electrons in the Au130 core (-0.4 to 0 V) will also gradually relax into and fill the Au-S interface orbitals (+0.9 V), therefore no reduction peaks can be observed at +0.9 V with scan rates lower than 0.4 V/s.

Next, to better resolve those electron coupling/relaxation activities, normal pulse voltammetry (NPV) was employed with the results shown in Figure 7.4. In NPV, the applied potential is stepped from an unchanged initial potential to sequentially-changed final potentials. The current difference under the two potentials at specific time scale is recorded as one data point at the stepped potential. The technique therefore allows us to maintain consistent initial conditions at the electrode surface to capture different decay or relaxation processes at a certain potential.

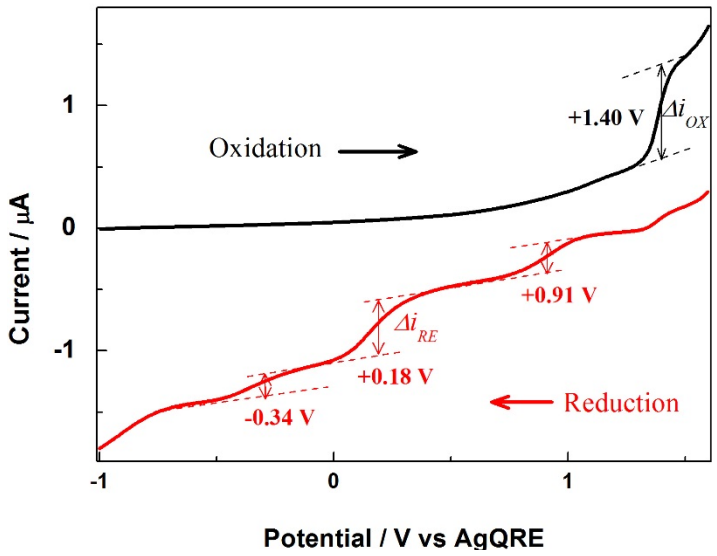

Figure 7.4 Normal Pulse Voltammograms (NPVs) of Au_{130} nanoclusters in CH_2Cl_2 with 0.1 M TBAP. The measurement parameters are: 0.05 V pulse width, 16.7 ms sample width, 0.2 s pulse period, 4 mV potential increment. Three distinct peaks, +0.91, +0.18 and -0.34 V are observed in the reduction process. The sample width (16.7 ms) corresponds to high scan rates in the CV measurements so that the oxidation potential (+ 1.40 V) is slightly larger than +1.34 V as observed in CVs.

The reduction curve in the NPVs was collected at an initial potential of +1.60 V, sufficiently more positive than the +1.34 V to replenish the oxidized species within the diffuse layer at each potential step. Three main reduction processes centered at +0.91 V, +0.18 V and -0.34 V can be resolved. Based on the current ratio ($\Delta i_{Red}/\Delta i_{Ox}$) at each reduction potential with respect to the oxidation current, about 37%, 53% and 18 % of the total oxidation products are reduced at those three potentials respectively. It is worth mentioning that a weak shoulder around +0.9 exists in the oxidation scans in both CVs and NPVs. With current recorded at 0.0167 s after each potential step, the loss of oxidation products is obviously less significant compared to CVs. It is interesting to notice that the total reduction current (from +1.0 V to -0.8/-0.4 V) matches nicely with the total oxidation current (+ 1.40 V).

With the three distinct reduction processes at -0.34, +0.18 and +0.91 V resolved by NPVs, potential step chronoamperometry was performed to capture the transient relaxation processes. After applying +1.6 V for 2 s to produce reproducible amount of oxidized products, the potential was stepped to -0.5, 0.0, and +0.7 V respectively (a small over potential was added in each measurement to ensure the current responses are determined by the diffusion process rather than electrode kinetics). Figure 7.5 shows those i-t and i-$t^{-1/2}$ curves at different potentials. For pure diffusion-limited responses, a linear relation-ship is expected in the i-$t^{-1/2}$ curve, in which the number of transferred electrons can be determined from the slope based on the Cottrell equation. A step to + 0.7 V will measure electrons needed to fill those vacant orbitals accessible, i.e. the + 0.91 V ones. At -0.5 V, the current will include all three reduction processes. An important observation in Figure 7.5 is that, at larger time scale (1 to 2 s), the slope at 0.7 V decreases more significantly com-pared to the slope/curvature at -0.5 and 0 V, suggesting the +0.9 V states becoming inaccessible, already filled by a slower relaxation process from orbitals with higher energy states (-0.4 to 0 V) to +0.9 V orbitals.

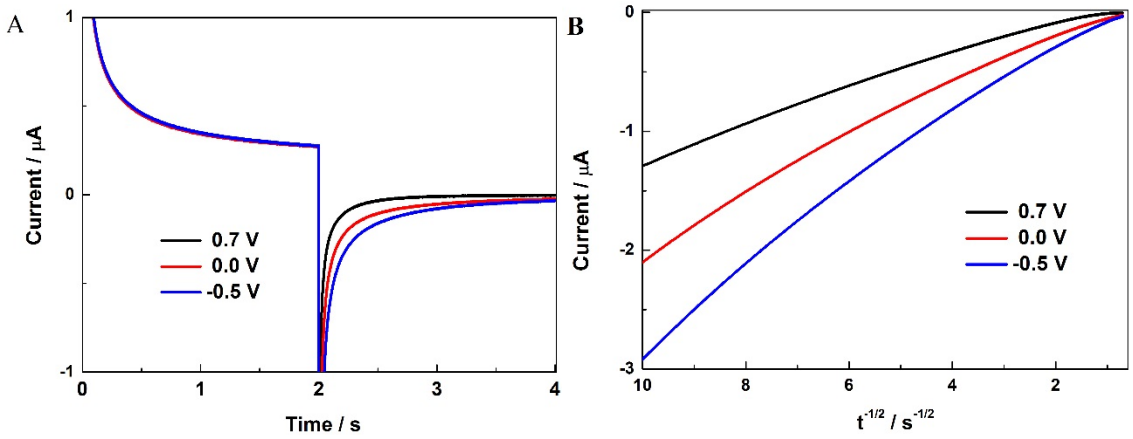

Figure 7.5 (A): Potential-step current-time curves from the same initial +1.60 V (0-2 seconds) to different end potentials 0.7, 0.0 and -0.5 V (2-4 s). (B): Cottrell plots of the reversal reducitons from 0.01 to 2 s respectively. Data below 10 ms was not included due to the charging effect (RC time constant is ca. 2-3 ms).The sampling interval is 0.1 ms.

Data analysis and linear fitting of the Cottrell curves at different time periods are detailed in Figure 7.6. Within 0.01 to 0.05 s, more than 97 % of those oxidized species was reduced at -0.5 V. This impressive number suggests almost full recovery or chemical reversibility. Among this 97%, 46% was captured at the + 0.7 V reduction, which leave 25% to the 0.0 V reduction and another 26% to the -0.5 V reduction. In other words, about 50% of the vacant orbitals by the + 1.34 V oxidation is filled within 10 ms by the electron relaxation from + 0.9 V states, 25% by those from + 0.18 V states, and another 25% by the -0.34 V states. At longer time, possible processes such as core structural changes, radical reactions involving durene-DT as well as mass transport loss cause the slope to further decrease in all three curves. Normalized by the slope of the -0.5 V curve under the assumption of it accounts for the total oxidized states/species still accessible by the electrode, the slope of the +0.7 V curve decreases to 44% (36%/82%) within 0.2-0.4 s and 14% (8/58%) within 1-2 s respectively. Because other possible losses have been normalized, the decrease accounts for the electrons relaxed from higher energy states, i.e. frontier states around +0.18 V and -0.34 V. The difference in the 0.0 V and -0.5 V curvatures is minimal over different time scale, probably corresponding to broad frontier states whose degeneracy could be changed during these processes that requires further analysis. Apparently, the electron relaxation from those frontier states into the +0.9 V states is gradual with a lifetime about 2 s, which agrees well with the scan rate CV analysis. Further, the electron relaxation occurs at a single potential (CA and NPV), which is consistent with the non-broadened +0.9 V peak shape in CV, attesting the assignments of relaxation into non-interacting states, i.e. those localized as Au-S-Durene bonding. It is unclear at this point if those states also involve the rest Durene-DT ligand molecular structures or solely the Au-S bonding.

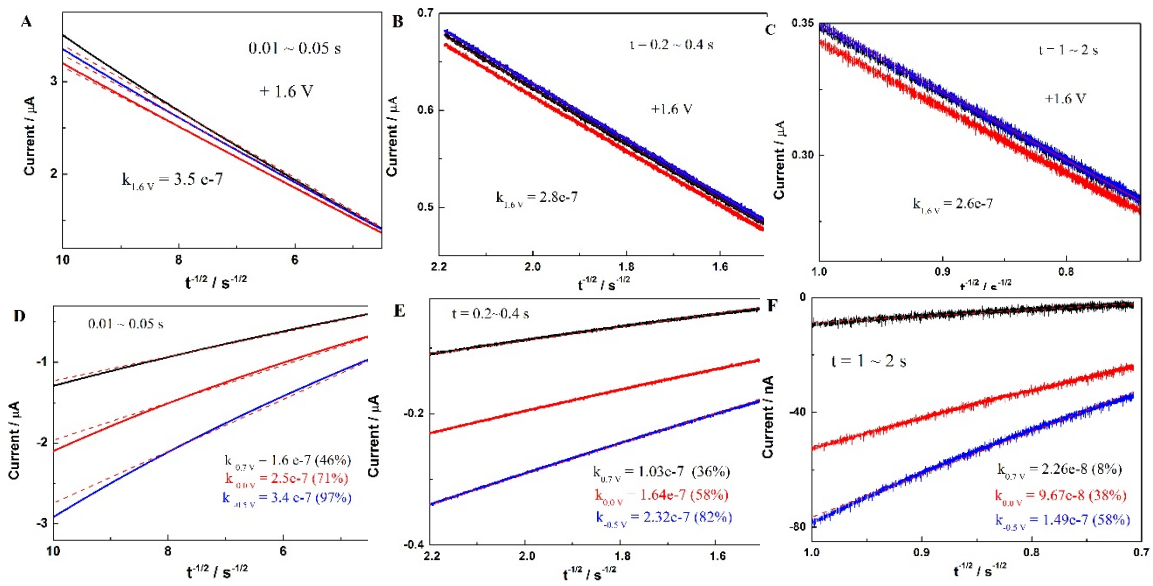

Figure 7.6 Chronoampermetry analysis of the ligand oxidation (+1.6 V) and three reversal reduction processes (-0.5, 0 and 0.7 V) at different time scales. The i- $t^{-1/2}$ curves for ligand oxidation at +1.6 V at short and long time duration are shown in panel A(0.01 to 0.05 s) B (0.2 to 0.4 s) and C(1 to 2 s), while i-$t^{-1/2}$ curves for the three reversal reduction process are shown in panel D(0.01 to 0.05 s) E (0.2 to 0.4 s) and F (1 to 2 s). Solid lines are from experiments and the dash lines from fitting. The slopes of those linear curves at the representative time periods are listed. From the ratio of the reduction curve slopes with respect to the oxidation ones, the percentage of electron transfer numbers at each potential, or energy states, are obtained. From Panel A and D: 46%; 71%-46%=25%; 97%-71%=26%. From Panel B and E: 36%; 58%-36%=22%; 82%-58%=24%. From Panel C and F: 8%; 38%-8%=30%; 58%-38%=20%.

Quantification of ETs. It is nontrivial to quantify the number of ET due to the time-dependent relaxation. The results from multiple electroanalytical techniques are discussed next. The number of ETs corresponding to ligand oxidation is quantified first. For a diffusion limited facile ET process,

$$i_p = (2.69\times10^5) n^{3/2} A D_0^{1/2} C_0 \upsilon^{1/2} \qquad \text{(Eq 8.1)}$$

i_p: peak current, n: # of electrons transferred, A: area of working electrode, D_0: diffusion coefficient, C_0: concentration, and v: scan rate.

For multiple electrons transferred to non-interacting redox centers (molecular orbitals), the peak shape remains while the peak current is directly proportional to the number of electrons instead of $n^{3/2}$. Shown in Figure 7.7, the oxidation current of one QDL peak at -0.35 V and that of the ligands at +1.34 V is largely linear with square root scan rate, confirming diffusion limited facile ET activities. Because *A, D_0* and *C_0* are the same, using the well-defined single electron transfer QDL peaks as the reference, the ET number at +1.34 V is calculated to be ~58. While the absolute number of ligand oxidation varies by few from different batches of Au_{130} samples (29 per cluster on average), the results suggest that about two electrons per Durene-DT ligands are oxidized in those ET processes, behaving as redox labels.

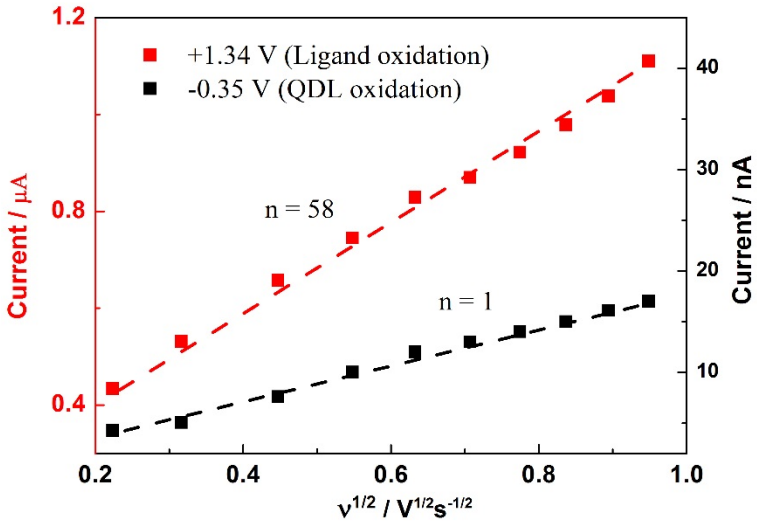

Figure 7.7 The peak currents vs square root scan rate and their corresponding fitting of the QDL and ligand oxidation peaks at -0.35 and +1.34 V, data are obtained from Figure 7.3.

Potential-step chronoamperometry analysis, shown in Figure 7.5 and 7.6, offers better quantitative analysis of the reversal reduction processes at different time scale. For example, within 0.01 to 0.05 s, after 59 e are transferred out from the ligand orbitals at +1.34 V , 27 e from the

+0.9 V states will relax into the vacant ligand orbitals, with the rest 30-31 e being filled by the relaxation from the core electrons (i.e. 15 e from -0.34V and another 15 e from +0.18 V). At longer time up to 2 s, 34 e of the 58 e can be reduced directly at -0.4 V. The 34 e includes 5 e to the +0.9 V, 17 e to the +0.18 V and 12 e to the -0.34 V states. The relative decrease of the +0.9 V reduction with respect to the core energy states reflects those electrons relaxed into lower energy states. The loss of total electrons, 34 out of 58, might be limited by electrokinetic and mass transport loss. Because the main optical absorption peaks and electrochemical peaks remain largely unchanged after repeated CV scans including ligand oxidation (hundreds cycles), possible irreversible processes, such as oxidative stripping of Durene-DT ligands or radical chemical reactions, are believed insignificant, at least at scan rates higher than 0.5 V/s.

The above analysis is also consistent with the CV features of two linear regions at low and high scan rate ranges, with transitions at middle scan rate range, as shown in Figure 7.8. Because CV analysis is relative slow compared to the amperometric analysis and the baseline is greatly affected by the charging currents, only 8 electrons were resolved in the data presented. Regard-less, the complement slopes suggest the electron relaxation from the core to Au-S interface states as time progresses (slower scan rates, toward left).

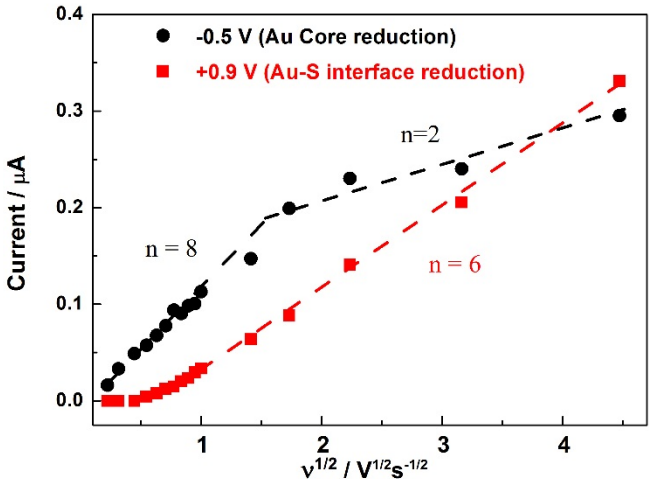

Figure 7.8 Peak current analysis of the reversal reduction peaks at +0.9 and -0.5 V in CVs at different scan rates (Data are from Figure 2, from 0.1 to 20 V/s). Different linear regions at low and high scan rate ranges for the -0.5 and +0.9 V peaks are displayed, indicating different relaxation time scales.

Temperature dependent relaxation. Next I will present the preliminary studies at lower temperature (195 K) of the ligand oxidation and reversal reduction processes to gain further insights and support of the proposed relaxation process. Systematic studies will be reported later for kinetic and thermodynamic discussions. The CV results normalized by the $\upsilon^{1/2}$ are shown in Figure 7.9. The oxidation process of the Durene-DT ligand is less reversible compared to that under room temperature, as the oxidation peak potential shifts more positive with the increase in scan rates. In addition to the slower ET kinetics, because the diffusion coefficient decreases at lower temperature, the ligands accessible for ET reactions at the electrode are more restrained by the limited rotational diffusion. Accordingly, only 20 electrons were transferred in the oxidation process based on the peak current ratio over QDL peaks. Compared to the RT behavior, the reversal Au-S reduction at + 0.8 V appears to be more dominant even at very slow scan rates. Additional reduction current around the frontier states, from +0.4 to -0.4 V, is still detectable (in

reference to the oxidation current within the same range corresponding to QDL charging), but less significant compared to RT results. The distorted reversal reduction peaks are indicative of the electronic coupling between the core and ligand energy states, which refute irreversible chemical reactions such as ligand stripping: an increase in QDL peak current would not be expected. Overall, the decrease in the electronic coupling/relaxation at low temperature, particularly those from the core frontier states, suggest high possibility of core structure changes or reversible radical chemical transformation during the slow relaxation.

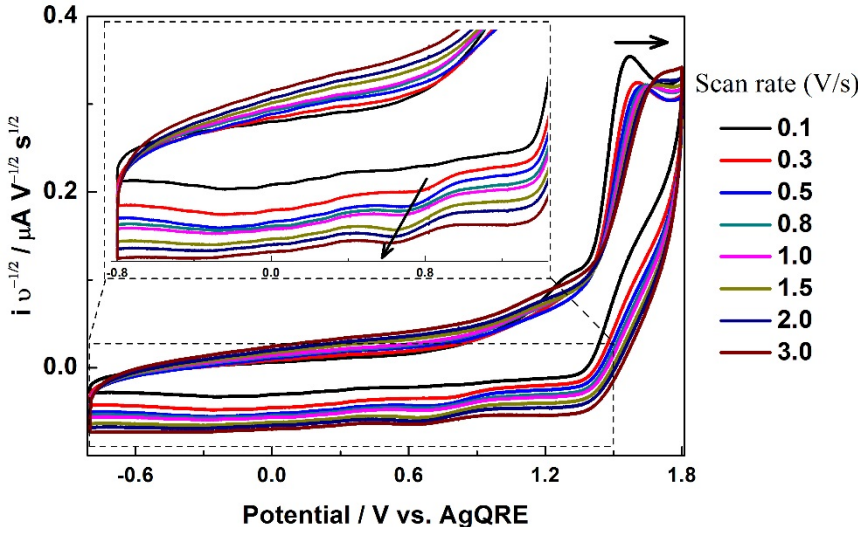

Figure 7.9 CVs of the Au_{130} nanoclusters at low temperature (195 K) in CH_2Cl_2 with 0.1 M TBAP as supporting electrolyte. Data were collected in dry ice/ethanol bath.

Last but not least, plasmonic Au nanoparticles with 3 nm core diameter stabilized by durene-DT ligands were tested. Similar voltammetric features were observed as shown in Figure 7.10. Compared to Au_{130}, the ligands are oxidized at +1.23 V rather than at +1.34 V. Reversal reduction processes, also observed only following ligand oxidation, are shifted to +0.75 V and 0.27 V respectively. The less positive potentials suggest a stronger stabilization of the oxidized species

by the larger core. Because single QDL peaks could not be resolved from large plasmonic nanoparticles due to the small charging energy, the charges in the oxidation and reduction scans were compared. In both cases of without ligand ETs in a small potential window and with ligand ETs, the integrated areas as shown in panel C, or charges, compensate in the respective oxidation and reduction scans. The observed multi-ET processes and the shifts in the redox potentials from a different sized Au core provide further evidence of the coupling between the ligand and core energy states.

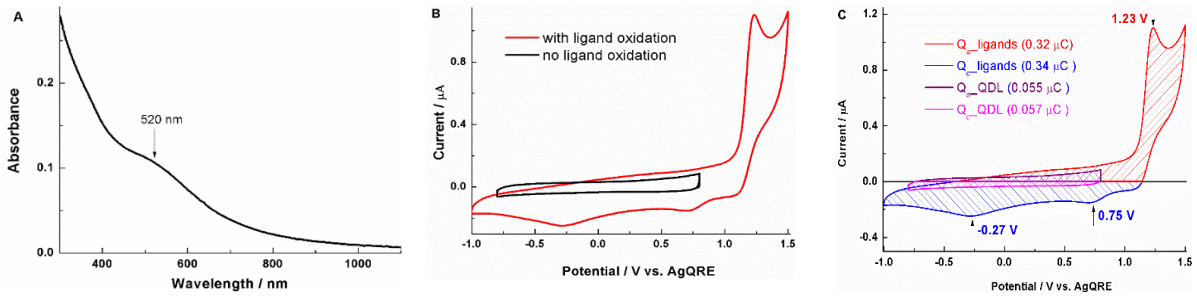

Figure 7.10 (A)**:** The UV-vis absorption spectrum, (B) cyclic voltammograms of large Au-Durene-DT nanoclusters at two different potential windows with 0.1 M TBAP as supporting electrolyte in CH_2Cl_2, and (C) the charge analysis for the QDL and ligand oxidation regions.

7.3.2 Spectroelectrochemistry of Au_{130} nanoclusters

Spectroelectrochemistry combines the merits of optical and electrochemical techniques: the core and ligands redox states can be actively controlled via electrochemistry; the absorbance at different charge states can be recorded after electrolysis; the energy states of those corresponding electronic transitions can be correlated accordingly. This report studies a large Au_{130} cluster with some ligands that can be electrochemically activated. Spectroelectrochemistry is shown as a readily accessible technique to conveniently provide new fundamental insights for metal clusters. Such knowledge in literature remains scarce and is mainly obtained by ultrafast transient

absorption spectroscopy. The later tool offers lifetime in addition to the detailed electronic transitions but requires more advanced instrumentation and thus with less accessibility.

Briefly, a three-electrode electrochemical cell was built in an asymmetric quartz cuvette (0.1×1 cm), as shown in the inset of Figure 7.11. A large Pt mesh was used as a working electrode in the light path (0.1 cm). A Pt foil as the counter electrode and an Ag wire as the quasi-reference electrode (QRE) were positioned away from the light path. The thin layer and relative low sample concentration enable fast electrolysis within minutes. The majority Au_{130} clusters in the light path can be charged to the desired charge states, monitored by the current decay to ca. 10% of initial value at a given potential. An absorption spectrum is recorded after each electrolysis. Due to the ligand oxidation process being irreversible, the absorbance spectra under +1.5 V (Dur-DT ligand oxidation) is taken after 1-2 min electrolysis.

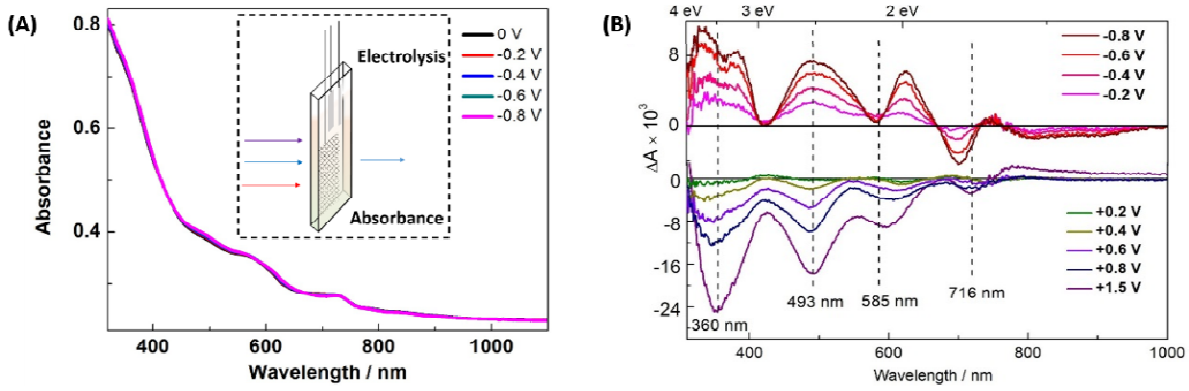

Figure 7.11 (A) The absorption spectra under different electrolysis potentials and the experimental setup was shown as an inset. To better illustrate the changes in the spectra, the differential absorption spectra was plotted with respect to the 0 V, as shown in (B).

The original and differential absorption spectra at different electrolysis potentials are included in Figure 7.11 and differential spectra were obtained by subtracting the spectrum at 0 V. The

four main peaks from the original sample are indicated by the dash lines among those rich transitions newly-resolved. In panel B, the absorption bands around 3.5 eV, 2.5 eV and 2 eV intensify upon further reduction of Au core. Negative ΔA is observed showing a valley at 1.77 eV and a broad decrease from 1.66 to 1.26 eV. Interestingly, the 585 nm peak is one of the zones (another two around 2.90 eV & 1.66 eV) that remain largely unchanged. A well-defined isosbestic point at 1.85 eV suggests the conversion between the 1.99 eV peak and the 1.77 eV valley (sum at 3.76 eV). In the core oxidation (+0.2 to +0.8 V), the intensity at all four peaks decreases. A notable feature is the shift in the peak position from ca. 2 eV in reduction panel toward the 585 nm band upon oxidation. In addition to those decreased bands, upon the ligand oxidation at +1.5 V, the intensity increases broadly below 1.66 eV.

The spectra after reduction electrolysis clearly display two components in the 360 and 493 nm absorption bands. Gaussian fittings of the differential spectrum at -0.8 V are shown in Figure 7.12. The 360 nm band is deconvoluted into two peaks centered at 335 nm and 380 nm (3.70 and 3.26 eV), while the 493 nm band into 478 nm and 526 nm (2.59 and 2.35 eV). It appears that the 3.26 eV peak remains in position while the 3.70 eV peak shifts toward the 360 nm band when further oxidized. While the plasmonic band for few-nanometer Au nanoparticles (at 520 nm, 2.38 eV) is not discernable for most Au clusters, it is intriguing to observe the emergence of a 2.35 eV band upon reduction.

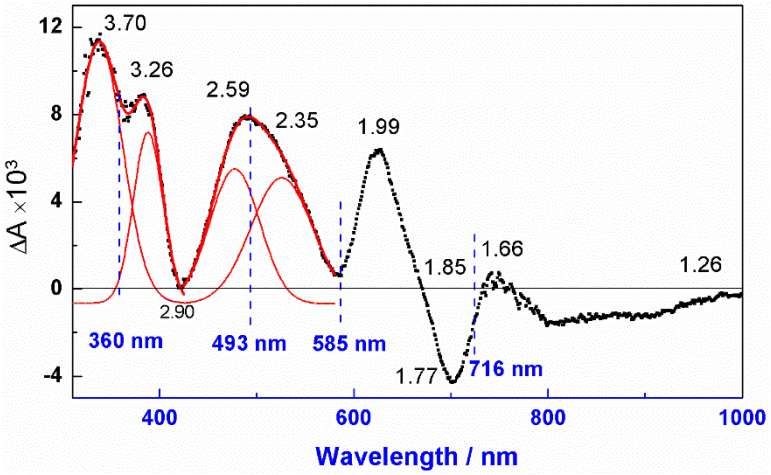

Figure 7.12 The Gaussian fittings (dash lines) for the 360 and 493 nm band in the differential absorption curve at -0.8 V. Four peaks centered at 335, 380, 478 and 526 nm are deconvoluted.

7.3.3 Energy diagram of the Au_{130}

The electrochemical potentials for the metal core, ligands and Au-S interface were investigated before the energy diagram is established. At higher potentials, ET activities involving thiolate ligands could occur. Irreversible ET processes accessing to ligand and Au(x)-ligand orbitals are observed in the CVs at wider potential window shown in Figure 7.13. Specific to the durene-dithiolate ligands, a prominent oxidation peak at ca. +1.32 V and a reduction at ca. -2.06 V are found for the Au_{130} clusters. The CVs from a 2:1 Au:Dur-DT complex and a 1:1 Au:Dur-DT complex are also provided for comparison. These complexes, known to be oligo/polymeric mixtures in general as intermediates when synthesizing Au clusters, could be perceived as Au(I)ish and as Au(II)ish respectively, considering each Dur-DT has two -SH groups and their possible bond motifs on Au core surfaces as ligands. The ET potential (peak or half wave $E_{1/2}$) of thiolate ligands on nanosized gold core, such as oxidative and reductive desorption, are slightly shifted from those observed from the Au(X) complexes and those on flat Au surface, i.e. self-assembled monolayer that has been widely-studied.

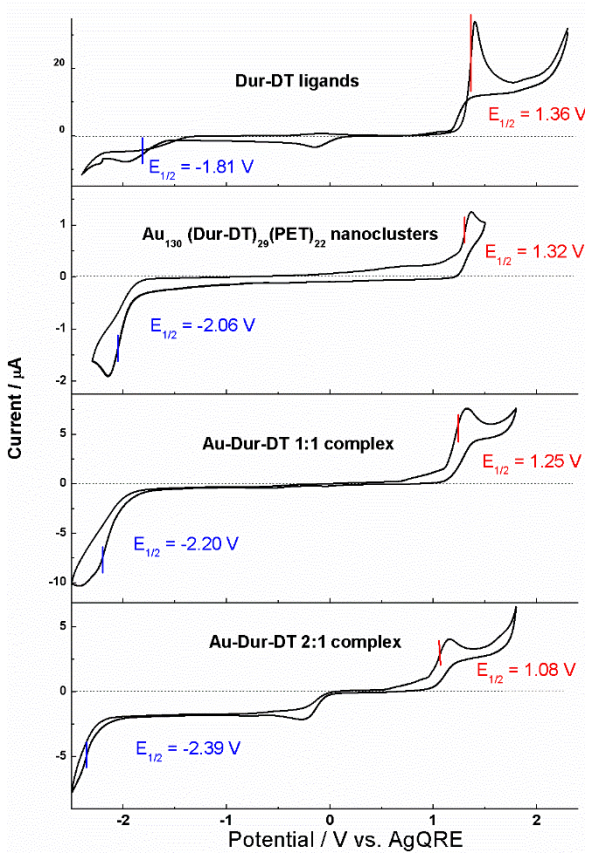

Figure 7.13 The electrochemical features of the Dur-DT ligands, Au_{130} nanoclusters, and 1:1 and 2:1 Au-Dur-DT complexes. The CV of Dur-DT ligands was collected in CH_3CN, while the Au_{130} nanoclusters and Au-Dur-DT complexes with two different ratios, 1:1 and 2:1 were measured in mixed toluene/CH_3CN (2:1, v/v) due to solubility limit. All solutions had 0.1 M TBAP as supporting electrolyte. As shown, most ET processes are irreversible presumably due to adsorption-desorption of extra thiol/thiolates on the Pt electrode. Regardless, the ligand redox potentials are relatively consistent in both complexes and nanoclusters, with small shifted $E_{1/2}$ values. These $E_{1/2}$ shift is employed as the boundary extreme for different possible Au-S interfacial bonding structures. For the Au-Dur-DT 2:1 complex, additional reduction peak near 0 V indicate a different Au-S interfacial bonding structure compared to 1:1 ratio complex. The charge states of Au in the 2:1 ratio is slightly positive than the Au in 1:1 ratio.

Before an energy diagram is proposed to attribute the corresponding transitions, an important concept about the electrochemical features at different charge states is explained in Figure 7.14. After each electrolysis, the majority clusters in the bulk solution have been con-

verted into the products of the corresponding ET reactions. It is obvious that the QDL peaks, still with uniform peak spacing in each voltammogram, are stretched or compressed upon the charging to the respective potentials as shown in panel A. Extra charges on the Au core will require counter ions to maintain charge neutrality in solution. Both core charges at the core-ligand interface beneath the ligand monolayer) and counter ion penetration (into the monolayer from outside) are known to decrease the capacitance, which leads to the increase in charging energy, i.e. peak spacing ΔE. Accordingly, the ligand oxidation potential is also shifted as shown in panel B. This change in QDL peak spacing, though small at ca. 10 mV range as analyzed in panel C, indicates the coupling between the core and peripheral charges (or dipoles). The QDL spacing at each electrolysis potential are averaged of all the peak distances. Such interaction at the core-ligand interface is expected to be dynamic, which adds complexity reflected in the proposed energy diagram.

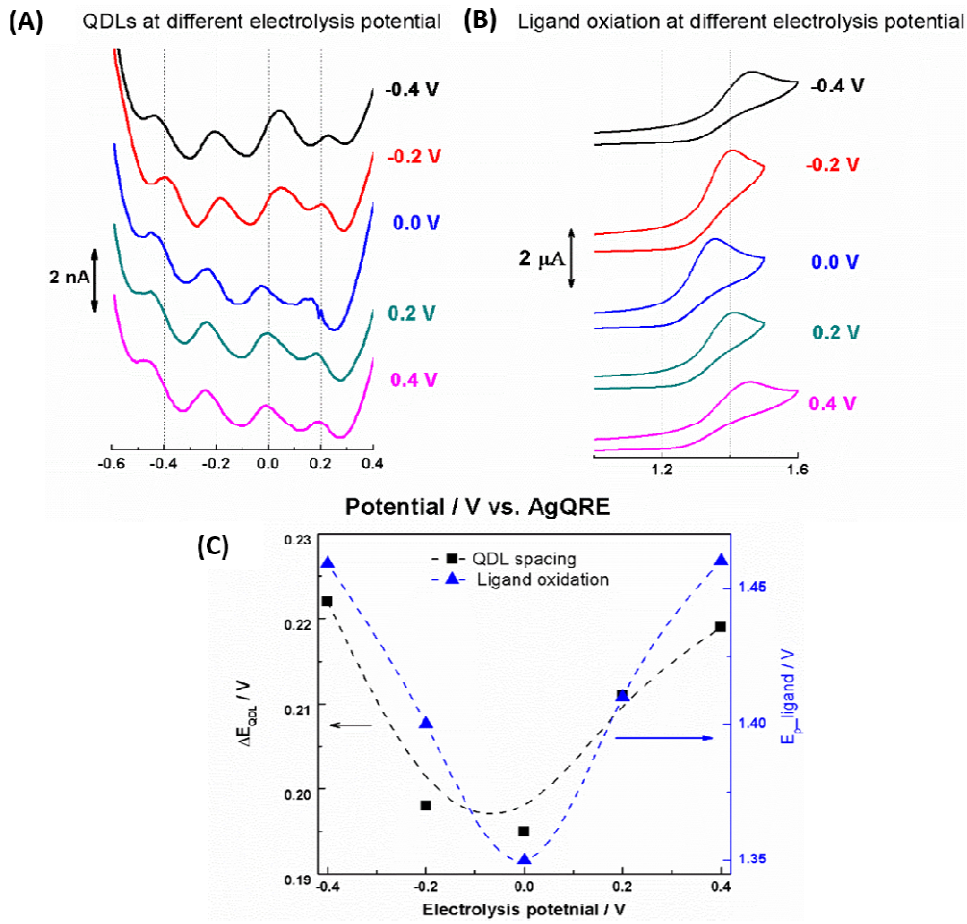

Figure 7.14 (A) The QDL peaks resolved from the DPVs; (B) the irreversible ligand oxidation from the CVs and (C) data analysis after bulk electrolysis at different potentials (or different core charge states). Dash lines in panel c are added to show the trend (not fitting).

The energy diagrams of the native Au_{130} clusters and those after reduction are proposed in Figure 7.15. Those energy states involved in the distinct absorption transitions are sketched. The diagram of the oxidized form is relatively straightforward to explain and thus not plotted separately. The open-circuit potential (or rest potential) is slightly positive for as synthesized Au_{130} clusters, i.e. +0.18 V for this sample, which is used to define the core frontier states. The 0.35 V gap after two-electron oxidation from 0 V (Figure 7.2) suggests that there is an energy state immediately below the core frontier states (0.35 - ΔE + 0.18 = 0.34 eV, ΔE is the charging energy, 0.19 V). In consideration of the one-charge differences of the Au clusters in the diffuse

layer after ET reactions, and possible heterogeneity of the Au clusters (both charge states and composition), ΔE is added into these two states as possible band boundaries (error bar).

At +1.32 V and -2.06 V, ET activities reveal the Au-Dur-DT HOMO and LUMO states. For monothiolate Au clusters, the Au atom in the staple motif (RS-Au-SR) is slightly more positive than Au(I) complexes. Because the bond structures of the dithiolate Dur-DT on Au clusters are currently unknown albeit inner Au core structures are determined,[122] the corresponding redox potentials of the two Au-Dur-DT complexes are employed to define the range of the HOMO and LUMO states respectively. Absorption transitions to the Au-Dur-DT LUMO could therefore involve the -2.06 V states observed from the Au_{130} clusters, and possibly -2.20 V and -2.39 V ones at different time scale that will require transient absorption measurements beyond the scope of this report. It is important emphasizing that due to the chemically irreversible desorption of thiolates, the listed potential values ($E_{1/2}$) could involve several processes spanning over a potential range rather than a specific value. A weak oxidation band at around +0.9 V can be resolved as previously reported.[123] The transition from this state to higher energy states, i.e. core frontier states, could not be detected with the spectrometer employed. This state is not included in the diagram for clarity. The oxidation peak around +1.73 V is denoted as Au-S HOMO-1, from either the Au-PET bonding or one of the two sulfurs on Dur-DT that bonds to Au similar to the monothiols, or both.

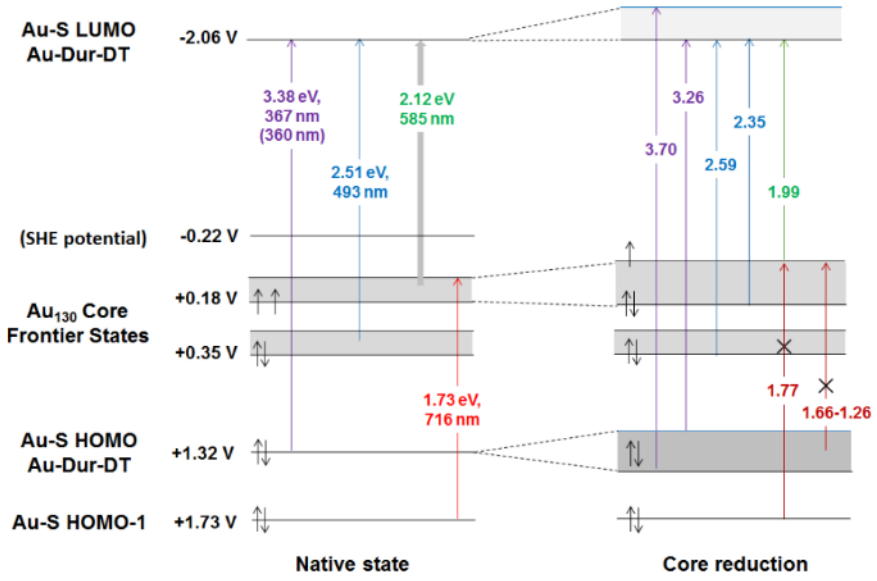

Figure 7.15 The proposed energy diagram for the Au_{130} nanoclusters at native, and reduction states. Some involved energy states would be split and shifted when the core are reduced. The arrows indicate the transferred electrons during the core oxidation/reduction processes. As all the potential values are measured with respect to the AgQRE (0.22 V vs. SHE), the SHE potential is thus included in the diagram as -0.22 V.

For the as-synthesized Au clusters, i.e. native state on the left, all four main absorption bands can be assigned with the transitions between these energy states very well. The 360 nm (3.44 eV) band is also observed from the two Au-Dur-DT complexes, and thus arises from the Au-Dur-DT HOMO-LUMO transitions. The minor differences from the electrochemistry states (1.32 + 2.06 = 3.38 vs. 3.44) is attributed to the broad potential range, particularly from the chemically irreversible reduction process. Considering the reduction of the two complexes at -2.20 V and -2.39 V respectively, a ca. -2.12 V state in the midst of this broad band would give almost perfect assignment. Similarly, the 493 (2.51 eV) and 585 nm (2.12 eV) bands are attributed to the transitions from the core frontier states to the Au-Dur-DT LUMO. The transition from the Au-S HOMO-1 state to the partially-filled core frontier states leads to the weak band around 716 nm

(1.73 eV). This assignment also explains and is supported by the weak band observed around 700 nm from different Au_{130}-Au_{144} clusters.[124-126] The minor peak shift reflects the differences in the core energy states of those clusters presumably. The transitions from the Au-Dur-DT HOMO to core frontier states would constitute the diminishing yet-non-zero absorbance extending beyond the detection range (1100 nm). Furthermore, transition from the +0.34 V states to the upper edge of the frontier states would generate the expected optical gap that could not be directly measured herein.

Oxidation or reduction processes will change the electron density of the Au clusters. The excess electrons or holes are expected to reside/delocalized at the core-ligand interface. The splitting and shifting of the peak wavelength reveal the corresponding shifted or split energy states at the interfacial Au-S bonding. The rationale further validates the proposed energy diagram retrospectively elaborated next. In the reduction diagram, additional electrons into the core frontier states will inhibit the excitation from the lower states, which explains the broad decrease at the 1.66 to 1.26 eV range (rightest arrow). Consequently, the excitation to the Au-Dur-DT LUMO state will intensify. Further, the excess electrons is speculated to shift the density of states corresponding to Au (II)ish toward Au(I)ish type bonding at the core-ligand interface. Using the -2.06 V and -2.39 V as boundaries, the 3.70 eV and 3.26 eV transitions are aligned almost perfectly. The argument requires finite structure information of the core-ligand bonding that is not available currently. Time resolved transitions could reveal the corresponding time constant that is not accessible in this study. The excess electrons appear to change the degeneracy of the frontier states and lift the upper edge slightly. This is attested by the well-defined isosbestic point at 1.85 eV that separates the new 1.99 eV peak and the 1.77 eV valley (a total

of 3.76 eV that matches the Au-S HOMO to LUMO transitions!). It is worth mentioning that both transitions are only observed in the differential spectrum by spectroelectrochemistry. The two areas match each other well, which strongly suggest the conversion between an enhancement and an inhibition of the respective transitions. Similarly, those additional electrons in the listed core states account for the enhancement and peak splitting of 493 nm band. Other possible transitions between those states are not elaborated one by one, as they either remain un- or less changed compared to not-electrolyzed samples (i.e. 585 nm band) or do not generate detectable signals (beyond detection range).

The lower electron density upon further oxidation causes the decrease of all four absorption bands in general. It is obvious that the 493 nm and 585 nm band will decrease due to the lower electron density. One likely cause for the 360 nm band decrease is strong coupling of the core energy states and the ligand orbitals at the core-ligand bonding. The newly created holes would reside at the Au-S interface and thus lower all corresponding transitions. Beside the decrease in intensity, the very important observation supporting the proposed diagram is the blue shift of the (-ΔA) valley at 1.99 eV toward the 585 nm absorption band and the corresponding red shift of the 1.77 eV (700 nm) valley toward the 716 nm absorption band. It is unknown if the absorbance at lower energy range, i.e. from +1.32 to +0.18 = 1.14 eV, would increase with more states accessible limited by the spectrometer detection range. Based on our earlier studies, electrons in the core energy states could relax into those emptied ligand orbitals after the cation radical formation upon ligand oxidation at +1.5 V.[123] Accordingly, the new feature in the +1.5 V oxidation spectrum, albeit incomplete electrolysis and non-steady-state, reveal a broad increase below 1.66 eV. The observation not just further prove the earlier concept in the coupling of elec-

trons in core states and Au-S ligand orbitals, but also justifies the inclusion of broad Au-Dur-DT energy states illustrated in the reduction panel corresponding to the 1.66-1.26 eV transitions.

7.3.4 Electrochemiluminescence (ECL) of Au_{130} nanoclusters

Based on the proposed energy diagram, two type of ECL patterns are observed from the Au_{130} nanoclusters when applying different potential forms.

Core charge annihilation. The well-defined and reversible QDL peaks of Au nanocluster suggest that the Au core can serve as both electron donor and acceptor, and their product is relatively stable. Therefore annihilation ECL would display when generating Au nanoclusters with negative and positive core charges by stepping the potential from negative to positive. As shown in Figure 7.16, ECL peaks displays when switching the potential from -0.6 V and 0.6 V, the ECL mechanism was shown in panel B. The resulting ECL intensity is relatively low and its time scale is also short. More interestingly, the ECL patterns only shows when the cores are reduced first and then oxidized, not the other way (core oxidation first and the reduced), which probably suggest different core oxidation and reduction mechanism and lifetime of the products.

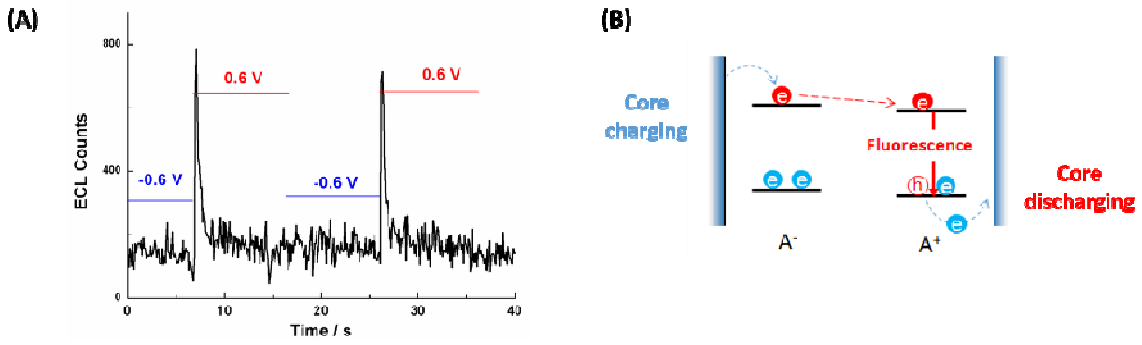

Figure 7.16 (A) The annihilation ECL from the Au_{130} nanocluster from core charging and discharging, and (B) shows the involving anihilation mechanism.

Au-S interface involving ECL. Another interesting ECL patterns have been obsrved when increasing the potential close and above 0.9 V (Au-S oxidation), as shown in Figure 7.17. An ECL

peak was displayed when applying 0.8 V, suggesting an electron relaxation processes from the Au core to the Au-S interface. Noting that only the core charging energy difference (0 to 0.8 V, or 1500 nm) would not result in lumilenscene that can be detected by the CCD camera (detection limit is around 1100 nm). When the Au-S interface are fully oxidzied at 1.0 V, as shown in panel B, a long time ECL was observed at 1.0 V and a huge emission peak was also displayed when switching the potential back to 0 V. The results further confirms the electron relaxation processes from the Au core to the Au-S interface, as the produced lumilescene was detected.

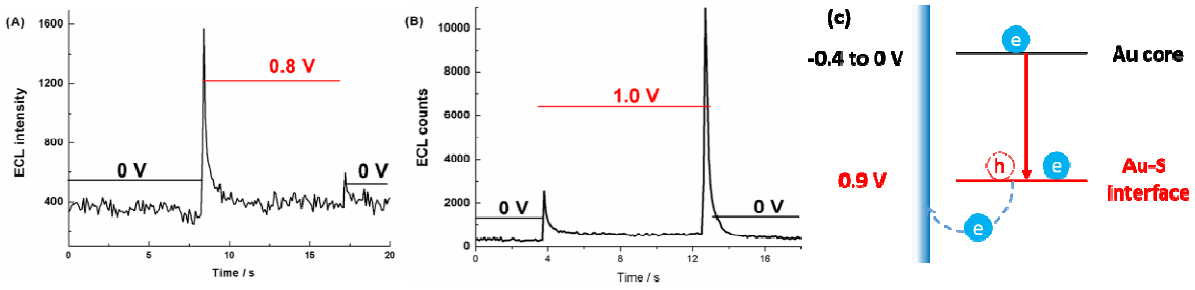

Figure 7.17 The Au-S interface oxidation invloved ECL. (A) An ECL peak was observed at 0.8 V, and (B) more ECL counts were observed in the when steping the potnential above 1.0 V, the ECL would come from the electron relaxation process from Au core to Au-S interface, as shown in panel C.

7.4 Conclusions

In this chapter, the electronic transitions in the thiolate protected Au_{130} nanoclusters are investigated via multiple electronic and optical techniques. The redox features of the Au core, ligands, and their interplay are investigated, and the strong energy coupling was observed between the core and ligand energy states, as revealed from the reduction peaks induced by the ligand oxidation. The energy diagram of this Au_{130} nanocluster have also been proposed based on the spectroelectrochemistry results, controlled electrolysis of the Au core reveal the corre-

sponding transition features observed in the UV-vis absorption spectrum. The electrochemiluminescence features of this Au_{130} nanoclusters are also investigated and two different type ECL patterns was attributed to the core charge annihilation and electron relaxation between the core and Au-S interface.

REFERENCES

(1) Daiguji, H., Ion Transport in Nanofluidic Channels. *Chem. Soc. Rev.* **2010,** *39*, 901-911.
(2) Hanggi, P.; Marchesoni, F., Artificial Brownian Motors: Controlling Transport on the Nanoscale. *Rev. Mod. Phys.* **2009,** *81*, 387-442.
(3) Schoch, R. B.; Han, J. Y.; Renaud, P., Transport Phenomena in Nanofluidics. *Rev. Mod. Phys.* **2008,** *80*, 839-883.
(4) Howorka, S.; Siwy, Z., Nanopore Analytics: Sensing of Single Molecules. *Chem. Soc. Rev.* **2009,** *38*, 2360-2384.
(5) Li, J. L.; Gershow, M.; Stein, D.; Brandin, E.; Golovchenko, J. A., DNA Molecules and Configurations in a Solid-State Nanopore Microscope. *Nat. Mater.* **2003,** *2*, 611-615.
(6) Vlassiouk, I.; Siwy, Z. S., Nanofluidic Diode. *Nano Lett.* **2007,** *7*, 552-556.
(7) Guo, W.; Cao, L. X.; Xia, J. C.; Nie, F. Q.; Ma, W.; Xue, J. M.; Song, Y. L.; Zhu, D. B.; Wang, Y. G.; Jiang, L., Energy Harvesting with Single-Ion-Selective Nanopores: A Concentration-Gradient-Driven Nanofluidic Power Source. *Adv. Funct. Mater.* **2010,** *20*, 1339-1344.
(8) Itoi, H.; Nishihara, H.; Kogure, T.; Kyotani, T., Three-Dimensionally Arrayed and Mutually Connected 1.2-Nm Nanopores for High-Performance Electric Double Layer Capacitor. *J. Am. Chem. Soc.* **2011,** *133*, 1165-1167.
(9) Nasir, S.; Ali, M.; Ensinger, W., Thermally Controlled Permeation of Ionic Molecules through Synthetic Nanopores Functionalized with Amine-Terminated Polymer Brushes. *Nanotechnology* **2012,** 225502.
(10) Wei, C.; Bard, A. J.; Feldberg, S. W., Current Rectification at Quartz Nanopipet Electrodes. *Anal. Chem.* **1997,** *69*, 4627-4633.
(11) Chang, H.; Kosari, F.; Andreadakis, G.; Alam, M. A.; Vasmatzis, G.; Bashir, R., DNA-Mediated Fluctuations in Ionic Current through Silicon Oxide Nanopore Channels. *Nano Lett.* **2004,** *4*, 1551-1556.
(12) Ray, S. J., Single Molecule Transistor Based Nanopore for the Detection of Nicotine. *J. Appl. Phys.* **2014,** *244307*.
(13) Wang, Y. C.; Stevens, A. L.; Han, J. Y., Million-Fold Preconcentration of Proteins and Peptides by Nanofluidic Filter. *Anal. Chem.* **2005,** *77*, 4293-4299.
(14) Kim, S. J.; Ko, S. H.; Kang, K. H.; Han, J., Direct Seawater Desalination by Ion Concentration Polarization. *Nat. Nanotechnol.* **2010,** *5*, 297-301.
(15) Dekker, C., Solid-State Nanopores. *Nat. Nanotechnol.* **2007,** *2*, 209-215.
(16) Majd, S.; Yusko, E. C.; Billeh, Y. N.; Macrae, M. X.; Yang, J.; Mayer, M., Applications of Biological Pores in Nanomedicine, Sensing, and Nanoelectronics. *Curr. Opin. Biotech.* **2010,** *21*, 439-476.
(17) Cervera, J.; Schiedt, B.; Neumann, R.; Mafe, S.; Ramirez, P., Ionic Conduction, Rectification, and Selectivity in Single Conical Nanopores. *J. Chem. Phys.* **2006,** 154502.
(18) Hlushkou, D.; Perry, J. M.; Jacobson, S. C.; Tallarek, U., Propagating Concentration Polarization and Ionic Current Rectification in a Nanochannel-Nanofunnel Device. *Anal. Chem.* **2012,** *84*, 267-274.

(19) Yossifon, G.; Chang, Y. C.; Chang, H. C., Rectification, Gating Voltage, and Interchannel Communication of Nanoslot Arrays Due to Asymmetric Entrance Space Charge Polarization. *Phys. Rev. Lett.* **2009,** *103*.
(20) White, H. S.; Bund, A., Ion Current Rectification at Nanopores in Glass Membranes. *Langmuir* **2008,** *24*, 2212-2218.
(21) Ramirez, P.; Apel, P. Y.; Cervera, J.; Mafe, S., Pore Structure and Function of Synthetic Nanopores with Fixed Charges: Tip Shape and Rectification Properties. *Nanotechnology* **2008,** 315707.
(22) Kovarik, M. L.; Zhou, K. M.; Jacobson, S. C., Effect of Conical Nanopore Diameter on Ion Current Rectification. *J. Phys. Chem. B* **2009,** *113*, 15960-15966.
(23) Siwy, Z. S., Ion-Current Rectification in Nanopores and Nanotubes with Broken Symmetry. *Adv. Funct. Mater.* **2006,** *16*, 735-746.
(24) Lan, W. J.; Holden, D. A.; White, H. S., Pressure-Dependent Ion Current Rectification in Conical-Shaped Glass Nanopores. *J. Am. Chem. Soc.* **2011,** *133*, 13300-13303.
(25) Siwy, Z.; Kosinska, I. D.; Fulinski, A.; Martin, C. R., Asymmetric Diffusion through Synthetic Nanopores. *Phys. Rev. Lett.* **2005,** 048102.
(26) Cheng, L. J.; Guo, L. J., Rectified Ion Transport through Concentration Gradient in Homogeneous Silica Nanochannels. *Nano Lett.* **2007,** *7*, 3165-3171.
(27) Maglia, G.; Restrepo, M. R.; Mikhailova, E.; Bayley, H., Enhanced Translocation of Single DNA Molecules through Alpha-Hemolysin Nanopores by Manipulation of Internal Charge. *P. Natl. Acad. Sci. USA* **2008,** *105*, 19720-19725.
(28) Derrington, I. M.; Butler, T. Z.; Collins, M. D.; Manrao, E.; Pavlenok, M.; Niederweis, M.; Gundlach, J. H., Nanopore DNA Sequencing with Mspa. *P. Natl. Acad. Sci. USA* **2010,** *107*, 16060-16065.
(29) Stefureac, R.; Long, Y. T.; Kraatz, H. B.; Howard, P.; Lee, J. S., Transport of Alpha-Helical Peptides through Alpha-Hemolysin and Aerolysin Pores. *Biochemistry* **2006,** *45*, 9172-9179.
(30) Soskine, M.; Biesemans, A.; Moeyaert, B.; Cheley, S.; Bayley, H.; Maglia, G., An Engineered Clya Nanopore Detects Folded Target Proteins by Selective External Association and Pore Entry. *Nano Lett.* **2012,** *12*, 4895-4900.
(31) Lo, C. J.; Aref, T.; Bezryadin, A., Fabrication of Symmetric Sub-5 Nm Nanopores Using Focused Ion and Electron Beams. *Nanotechnology* **2006,** *17*, 3264-3267.
(32) Li, J.; Stein, D.; McMullan, C.; Branton, D.; Aziz, M. J.; Golovchenko, J. A., Ion-Beam Sculpting at Nanometre Length Scales. *Nature* **2001,** *412*, 166-169.
(33) dela Torre, R.; Larkin, J.; Singer, A.; Meller, A., Fabrication and Characterization of Solid-State Nanopore Arrays for High-Throughput DNA Sequencing. *Nanotechnology* **2012,** 385308.
(34) Smeets, R. M. M.; Keyser, U. F.; Krapf, D.; Wu, M. Y.; Dekker, N. H.; Dekker, C., Salt Dependence of Ion Transport and DNA Translocation through Solid-State Nanopores. *Nano Lett.* **2006,** *6*, 89-95.
(35) Deng, T.; Chen, J.; Wu, C. N.; Liu, Z. W., Fabrication of Inverted-Pyramid Silicon Nanopore Arrays with Three-Step Wet Etching. *Ecs. J. Solid State Sci.* **2013,** *2*, 419-422.
(36) James, T.; Kalinin, Y. V.; Chan, C. C.; Randhawa, J. S.; Gaevski, M.; Gracias, D. H., Voltage-Gated Ion Transport through Semiconducting Conical Nanopores Formed by Metal Nanoparticle-Assisted Plasma Etching. *Nano Lett.* **2012,** *12*, 3437-3442.

(37) Sha, J. J.; Si, W.; Xu, W.; Zou, Y. R.; Chen, Y. F., Glass Capillary Nanopore for Single Molecule Detection. *Sci. China Technol. Sci.* **2015,** *58*, 803-812.
(38) Zhang, B.; Zhang, Y. H.; White, H. S., The Nanopore Electrode. *Anal. Chem.* **2004,** *76*, 6229-6238.
(39) Lan, W. J.; White, H. S., Diffusional Motion of a Particle Translocating through a Nanopore. *ACS Nano* **2012,** *6*, 1757-1765.
(40) Karhanek, M.; Kemp, J. T.; Pourmand, N.; Davis, R. W.; Webb, C. D., Single DNA Molecule Detection Using Nanopipettes and Nanoparticles. *Nano Lett.* **2005,** *5*, 403-407.
(41) Jal, P. K.; Patel, S.; Mishra, B., Chemical Modification of Silica Surface by Immobilization of Functional Groups for Extractive Concentration of Metal Ions. *Talanta* **2004,** *62*, 1005-1028.
(42) Hoogerheide, D. P.; Garaj, S.; Golovchenko, J. A., Probing Surface Charge Fluctuations with Solid-State Nanopores. *Phys. Rev. Lett.* **2009,** 256804.
(43) Liu, J.; Wang, D. C.; Kvetny, M.; Brown, W.; Li, Y.; Wang, G. L., Noninvasive Surface Coverage Determination of Chemically Modified Conical Nanopores That Rectify Ion Transport. *Anal. Chem.* **2012,** *84*, 6926-6929.
(44) Wang, G. L.; Bohaty, A. K.; Zharov, I.; White, H. S., Photon Gated Transport at the Glass Nanopore Electrode. *J. Am. Chem. Soc.* **2006,** *128*, 13553-13558.
(45) Li, Y.; Wang, D. C.; Kvetny, M. M.; Brown, W.; Liu, J.; Wang, G. L., History-Dependent Ion Transport through Conical Nanopipettes and the Implications in Energy Conversion Dynamics at Nanoscale Interfaces. *Chem. Sci.* **2015,** *6*, 588-595.
(46) Siwy, Z.; Apel, P.; Baur, D.; Dobrev, D. D.; Korchev, Y. E.; Neumann, R.; Spohr, R.; Trautmann, C.; Voss, K. O., Preparation of Synthetic Nanopores with Transport Properties Analogous to Biological Channels. *Surf. Sci.* **2003,** *532*, 1061-1066.
(47) Moon, J. M.; Akin, D.; Xuan, Y.; Ye, P. D.; Guo, P. X.; Bashir, R., Capture and Alignment of Phi29 Viral Particles in Sub-40 Nanometer Porous Alumina Membranes. *Biomed. Microdevices* **2009,** *11*, 135-142.
(48) Hu, K. K.; Wang, Y. X.; Cai, H. J.; Mirkin, M. V.; Gao, Y.; Friedman, G.; Gogotsi, Y., Open Carbon Nanopipettes as Resistive-Pulse Sensors, Rectification Sensors, and Electrochemical Nanoprobes. Anal. Chem. **2014**, 86, 8897-8901.
(49) Mara, A.; Siwy, Z.; Trautmann, C.; Wan, J.; Kamme, F., An Asymmetric Polymer Nanopore for Single Molecule Detection. *Nano Lett.* **2004,** *4*, 497-501.
(50) Siwy, Z.; Fulinski, A., Fabrication of a Synthetic Nanopore Ion Pump. *Phys. Rev. Lett.* **2002,** *198103*.
(51) Li, F.; Diaz, R.; Ito, T., Quantitative Investigation of Surface Functionalization of Cylindrical Nanopores Derived from Polystyrene-Poly(Methylmethacrylate) Diblock Copolymers. *Rsc. Adv.* **2011,** *1*, 1732-1736.
(52) Ali, M.; Schiedt, B.; Healy, K.; Neumann, R.; Ensinger, A., Modifying the Surface Charge of Single Track-Etched Conical Nanopores in Polyimide. *Nanotechnology* **2008,** 085713.
(53) Chen, B.; Lu, K., Influence of Patterned Concave Depth and Surface Curvature on Anodization of Titania Nanotubes and Alumina Nanopores. *Langmuir* **2011,** *27*, 12179-12185.
(54) Parks, G. A., The Isoelectric Points of Solid Oxides, Solid Hydroxides, and Aqueous Hydroxo Complex Systems. *Chem. Rev.* **1965,** *65*, 177-198.

(55) Schneider, G. F.; Kowalczyk, S. W.; Calado, V. E.; Pandraud, G.; Zandbergen, H. W.; Vandersypen, L. M. K.; Dekker, C., DNA Translocation through Graphene Nanopores. *Nano Lett.* **2010,** *10*, 3163-3167.
(56) Farimani, A. B.; Min, K.; Aluru, N. R., DNA Base Detection Using a Single-Layer MoS_2. *Acs Nano* **2014,** *8*, 7914-7922.
(57) Goldberger, J.; Fan, R.; Yang, P. D., Inorganic Nanotubes: A Novel Platform for Nanofluidics. *Acc. Chem. Res.* **2006,** *39*, 239-248.
(58) Lemay, S. G., Fluidics Meets Electronics: Carbon Nanotubes as Nanopores. *Angew. Chem. Int. Ed.* **2010,** *49*, 7627-7628.
(59) Siria, A.; Poncharal, P.; Biance, A. L.; Fulcrand, R.; Blase, X.; Purcell, S. T.; Bocquet, L., Giant Osmotic Energy Conversion Measured in a Single Transmembrane Boron Nitride Nanotube. *Nature* **2013,** *494*, 455-458.
(60) Siwy, Z.; Trofin, L.; Kohli, P.; Baker, L. A.; Trautmann, C.; Martin, C. R., Protein Biosensors Based on Biofunctionalized Conical Gold Nanotubes. *J. Am. Chem. Soc.* **2005,** *127*, 5000-5001.
(61) Li, Y.; Chen, C.; Kerman, S.; Neutens, P.; Lagae, L.; Groeseneken, G.; Stakenborg, T.; Van Dorpe, P., Harnessing Plasmon-Induced Ionic Noise in Metallic Nanopores. *Nano Lett.* **2013,** *13*, 1724-1729.
(62) Bocquet, L.; Charlaix, E., Nanofluidics, from Bulk to Interfaces. *Chem. Soc. Rev.* **2010,** *39*, 1073-1095.
(63) Wang, D. C.; Liu, J.; Kvetny, M.; Li, Y.; Brown, W.; Wang, G. L., Physical Origin of Dynamic Ion Transport Features through Single Conical Nanopores at Different Bias Frequencies. *Chem. Sci.* **2014,** *5*, 1827-1832.
(64) Wang, D. C.; Kvetny, M.; Liu, J.; Brown, W.; Li, Y.; Wang, G. L., Transmembrane Potential across Single Conical Nanopores and Resulting Memristive and Memcapacitive Ion Transport. *J. Am. Chem. Soc.* **2012,** *134*, 3651-3654.
(65) Feng, J. Y.; Liu, J.; Wu, B. H.; Wang, G. L., Impedance Characteristics of Amine Modified Single Glass Nanopores. *Anal. Chem.* **2010,** *82*, 4520-4528.
(66) Smeets, R. M. M.; Keyser, U. F.; Dekker, N. H.; Dekker, C., Noise in Solid-State Nanopores. *P. Natl. Acad. Sci. USA* **2008,** *105*, 417-421.
(67) Detcheverry, F.; Bocquet, L., Thermal Fluctuations in Nanofluidic Transport. *Phys. Rev. Lett.* **2012,** 024501.
(68) Lu, B.; Albertorio, F.; Hoogerheide, D. P.; Golovchenko, J. A., Origins and Consequences of Velocity Fluctuations During DNA Passage through a Nanopore. *Biophys. J.* **2011,** *101*, 70-79.
(69) Liu, J.; Wang, D. C.; Kvetny, M.; Brown, W.; Li, Y.; Wang, G. L., Quantification of Steady-State Ion Transport through Single Conical Nanopores and a Nonuniform Distribution of Surface Charges. *Langmuir* **2013,** *29*, 8743-8752.
(70) Thompson, A. P., Nonequilibrium Molecular Dynamics Simulation of Electro-Osmotic Flow in a Charged Nanopore. *J. Chem. Phys.* **2003,** *119*, 7503-7511.
(71) Peter, C.; Hummer, G., Ion Transport through Membrane-Spanning Nanopores Studied by Molecular Dynamics Simulations and Continuum Electrostatics Calculations. *Biophys. J.* **2005,** *89*, 2222-2234.
(72) Pershin, Y. V.; Di Ventra, M., Memory Effects in Complex Materials and Nanoscale Systems. *Adv. Phys.* **2011,** *60*, 145-227.

(73) van der Heyden, F. H. J.; Stein, D.; Besteman, K.; Lemay, S. G.; Dekker, C., Charge Inversion at High Ionic Strength Studied by Streaming Currents. *Phys. Rev. Lett.* **2006,** *96*.
(74) Sa, N. Y.; Fu, Y. Q.; Baker, L. A., Reversible Cobalt Ion Binding to Imidazole-Modified Nanopipettes. *Anal. Chem.* **2010,** *82*, 9963-9966.
(75) Karnik, R.; Fan, R.; Yue, M.; Li, D. Y.; Yang, P. D.; Majumdar, A., Electrostatic Control of Ions and Molecules in Nanofluidic Transistors. *Nano Lett.* **2005,** *5*, 943-948.
(76) Andersen, M. B.; van Soestbergen, M.; Mani, A.; Bruus, H.; Biesheuvel, P. M.; Bazant, M. Z., Current-Induced Membrane Discharge. *Phys. Rev. Lett.* **2012,** 108301.
(77) Zhang, B.; Galusha, J.; Shiozawa, P. G.; Wang, G. L.; Bergren, A. J.; Jones, R. M.; White, R. J.; Ervin, E. N.; Cauley, C. C.; White, H. S., Bench-Top Method for Fabricating Glass-Sealed Nanodisk Electrodes, Glass Nanopore Electrodes, and Glass Nanopore Membranes of Controlled Size. *Anal. Chem.* **2007,** *79*, 4778-4787.
(78) Jung, J. Y.; Joshi, P.; Petrossian, L.; Thornton, T. J.; Posner, J. D., Electromigration Current Rectification in a Cylindrical Nanopore Due to Asymmetric Concentration Polarization. *Anal. Chem.* **2009,** *81*, 3128-3133.
(79) Alcaraz, A.; Ramirez, P.; Garcia-Gimenez, E.; Lopez, M. L.; Andrio, A.; Aguilella, V. M., A Ph-Tunable Nanofluidic Diode: Electrochemical Rectification in a Reconstituted Single Ion Channel. *J. Phys. Chem. B* **2006,** *110*, 21205-21209.
(80) Ramirez, P.; Gomez, V.; Cervera, J.; Schiedt, B.; Mafe, S., Ion Transport and Selectivity in Nanopores with Spatially Inhomogeneous Fixed Charge Distributions. *J. Chem. Phys.* **2007,** 194703.
(81) Constantin, D.; Siwy, Z. S., Poisson-Nernst-Planck Model of Ion Current Rectification through a Nanofluidic Diode. *Phys. Rev. E* **2007,** 041202.
(82) Momotenko, D.; Girault, H. H., Scan-Rate-Dependent Ion Current Rectification and Rectification Inversion in Charged Conical Nanopores. *J. Am. Chem. Soc.* **2011,** *133*, 14496-14499.
(83) Guerrette, J. P.; Zhang, B., Scan-Rate-Dependent Current Rectification of Cone-Shaped Silica Nanopores in Quartz Nanopipettes. *J. Am. Chem. Soc.* **2010,** *132*, 17088-17091.
(84) Krems, M.; Pershin, Y. V.; Di Ventra, M., Ionic Memcapacitive Effects in Nanopores. *Nano Lett.* **2010,** *10*, 2674-2678.
(85) Siwy, Z. S.; Howorka, S., Engineered Voltage-Responsive Nanopores. *Chem. Soc. Rev.* **2010,** *39*, 1115-1132.
(86) Siwy, Z.; Gu, Y.; Spohr, H. A.; Baur, D.; Wolf-Reber, A.; Spohr, R.; Apel, P.; Korchev, Y. E., Rectification and Voltage Gating of Ion Currents in a Nanofabricated Pore. *Europhys. Lett.* **2002,** *60*, 349-355.
(87) Stein, D.; Kruithof, M.; Dekker, C., Surface-Charge-Governed Ion Transport in Nanofluidic Channels. *Phys. Rev. Lett.* **2004,** *93*.
(88) Martin, C. R.; Siwy, Z. S., Learning Nature's Way: Biosensing with Synthetic Nanopores. *Science* **2007,** *317*, 331-332.
(89) Schibel, A. E. P.; An, N.; Jin, Q. A.; Fleming, A. M.; Burrows, C. J.; White, H. S., Nanopore Detection of 8-Oxo-7,8-Dihydro-2'-Deoxyguanosine in Immobilized Single-Stranded DNA via Adduct Formation to the DNA Damage Site. *J. Am. Chem. Soc.* **2010,** *132*, 17992-17995.

(90) Wang, G. L.; Zhang, B.; Wayment, J. R.; Harris, J. M.; White, H. S., Electrostatic-Gated Transport in Chemically Modified Glass Nanopore Electrodes. *J. Am. Chem. Soc.* **2006,** *128*, 7679-7686.
(91) Hou, X.; Guo, W.; Jiang, L., Biomimetic Smart Nanopores and Nanochannels. *Chem. Soc. Rev.* **2011,** *40*, 2385-2401.
(92) Kim, S. J.; Wang, Y. C.; Lee, J. H.; Jang, H.; Han, J., Concentration Polarization and Nonlinear Electrokinetic Flow near a Nanofluidic Channel. *Phys. Rev. Lett.* **2007,** 044501.
(93) Zangle, T. A.; Mani, A.; Santiago, J. G., Theory and Experiments of Concentration Polarization and Ion Focusing at Microchannel and Nanochannel Interfaces. *Chem. Soc. Rev.* **2010,** *39*, 1014-1035.
(94) Yossifon, G.; Chang, H. C., Selection of Nonequilibrium Overlimiting Currents: Universal Depletion Layer Formation Dynamics and Vortex Instability. *Phys. Rev. Lett.* **2008,** 254501.
(95) Powell, M. R.; Sullivan, M.; Vlassiouk, I.; Constantin, D.; Sudre, O.; Martens, C. C.; Eisenberg, R. S.; Siwy, Z. S., Nanoprecipitation-Assisted Ion Current Oscillations. *Nat. Nanotechnol.* **2008,** *3*, 51-57.
(96) Innes, L.; Powell, M. R.; Vlassiouk, I.; Martens, C.; Siwy, Z. S., Precipitation-Induced Voltage-Dependent Ion Current Fluctuations in Conical Nanopores. *J. Phys. Chem. C* **2010,** *114*, 8126-8134.
(97) Feng, J.; Liu, J.; Wu, B.; Wang, G., Impedance Characteristics of Amine Modified Single Glass Nanopores. *Anal. Chem.* **2010,** *82*, 4520-4528.
(98) Wang, D.; Kvetny, M.; Liu, J.; Brown, W.; Li, Y.; Wang, G., Transmembrane Potential across Single Conical Nanopores and Resulting Memristive and Memcapacitive Ion Transport. *J. Am. Chem. Soc.* **2012,** *134*, 3651-3654.
(99) Wang, G.; Zhang, B.; Wayment, J. R.; Harris, J. M.; White, H. S., Electrostatic-Gated Transport in Chemically Modified Glass Nanopore Electrodes. *J. Am. Chem. Soc.* **2006,** *128*, 7679-7686.
(100) Liu, J.; Kvetny, M.; Feng, J.; Wang, D.; Wu, B.; Brown, W.; Wang, G., Surface Charge Density Determination of Single Conical Nanopores Based on Normalized Ion Current Rectification. *Langmuir* **2012,** *28*, 1588-1595.
(101) Liu, J.; Wang, D.; Kvetny, M.; Brown, W.; Li, Y.; Wang, G., Noninvasive Surface Coverage Determination of Chemically Modified Conical Nanopores That Rectify Ion Transport. *Anal. Chem.* **2012,** *84*, 6926-6929.
(102) Wu, J.; Li, Z., Density-Functional Theory for Complex Fluids. *Annu. Rev. Phys. Chem.* **2007,** *58*, 85-112.
(103) Zhao, S.; Wu, J., Self-Consistent Equations Governing the Dynamics of Nonequilibrium Colloidal Systems. *J. Chem. Phys.* **2011,** *134*, 054514.
(104) Liu, J.; Wang, D.; Kvetny, M.; Brown, W.; Li, Y.; Wang, G., Quantification of Steady-State Ion Transport through Single Conical Nanopores and a Nonuniform Distribution of Surface Charges. *Langmuir* **2013,** *29*, 8743-8752.
(105) Kim, S. J.; Song, Y. A.; Han, J., Nanofluidic Concentration Devices for Biomolecules Utilizing Ion Concentration Polarization: Theory, Fabrication, and Applications. *Chem. Soc. Rev.* **2010,** *39*, 912-922.
(106) Xie, Y. B.; Wang, X. W.; Xue, J. M.; Jin, K.; Chen, L.; Wang, Y. G., Electric Energy Generation in Single Track-Etched Nanopores. *Appl. Phys. Lett.* **2008,** 163116.

(107) Saleh, O. A.; Sohn, L. L., An Artificial Nanopore for Molecular Sensing. *Nano Lett.* **2003,** *3*, 37-38.
(108) Shendure, J.; Ji, H. L., Next-Generation DNA Sequencing. *Nat. Biotechnol.* **2008,** *26*, 1135-1145.
(109) Murray, R. W., Nanoelectrochemistry: Metal Nanoparticles, Nanoelectrodes, and Nanopores. *Chem. Rev.* **2008,** *108*, 2688-2720.
(110) Sardar, R.; Funston, A. M.; Mulvaney, P.; Murray, R. W., Gold Nanoparticles: Past, Present, and Future. *Langmuir* **2009,** *25*, 13840-13851.
(111) Jin, R. C., Quantum Sized, Thiolate-Protected Gold Nanoclusters. *Nanoscale* **2010,** *2*, 343-362.
(112) Zheng, J.; Zhou, C.; Yu, M. X.; Liu, J. B., Different Sized Luminescent Gold Nanoparticles. *Nanoscale* **2012,** *4*, 4073-4083.
(113) Jadzinsky, P. D.; Calero, G.; Ackerson, C. J.; Bushnell, D. A.; Kornberg, R. D., Structure of a Thiol Monolayer-Protected Gold Nanoparticle at 1.1 Å Resolution. *Science* **2007,** *318*, 430-433.
(114) Heaven, M. W.; Dass, A.; White, P. S.; Holt, K. M.; Murray, R. W., Crystal Structure of the Gold Nanoparticle $[N(C_8H_{17})_4][Au_{25}(SCH_2CH_2Ph)_{18}]$. *J. Am. Chem. Soc.* **2008,** *130*, 3754-3755.
(115) Zhu, M.; Aikens, C. M.; Hollander, F. J.; Schatz, G. C.; Jin, R., Correlating the Crystal Structure of a Thiol-Protected Au-25 Cluster and Optical Properties. *J. Am. Chem. Soc.* **2008,** *130*, 5883-5885.
(116) Dass, A.; Stevenson, A.; Dubay, G. R.; Tracy, J. B.; Murray, R. W., Nanoparticle MALDI-TOF Mass Spectrometry without Fragmentation: $Au_{25}(SCH_2CH_2Ph)_{18}$ and Mixed Monolayer $Au_{25}[S(CH_2)_2Ph]_{18-X}(L)x$. *J. Am. Chem. Soc.* **2008,** *130*, 5940-5946.
(117) Tracy, J. B.; Crowe, M. C.; Parker, J. F.; Hampe, O.; Fields-Zinna, C. A.; Dass, A.; Murray, R. W., Electrospray Ionization Mass Spectrometry of Uniform and Mixed Monolayer Nanoparticles: $Au_{25}[S(CH_2)_2Ph]_{18}$ and $Au_{25}[S(CH_2)_2Ph]_{18-X}(SR)_x$. *J. Am. Chem. Soc.* **2007,** *129*, 16209-16215.
(118) Li, G.; Jin, R. C., Atomically Precise Gold Nanoclusters as New Model Catalysts. *Acc. Chem. Res.* **2013,** *46*, 1749-1758.
(119) Zhou, C.; Yang, S. Y.; Liu, J. B.; Yu, M. X.; Zheng, J., Luminescent Gold Nanoparticles: A New Class of Nanoprobes for Biomedical Imaging. *Exp. Biol. Med.* **2013,** *238*, 1199-1209.
(120) Tang, Z. H.; Robinson, D. A.; Bokossa, N.; Xu, B.; Wang, S. M.; Wang, G. L., Mixed Dithiolate Durene-Dt and Monothiolate Phenylethanethiolate Protected Au_{130} Nanoparticles with Discrete Core and Core-Ligand Energy States. *J. Am. Chem. Soc.* **2011,** *133*, 16037-16044.
(121) Murray, R. W., Nanoelectrochemistry: Metal Nanoparticles, Nanoelectrodes, and Nanopores. *Chem. Rev.* **2008,** *108*, 2688-2720.
(122) Tlahuice-Flores, A.; Santiago, U.; Bahena, D.; Vinogradova, E.; Conroy, C. V.; Ahuja, T.; Bach, S. B. H.; Ponce, A.; Wang, G.; Jose-Yacaman, M.; Whetten, R. L., Structure of the Thiolated Au_{130} Cluster. *J. Phys. Chem. A* **2013,** *117*, 10470-10476.
(123) Ahuja, T.; Wang, D.; Tang, Z.; Robinson, D.; Padelford, J.; Wang, G., Electronic Coupling between Ligand and Core Energy States in Dithiolate-Monothiolate Stabilized Au Clusters. *Phys. Chem. Chem. Phys.* **2015***, in press*.
(124) Negishi, Y.; Sakamoto, C.; Ohyama, T.; Tsukuda, T., Synthesis and the Origin of the Stability of Thiolate-Protected Au_{130} and Au_{187} Clusters. *J. Phys. Chem. Lett.* **2012,** *3*, 1624-1628.

(125) Qian, H. F.; Jin, R. C., Controlling Nanoparticles with Atomic Precision: The Case of $Au_{144}(SCH_2CH_2Ph)_{60}$. *Nano Lett.* **2009,** *9*, 4083-4087.
(126) Jupally, V. R.; Dass, A., Synthesis of $Au_{130}(SR)_{50}$ and $Au_{130-x}Ag_x(SR)_{50}$ Nanomolecules through Core Size Conversion of Larger Metal Clusters. *Phys. Chem. Chem. Phys.* **2014,** *16*, 10473-10479.